Glucose-weighted CEST MRI in Adipose Tissue and Sepsis induced AKI

Doctoral thesis
to obtain a doctorate (PhD)
from the Faculty of Medicine
of the University of Bonn

Van Nhat Minh Vo

Hue, Vietnam

2025

Written with authorization of

the Faculty of Medicine of the University of Bonn

First reviewer: Prof. Dr. rer. nat. Verena Hörr

Second reviewer: Prof. Dr. rer. nat. Andreas Schlitzer

Day of oral examination: 17.11.2025

From the Department of Internal Medicine II, University Hospital Bonn

Table of Contents

List of abbreviations

^{18}FDG	^{18}F-Fluorodeoxyglucose
3-OMG	3-O-Methyl-D-GLC
AACID	Amine and Amide Concentration Independent Detection
APT	Amide Proton Transfer
AUC	Area Under the Curve
BAT	Brown Adipose Tissue
BUN	Blood urea nitrogen
CE	Chemical exchange
CEST	Chemical Exchange Saturation Transfer
CK	Creatine Kinase
CT	Computed Tomography
D-GLC	D-Glucose
DWI	Diffusion Weighted Imaging
FLASH	Fast Low Angle Shot
GlucoCEST	glucose-weighted CEST
GLUT	Glucose transporter
GRE	Gradient Echo
HDL	High-Density Lipoproteins
i.p	Intraperitoneal
i.v	Intravenous
IHC	Immunohistochemistry
MRI	Magnetic Resonance Imaging
MRS	Magnetic Resonance Spectroscopy Imaging
MT	Magnetization transfer
MTC	Magnetization Transfer Contrast
n.s	Not significant
NMR	Nuclear Magnetic Resonance
NOE	Nuclear Overhauser Enhancement
PBS	Phosphate buffered saline

PCI	Peritoneal Contamination and Infection Model
PCT	Proximal convoluted tubule
PET	Positron Emission Tomography
PPM	Part Per Million
PTE	Proton transfer ratio
RARE	Rapid Acquisition with Relaxation Enhancement
RF	Radio Frequency
S.D	Standard deviation
S.I	Signal intensity
S-AKI	Sepsis-induced acute kidney injury
SCr	Serum creatinine
SE	Spin echo
Seg-FLASH	Segmented-Fast Low Angle Shot
TE	Echo time
TMS	Tetramethylsilane
TR	Repetition Time
t_{sat}	Saturation time
UTE	Ultra-Short Time Echo
WAT	White Adipose Tissue
WGA	Wheat Germ Agglutinin

1. Introduction

Magnetic resonance imaging (MRI) is a non-invasive imaging technique widely used in clinical and scientific settings. Based on the principles of nuclear magnetic resonance (NMR), MRI utilizes a magnetic field and radio frequency (RF) to generate images. Isidor Rabi first introduced NMR in the early 20th century; he demonstrated how the magnetic moment could be quantified using a rotating magnetic field. Later, Felix Bloch and Edward M. Purcell independently expanded on this concept in the 1940s, showing its application in solids and liquids. In the 1970s, MRI was developed further by Paul Lauterbur and Sir Peter Mansfield(C. Westbrook & Talbot, 2019). MRI has been developed using various techniques to explore different aspects: diffusion-weighted imaging (DWI), functional magnetic resonance imaging (fMRI), or magnetic resonance spectroscopy imaging (MRS), each providing structural, functional and biochemical information, respectively(Haacke, Brown, Thompson, & Venkatesan, 1999).

Chemical exchange saturation transfer (CEST) is an advanced technique that Wolff Balaban and Ward first introduced(Gochberg & Gore, 2017). It uses a frequency-selective RF irradiation of the solute proton signal before excitation and acquisition of the water signal(Ward, Aletras, & Balaban, 2000). During this irradiation, the spin states of the labile proton originally on the targeted species are saturated and can be transferred through chemical exchange to the water pool, resulting in a negative image contrast. The indirect detection of low-concentrated solutes leads to a powerful amplification. In addition, the spatial resolution is approximately ~ 1 mm^3 in human scanner and 50 μm in plane resolution in pre-clinical scanner(Murase, 2018). Over the last decade, CEST-MRI has been developed as a promising tool for indirectly detecting exchangeable amide, amine, or hydroxyl proton groups in small concentrations(van Zijl & Yadav, 2011; B. Wu et al., 2016b). In particular, the glucose-weighted CEST (glucoCEST) MRI, another subtype of the CEST technique, using glucose as an contrast agent, is based on changes in the water signal due to the chemical exchange between water protons and the labelled hydroxyl protons in natural sugar(B. Wang et al., 2024). In addition, this technique offers the advantage of not producing ionizing radiation during an MRI exam, unlike Positron emission tomography (PET) using ^{18}F-Fluorodeoxyglucose (^{18}FDG), and it has fewer side effects compared to classic MRI contrast agents like gadolinium.

Glucose is essential for metabolic processes and serves as the main energy source for the body's organs. Therefore, an alternation in glucose metabolism are some of the signs suggesting disease progress. For example, increasing the fuel supply for metabolites to anabolic metabolism due to the regulated glycolysis process is a common feature of cancer-related diseases because cancer cells require an increased amount of energy, and this phenomenon is also known as the Warburg effect(Vinogradov, Sherry, & Lenkinski, 2013). Since glucoCEST can detect glucose concentration, it can indirectly provide information about energy metabolism in living organisms(Walker-Samuel et al., 2013). Currently, this technique is widely applied in research on the nervous system, such as cancer and stroke(Boehm-Sturm et al., 2025; Meng et al., 2024; J. Wang et al., 2016); in addition, it is also applied in some research on breast and rectal cancer(Meng et al., 2024; Rivlin & Navon, 2018). Most of the current glucoCEST is performed on animal models. It is not yet ready for clinical implementation but shows the potential as a new biomarker that can be used to diagnose and monitor diseases.

The aim of this thesis was to optimize and develop CEST and glucoCEST as a promising biomarker that can provide structural and metabolic information being suitable to differentiate between brown and white adipose tissue and evaluate sepsis-induced acute kidney injury (S-AKI).

In the first part of the study, CEST is used as a non-invasive technique to distinguish types of adipose tissue: white adipose tissue (WAT) and brown adipose tissue (BAT). In particular, BAT plays a vital role in metabolic activity and body temperature regulation. These findings are important in understanding metabolism and energy regulation in some metabolism-related diseases, such as diabetes and obesity. Current imaging modalities, like MRI with gadolinium and PET, are limited in using gadolinium and radiation(Hankir et al., 2017; Yaligar et al., 2020).

The second part of the thesis examines the validity of glucoCEST MRI to detect early signs of sepsis-related kidney injury(S-AKI), as the current biomarkers like serum creatinine or blood urea nitrogen are not sensitive or specific for diagnosing S-AKI(Peerapornratana, Manrique-Caballero, Gómez, & Kellum, 2019). We hypothesized that changes in hemodynamics and glucose reabsorption would alter the glucoCEST signal, possibly using this signal as a new imaging biomarker in diagnosing SAKI. To test this hypothesis, we conducted a mouse model of SAKI through the Peritoneal

Contamination and Infection Model (PCI)(W.-T. Zhao et al., 2023). We analyzed the glucoCEST signal change in the injured kidney regions at different time points after glucose injection.

2. Fundamental Principles

In this session, a summary of the principles of NMR, CEST and its application in MRI is provided. It presents the essential physical concepts, along with the applied techniques employed in the research. However, the detailed explanation of physics and mathematics of MRI is beyond this thesis. For readers seeking more in-depth NMR physics may refer to standard textbooks such as (Hashemi, Bradley, & Lisanti, 2010), (Jacobs, 2006), (Catherine Westbrook & Talbot, 2018), (Gochberg & Gore, 2017).

2.1. Nuclear Magnetic Resonance

2.1.1 Nuclear Spin

In principle, the physics of MRI can be explained using two approaches: classical mechanics and quantum mechanics. To fully understand NMR, it is essential to apply the principles of quantum mechanics(Xia, 2022). Fermions are the primary components of any nucleus, protons, and neutrons with half-integer numbered spin, determined by their spin quantum number. All atomic nuclei that consist of protons and neutrons with an odd number of protons/neutrons carry a nuclear spin I different from zero $I \neq 0$. Accordingly, the nucleus of hydrogen ^{1}H, consisting of a single proton, results in imbalanced spin directions that do not completely cancel each other out, giving the nucleus an angular momentum $\boldsymbol{\mu}$. And a magnetic moment $\boldsymbol{\mu}$ is associated with the nuclear spin $\boldsymbol{I}$ (Xia, 2022):

$$\boldsymbol{\mu} = \gamma \boldsymbol{I} \tag{2.1}$$

where γ is the gyromagnetic ratio that is specific constant for each nucleus. For hydrogen proton, the value is $\gamma = 2.675 \cdot 10^8 \frac{\text{rad}}{\text{s}\cdot\text{T}}$, $\frac{\gamma}{2\pi} = 42.576 \frac{\text{MHz}}{\text{T}}$. When an external magnetic field (B_0) is applied along the Z-axis, hydrogen atom systems interacts with the field. As a result, the atom spins align either parallel or antiparallel to B_0. This interaction splits energy levels into two states: a lower-energy state for spins aligned parallel to B_0 (spin-up) and a higher-energy state for spins aligned antiparallel to B_0 (spin-down). The energy difference between the two spin states is called the Zeeman effect (Figure 1) and is given by:

$$\Delta \mathrm{E} = \hbar \gamma \mathrm{B}_0 = \hbar \omega_0 \tag{2.2}$$

With the reduced Planck constant $\hbar = 2\pi\hbar$, and $\omega_0 = \gamma B_0$ being the Larmor frequency.

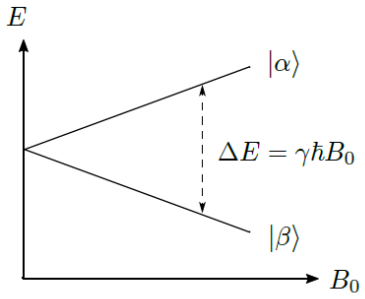

Figure 1: Zeeman splitting of energy levels for a nucleus with spin quantum number *I* = ½ as a function of B_0

Additionally, MR can also be explained using classical mechanics. The hydrogen (^1H) nucleus, the most abundant in the human body, consists of a single proton with a net positive charge. It produces a weak magnetic field denoted by a magnetic moment with vector properties: size, direction, and random orientation under normal conditions. When B_0 is applied, the nuclei align either parallel or antiparallel to B_0. The difference in the number of protons between the two orientation is only a few per million and depends on the strength of B_0 as well as the thermal effects, as described by the Boltzmann distribution. As the results, the spin system presents a net magnetization vector M aligned with B_0. Under the influence of B_0, the magnetic moments of the hydrogen nuclei precess around the magnetic field with an angular frequency proportional to the gyromagnetic ratio (γ), a constant specific to each nucleus, and B_0 strength. This is given by the Larmor frequency (ω)(C. Westbrook & Talbot, 2019):

$$\omega = \gamma B_0 \qquad (2.3)$$

The Larmor equation shows that the precession frequency is proportional to the magnetic field strength.

2.1.2 Bloch equation

In NMR experiments, a macroscopic ensemble containing a large number of protons (with $N > 10^6$) is considered instead of a single nuclear spin. The net magnetization $\vec{M}$ is the sum of magnetic moments of the spin ensemble, reflecting the balance between spin-up and spin-down nuclei. $\vec{M}$ precesses around the z-axis under the influence of B_0. To observe the magnetization, the net magnetization vector $\vec{M}$ must be flipped by applying an oscillating magnetic field (B_1) in the plane perpendicular to B_0. This process is called RF excitation, and the frequency of this RF pulse should match the Lamor frequency of the precessing protons to induce the resonance. As a result of resonance, the protons gain energy and transition to the higher energy state, where they are anti-parallel to B_0. As a result, in the classical description the protons move in phase with each other into the

transversal plane, generating transverse magnetization. The transverse magnetization vector rotates at the Larmor frequency, producing a moving magnetic field. A nearby conductive receiver coil detects this change by inducing an alternating voltage, generating a current detected as an MR signal, similar to how an antenna picks up radio waves. Once the RF pulse is turned off, the magnetization gradually returns to thermal equilibrium or lower energy state through a process called relaxation. This occurs due to the interaction of spins with their surroundings known as longitudinal spin-lattice relaxation time (T_1), and the interaction between spins, known as transversal spin-spin relaxation time (T_2).

Based on the classic magnetization equation formulated by Niels Bohr(Xia, 2022), given the large number of proton spins within the measurement volume, it is sufficient to consider the time-dependent expectation value of the classical macroscopic magnetization $\vec{M}$:

$$\frac{d\vec{M}(t)}{dt} = \vec{M}(t) \times \gamma\vec{B}(t) \tag{2.4}$$

And in order to describe the phenomenon that including the interactions of the nuclear spins with one another and with the environment, Felix Bloch expanded the equations given in (2.4), resulting in the Bloch-equations that uses to describe the interaction phenomenon(Bloch, Hansen, & Packard, 1946):

$$\frac{dM_x}{dt} = \gamma\left(\vec{M} \times \vec{B}\right)_x - \frac{M_x}{T_2} \tag{2.5}$$

$$\frac{dM_y}{dt} = \gamma\left(\vec{M} \times \vec{B}\right)_y - \frac{M_y}{T_2} \tag{2.6}$$

$$\frac{dM_z}{dt} = \gamma\left(\vec{M} \times \vec{B}\right)_z - \frac{M_z - M_0}{T_1} \tag{2.7}$$

with M_0 is the equilibrium magnetization. The relaxation times are strongly dependent on the chemical environment. T_1 arises from the interaction between the spin system and the thermal reservoir (lattice), driven by molecular movements that cause temporary fluctuations in the magnetic field. T_2, on the other hand, results from a dephasing of the individual spin ensembles among one another. In reality, the spins lose their phase coherence faster due to the local field inhomogeneities of the static field B_0 and result in a shorter T_2^* relaxation time:

$$\frac{1}{T_2^*} = \frac{1}{T_2} + \frac{1}{T_2'} \tag{2.8}$$

Where $T_2' = \gamma\Delta B_0$ describing the dephasing due to the local field-inhomogeneities.

2.1.3 Relaxation

2.1.3.1 Longitudinal (Spin-Lattice) relaxation

The molecular lattice surrounding the nuclei allow energy exchanges between excited nuclei and the lattice. When nuclei interact, energy is transferred from discrete quanta, not gradually. As a result,, after RF excitation, the net magnetization vector returns to its original magnitude exponentially, driving by fluctuating magnetic fields (See Figure 2). Spin-lattice relaxation, characterized by the time constant T_1, describes the time required for magnetization to return to 63% of its original value (See Figure 2). Typical T_1 values in biological tissue range from about 50 milliseconds to a few seconds(Catherine Westbrook & Talbot, 2018).

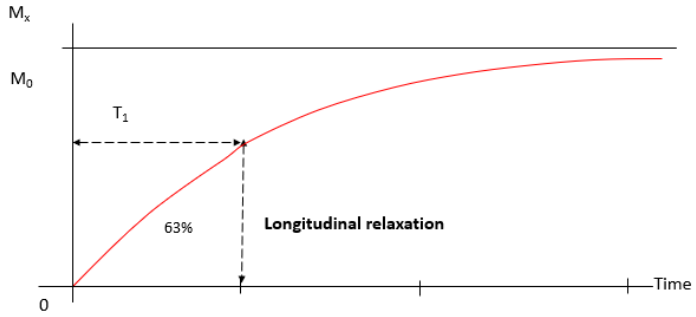

Figure 2: The longitudinal relaxation curve illustrates the net magnetization recovery along the z-axis. T_1 is the time magnetization recovers to 63% of its initial value before the RF is applied

2.1.3.2 Transverse (Spin-Spin) relaxation

After RF excitation, in addition to T_1 relaxation, T_2 relaxation occurs. The transverse relaxation refers to the process in which protons lose phase coherence in the x–y plane, leading to a decrease in transverse magnetization. During transverse relaxation, energy exchange between spins cause a loss of phase coherence. Moreover, interactions between individual spins create random local magnetic field variations, which cause fluctuations in the processional frequency of the nuclei. As a result, a gradual and random dephasing of the spins occurs, causing a decay in the transverse component of the net magnetization (See Figure 3). If spin-spin interactions were the only contributing to the dephasing, T_2 could be determined. However, spin coherence is also influenced by inhomogeneities in the applied magnetic field. The exponential decay in signal resulting from both of T_2 and field

inhomogeneities is referred to as T_2^*, the effective transverse relaxation time.(Catherine Westbrook & Talbot, 2018)

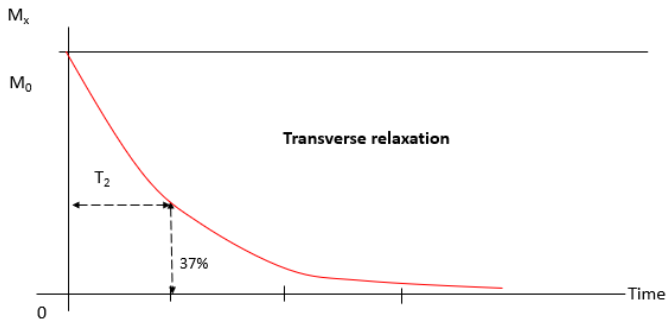

Figure 3: The transverse relaxation process describes the decay of magnetization in the transverse plane (M_{xy}). It is also known as the T_2 decay time, during which the transverse magnetic vector decays to 37% of its initial magnitude.

2.1.4 Chemical shift

Hydrogen atoms, bound within a molecule, experience a local magnetic field due to the electron cloud surrounding each nucleus, which shields the nucleus from B_0. Consequently, the local variation in the magnetic field strength for the proton spins can be described as follows(Gochberg & Gore, 2017):

$$\overrightarrow{B_{\text{loc}}} = \overrightarrow{B_0} + \delta\vec{B} = \overrightarrow{B_0}(1-\sigma) \tag{2.9}$$

where $\overrightarrow{B_{\text{loc}}}$ is the local magnetic field, σ is the shielding constant. Consequently, $\overrightarrow{B_{\text{loc}}}$ the change of resonance frequency caused by σ causes is given by:

$$\omega = \omega_0 + \delta\omega = \gamma B_0(1-\sigma) \tag{2.10}$$

with $\delta\omega$ is the resonance frequency shift that strongly depends on the chemical environment. It is referred to as a chemical shift (CS):

$$\delta\omega = \gamma\delta\vec{B} \tag{2.11}$$

For the B_0 field independent representation, CS is given by a frequency ratio in parts per million (ppm) with the reference frequency ω_{ref} :

$$\delta[\text{ppm}] = \frac{\omega-\omega_{\text{ref}}}{\omega_{\text{ref}}} \cdot 10^6 \tag{2.12}$$

In MRS, tetramethylsilane (TMS) is commonly used as the reference substance for protons(Faghihi et al., 2017) (See Figure 4). However, in the magnetization transfer technique, the signal of free water proton is used as a reference, assigned to the chemical shift of $\delta = 0$ ppm. In MRS spectra, the frequency axis is conventional directed from downfield (higher frequency) to upfield (lower frequency).

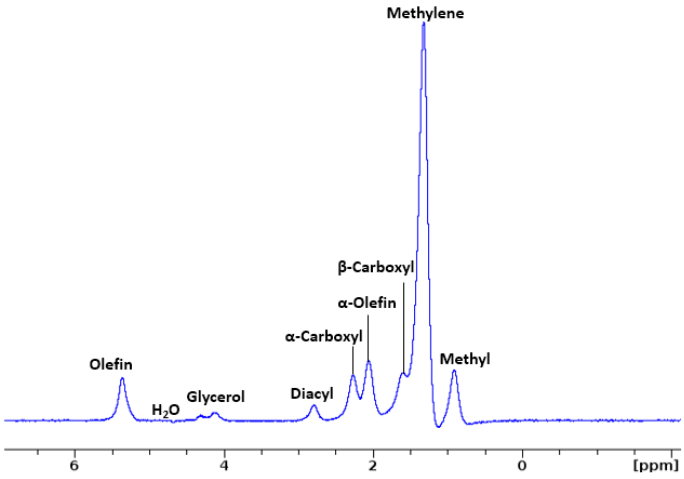

Figure 4: Representative ^{1}H MRS spectra of the adipose tissue in mice acquired at 9.4 MRI system. The chemical shift effect allows for the distinction between different chemical groups by using MRS. The water signal is suppressed (resonating at δ ≈ 4.7 ppm with respect to TMS).

2.2 Magnetic Resonance Imaging

2.2.1 Spatial encoding

Spatial encoding is achieved by adding superimposing spatially varying linear magnetic fields $\vec{G} = (G_x, G_y, G_z)$, resulting in a spatially dependent magnetic field $\vec{B}$:

$$\vec{B}(\vec{r}) = \overrightarrow{B_0} + (\vec{G} \cdot \vec{r}) \tag{2.13}$$

With $\vec{r}$ is the location of a spin. The spatial position of spin is encoded by their effective resonance frequency by adding a gradient field which is parallel to B_0 $(\vec{G} \parallel \overrightarrow{B_0})$:

$$\omega_0(\vec{r}) = \gamma\left(\overrightarrow{B_0} + \vec{G}(\vec{r})\right) \tag{2.14}$$

By convention, $(\vec{G} \parallel \overrightarrow{B_0})$ in order to maintain the original quantization axis of the nuclear spins. The complete signal encoding pathway during an MR experiment is described in the following sections.

2.2.1.1 Slice selection

In the first step, the slice selection is performed by applying a linear gradient in the Z-direction, G(z), during the RF irradiation (Hashemi et al., 2010). The transverse slice in the object resonates at a different Larmor frequency depending on Z as follows:

$$\omega_0(z) = \gamma\left(\overrightarrow{B_0} + G_z \cdot z\right) \quad (2.15)$$

The combination of the slice selective gradient, RF-pulse, and gradient strength is used to adjust the location and thickness of the 2D. The RF bandwidth and gradient amplitude directly control the slice thickness, as shown in the equation below:

$$SI_t = \frac{\text{TBW}}{\gamma G} \quad (2.16)$$

Where SI_t is slice thickness (Hz), TBW is the transmit bandwidth (KHz), γ is the gyromagnetic ratio and G is the gradient amplitude (mT/m).(McRobbie, Moore, Graves, & Prince, 2017).

2.2.1.2 Frequency encoding

After the slice selective excitation, the two remaining signal dimensions must be encoded in the x and y directions. During read out, a gradient in the x-direction is applied orthogonally to the slice selection gradient. As the signal is received, the frequency of the emitted signa correlates with its position along the G_x gradient axis. Therefore, the spins precess with different Larmor frequencies in the x- direction given by:

$$\omega_0(x) = \gamma\left(\overrightarrow{B_0} + G_x \cdot x\right). \quad (2.17)$$

The Fourier transform of the detected signal is a projection onto the x-axis. The amplitude of each frequency component, or the intensity at each position along the x-axis, is proportional to the summed signal in the y-direction for that x-position. The G_x gradient is referred to as the “read-out gradient” or frequency encoding gradient(Catherine Westbrook & Talbot, 2018).

2.2.1.3 Phase encoding

The phase-encoding gradient (G_y) is applied during the time interval between slice excitation and read-out along the y-axis. Before G_y is applied, a proton within a slice precesses at the base frequency w_0. In the next step, the phase of the precessing spin packages is manipulated to encode the remaining spatial dimension (y-direction). Under the influence of G_y, the precessional frequency of the protons increases or decreases

according to the Larmor Equation. Once G_y is turned off, the protons progress to their original frequency. Although the protons precess with the same frequency, they are slightly out of phase. A proton located at the edge of the chosen FOV experiences the maximum phase shift during each phase encoding step, requiring multiple phase encoding steps along the y-axis to fully encode the spatial information. During phase encoding period t_{PE}, the magnetization along the y direction accumulates a phase Φ(y), given by(Xia, 2022):

$$\Phi(y) = \frac{\gamma}{2\pi} \int_{t_0}^{t_{PE}} G_y(t) \cdot y \, dt \tag{2.18}$$

The system differentiate between nuclei positioned at different locations along the phase-encoding gradient by applying various phase encoding steps, resulting in different precessional phases of their magnetic moments. However, since the phase accumulation remains unchanged during the readout, the N_y phase encoding steps with varying strengths of gradient Gy must be repeated multiple times to acquire the full k-space. Afterwards, the second Fourier transform is applied to compute the final image.

2.2.2 MRI pulse sequences

2.2.2.1 Spin echo (SE)

2.2.2.1.1 Conventional spin echo

Spin echo signal generation is designed to meet the timing requirements of phase encoding while allowing a more complete evolution of spin-spin interactions. The 90° pulse and the slice-selection gradient define the imaged slice. The 90° pulse flips the magnetization into the transverse plane, while the 180° refocusing pulse, applied precisely at TE/2, reverses dephasing effects to generate a spin echo. The time from excitation to the peak of the echo signal is the echo time (TE) (See Figure 5).The interval between consecutive excitations is the repetition time (TR), which must be long enough to allow sufficient recovery longitudinal magnetization through T_1 relaxation(C. Westbrook & Talbot, 2019).

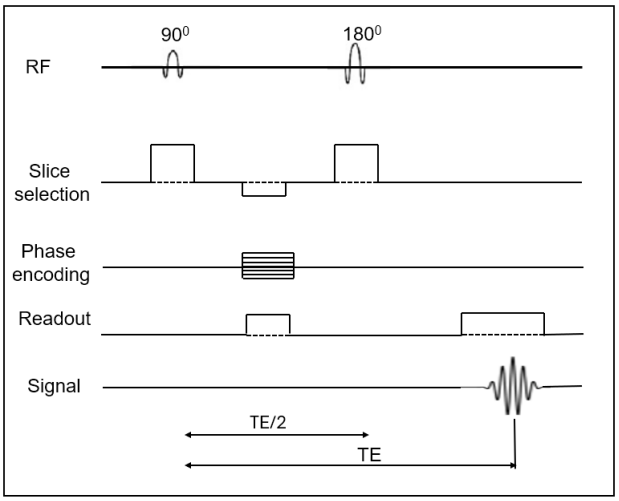

Figure 5: The spin echo pulse sequence diagram illustrates the sequence of RF pulses and magnetic field gradients used for spatial encoding. This sequence comprises a 90° excitation pulse followed by a 180° refocusing pulse, which generates the spin echo signal.

2.2.2.1.2 Fast spin echo

Rapid Acquisition with Relaxation Enhancement (RARE) is a fast spin echo sequence using a series of 180^0 refocusing pulses. It generates multiple spin echoes, allowing multiple k-space rows to be filled with a single excitation. Each echo is separately phase-encoded, and the phase encoding is incremented within one echo train to accelerate the acquisition(C. Westbrook & Talbot, 2019) (See Figure 6).

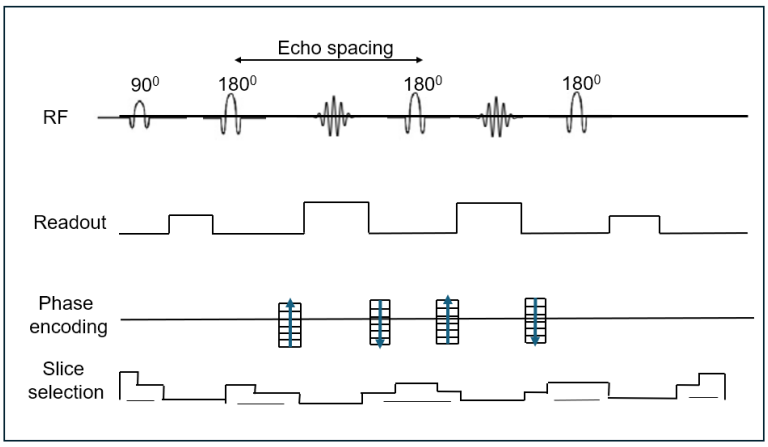

Figure 6: The fast spin echo sequence consists of a 90^0 excitation and a series of 180^0 refocusing pulse. It helps to acquire several lines of data for every TR period, reducing the overall scan time by the RARE factor or turbo factor

2.2.2.2 Gradient echo pulse sequences

2.2.2.2.1 Gradient echo imaging (GRE)

Instead of using a 180^0 pulse to rephase the spins into an echo, the FID-domain can be used for signal detection. In a gradient echo imaging sequence, a gradient is applied for a brief period in the read-out direction following the excitation pulse. This causes spins to precess at different rates based on their position along the x-axis, leading to dephasing and a signal drop. The gradient is then reversed, so that spins previously in a positive field are now in a negative field, and vice versa (See Figure 7). This reversal rephases leads the spins, generating an echo signal. Gradient reversal refocuses only the spins dephased by the gradient, while in GRE, field inhomogeneity persists, affecting image contrast through T2* effects, unlike in SE, where the 180° RF pulse minizes this effect (McRobbie et al., 2017)

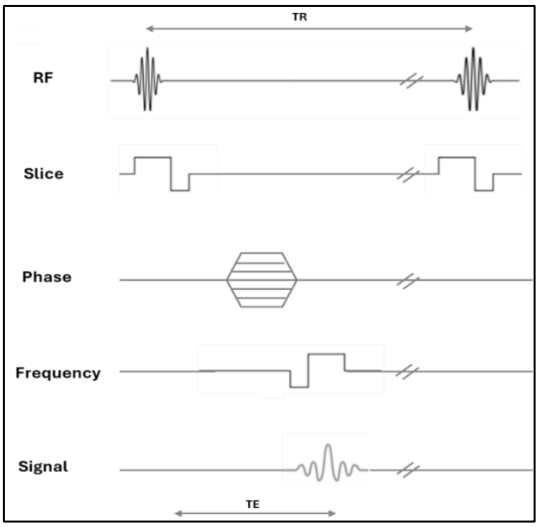

Figure 7: The diagram of a 2-dimensional gradient echo sequence. The gradient echo signal produced at TE is generated by a preceding sequence of dephasing and rephasing gradients.

2.2.2.2.2 Segmented FLASH sequence

Segmented Fast Low Angle Shot (SegFLASH) is a turbo gradient-echo technique that generates multiple echoes with a single slice-selective RF pulse. It allows for short TR times through rewound phase encoding and constant spoiling gradients (See Figure 8). By combining short TR times and segment-slicing, steady-state magnetization ensures consistent signal intensity across all acquired k-space lines and continuous data acquisition without full relaxation between excitations, optimizing imaging efficiency and reducing scan time (Brown, Cheng, Haacke, Thompson, & Venkatesan, 2014).

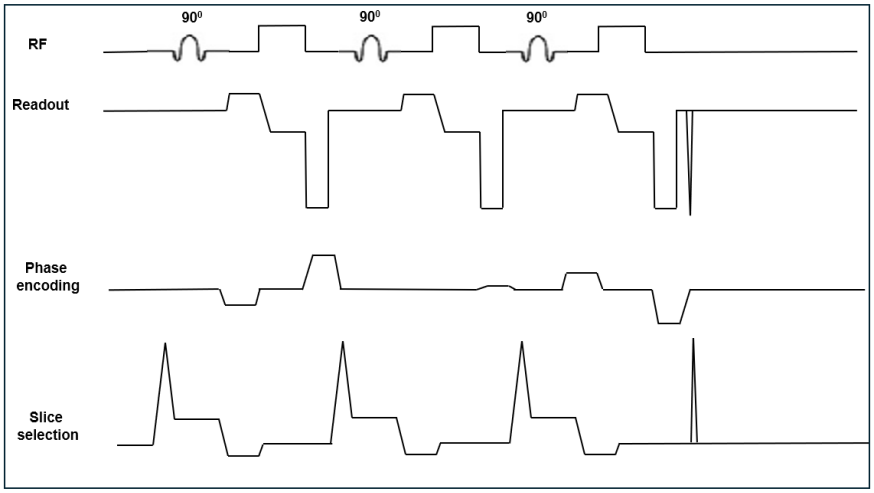

Figure 8: The segmented FLASH MRI sequence. It uses RF excitation 90^0 followed by gradient rephasing to generate an echo. The sequence is able to run with a short TR due to the use of compensated (rewound) phase encoding and constant spoiling gradients.

2.2.2.2.3 Ultra-short echo time sequence

Ultra-short echo time sequence (UTE) is a rapid imaging sequence. To reduce gradient switching time, UTE use non-Cartesian k-space sampling, such as center-out radial or spiral readout trajectories. Starting each encoding line at the center of k-space saves phase encoding time and allows sampling while the gradients are still ramping up(See Figure 9). UTE employs various k-space trajectories, including radial, spiral, twisted, and cone trajectories(Larson et al., 2016).

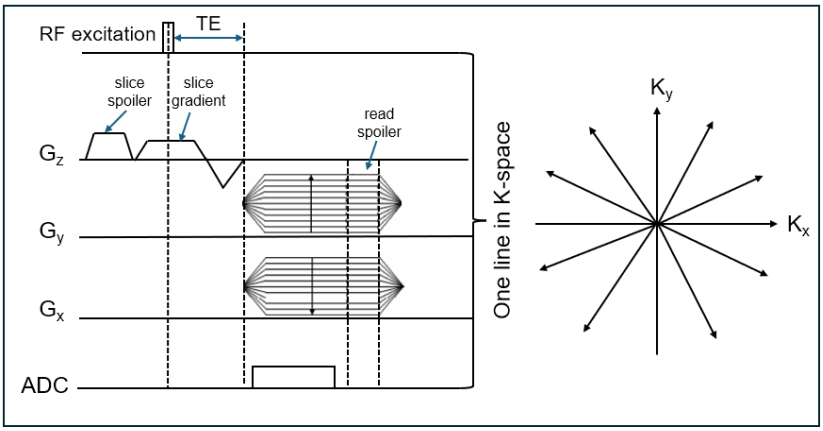

Figure 9: Diagram of UTE sequence in the free induction decay (FID) mode. UTE sequences exploit the center-out radial trajectories that fill in the k-space data with radial spokes. In the ramp-sampled FID acquisition, the radial spokes always start from the center of k-space.

2.2.2.3 Diffusion weighted imaging

DWI is a non-invasive technique that allows to encode the random motion of water molecules in the body. It reflects the microscopic tissue characteristics. Therefore, this techniques are widely used for assessing the microstructural changes of different organs over the past 20 years(Baliyan, Das, Sharma, & Gupta, 2016).

Diffusion results from the thermal movement of molecules, with water molecules moving randomly in all directions, a phenomenon known as Brownian motion. In 1905, Albert Einstein statistically described this process by using the Gaussian Probability Distribution ,as diffusion is a random process that cannot be mechanistically described at the single-particle level:

$$\langle r^2 \rangle = 2NDt, \tag{2.19}$$

Where $\langle r^2 \rangle$: is mean squared displacement, representing the average squared distance traveled by a particle over time,

N: is the number of spatial dimensions,

D: is the diffusion coefficient, which quantifies how fast a particle spreads in a medium. It depends on factors like temperature, viscosity, and particle size,

t: is the time, representing the duration over which diffusion occurs.

In principle, the basis of DWI sequences was first developed by modifying standard T_2-weighted spin-echo sequences, adding bi-polar gradients and 180^0 refocusing pulse to sensitize the signal to diffusion effects. This sequence is known as Stejskal and Tanner-sequence(Baliyan et al., 2016).

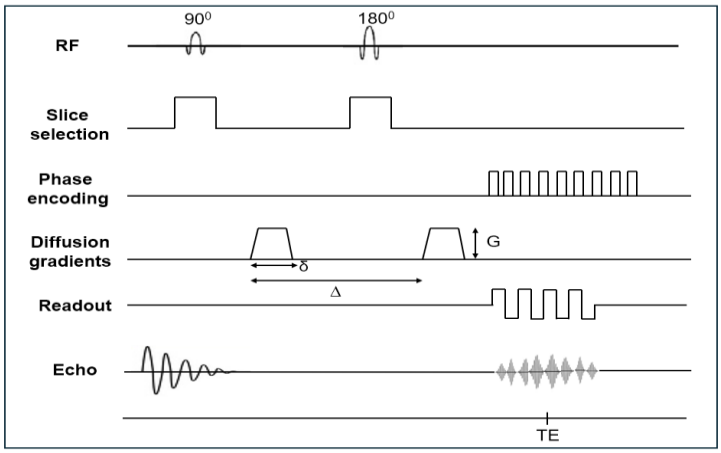

Figure 10: The fast spin echo imaging (The Stejskal–Tanner diffusion-weighted imaging sequence) for single diffusion encoding by applying the symmetric diffusion-sensitizing gradient 180^0 refocusing pulse.

The paired gradients are applied along the same direction and length, with opposite signs due to the 180° pulse. As a result, the spin diffuses along with the gradient direction, initially dephased by the first gradient and rephased by the second. However, diffusion causes a loss in signal intensity, as moving spins contribute less to the measured signal. For moving water molecules, the spin moves in the parallel direction of the applied gradient; the second gradient does not fully rephrase the signal, resulting in signal loss (See Figure 10).

The signal intensity of DWI replies to several factor such as gradient amplitude (G), the duration of a gradient pulse (δ), and time interval between the bipolar gradients (∆). The relationship between these factors is given by the expression below:

$$b = \gamma^2 G^2 \delta^2 \left(\Delta - \frac{\delta}{3}\right). \tag{2.20}$$

with b is a factor that depends on the strength and duration of the diffusion-encoding gradient pulses; γ is the gyromagnetic ratio. This equation is under the condition that the gradient pulses are bipolar and symmetric trapezoids, and the diffusion time Δ is large enough compared to the pulse duration δ for the approximation to be valid(Jones, 2010).

2.3 Magnetization transfer and chemical exchange saturation transfer

2.3.1 Magnetization transfer

Magnetization transfer (MT) is the phenomenon in which magnetization can be transferred from one biological tissue compartment to another(Henkelman, Stanisz, & Graham, 2001). In the following, the pool model is formulated by a proton pool A which has an identical chemical shift (δ_A), relaxation properties and exchange rate (k_{AB}) and exchanges magnetization with a second pool, pool B.

2.3.1.1 Bloch-McConnell equation

The Bloch-McConnell equations(McConnell, 1958), an expanded version of the Bloch Equations incorporating magnetization transfer terms, are presented below:

$$\frac{d}{dt} M_{xA} = -\Delta\omega_A M_{yA} - R_{2A} M_{xA} + k_{BA} M_{xB} - k_{AB} M_{xA} \tag{2.21}$$

$$\frac{d}{dt}M_{yA} = +\Delta\omega_A M_{xA} - R_{2A}M_{yA} - \omega_1 M_{zA} + k_{BA}M_{yB} - k_{AB}M_{yA} \quad (2.22)$$

$$\frac{d}{dt}M_{zA} = +\omega_1 M_{yA} - R_{1A}\left(M_{zA} - M_{zA,0}\right) + k_{BA}M_{zB} - k_{AB}M_{zA} \quad (2.23)$$

$$\frac{d}{dt}M_{xB} = -\Delta\omega_B M_{yB} - R_{2B}M_{xB} - k_{BA}M_{xB} + k_{AB}M_{xA} \quad (2.24)$$

$$\frac{d}{dt}M_{yB} = +\Delta\omega_B M_{xB} - R_{2B}M_{yB} - \omega_1 M_{zB} - k_{BA}M_{yB} + k_{AB}M_{yA} \quad (2.25)$$

$$\frac{d}{dt}M_{zB} = +\omega_1 M_{yB} - R_{1B}\left(M_{zB} - M_{zB,0}\right) - k_{BA}M_{zB} + k_{AB}M_{zA} \quad (2.26)$$

These equations illustrate the dynamic magnetization of two proton pools A, and B during RF irradiation with $\omega_1 = \gamma B_1$. R_{1A} and R_{2A} are the longitudinal and transversal relaxation rates for pool A, defined as water pool and, pool B described as solute pool with R_{1i} and R_{2i} are the relaxation rates of a particular pool B. $\Delta\omega_A = \omega_{RF} - \delta_A$ refers to the shift of RF irradiation with frequency ω_{RF} which give in ppm, and the pool A with the Larmor frequency δ_A. The exchange rate denoted as k_{AB} refers to the transfer from water pool to solute pool while k_{BA} describes the transfer from solute pool to water pool. At equilibrium condition, the following relationship is given as:

$$k_{BA} \cdot M_{0,B} = k_{AB} \cdot M_{0,A} \quad (2.27)$$

With k_{AB} refers to the forward transfer and the magnetizations at thermal equilibrium $M_{0,B}$ and $M_{0,A}$ define the relative population fraction f_B , calculated as $f_B = \frac{M_{0,B}}{M_{0,A}}$. The exchange of multiple-solute pools with water can be described by the extension of this equation.

2.3.1.2 Chemical exchange

Chemical exchange (CE) is a process based on acid-base reactions that induce the physical exchange of protons between two pools. For instance, exchange occurs between functional groups such as amides, amines or hydroxyl groups, and water (See Figure 11). This leads to magnetization transfer between different molecular environments as spin state remains unchanged(B. Wu et al., 2016a). This transfer is important to explain the Chemical exchange saturation transfer (will be described in the section 2.3.2) effect which depends on the exchange rate and concentration of the functional group (See Table 1).

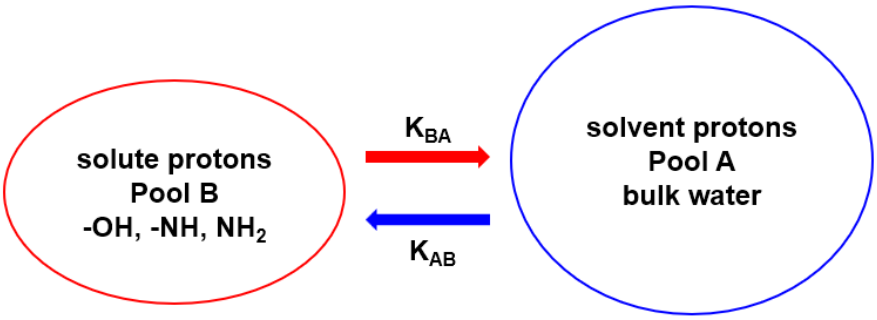

Figure 11: Schematic illustration of the two-pool model. Pool B (solute) exchanges with Pool A (solvent). The characteristics of the protons of each pool are defined by the relaxation rates and the resonance frequency.

Functional group	Solute	δ_i (ppm)	Exchange rate k_{BA} (Hz)
Amide (-CONH-)	Proteins	3.5	28.6-280
Amine ($-NH_2$)	Proteins	2.0	700-10000
Hydroxyl (-OH)	Glucose, lactate	0.4 – 2.9	From 30 to several thousands
Guanidinium $(-NH_2)^+{}_2C(=NH)$	Creatine	1.9	950

Table 1: The overview of endogenous functional groups that include the resonance frequencies δ_i and the exchange rate (Hz). The data is taken from references(DeBrosse et al., 2016; Goerke, Zaiss, & Bachert, 2014; Goerke et al., 2015; Haris et al., 2012; Liepinsh & Otting, 1996; J. Zhou, Payen, Wilson, Traystman, & van Zijl, 2003)

2.3.1.3 Dipolar interaction

Dipolar interaction is a magnetic interaction between nuclear spins in coupled spin systems that occur through space. It creates a cross-relaxation pathway, enabling magnetization transfer between different pools. This effect is known as the nuclear Overhauser effect (NOE). There are two types of dipolar interactions: intramolecular dipolar (the spins are on the same molecule) and intermolecular dipolar (they are on different molecules)(Gochberg & Gore, 2017).

2.3.2 Chemical exchange saturation transfer

2.3.2.1 Saturation transfer

CEST is a technique used to indirectly detect the protons in the solute pool (e.g. metabolites, peptides or guanidyl groups in proteins) with concentrations in the millimolar

(mM) range(Vinogradov et al., 2013). Saturation refers to the depletion of magnetization in a specific pool of nuclear spins. To achieve this, a selective RF irradiation with saturation duration time t_{sat} and RF amplitude B_1 is applied to saturate a specific pool (solute pool). This saturated magnetization is then transferred to neighboring proton pool(solvent pool). As saturation accumulates, the magnetization of solvent pool is reduced. The reduced signal is detected after the presaturation by conventional MRI imaging sequence. This indirect signal gain is referred to as proton transfer ratio (PTE) which depends on the longitudinal relaxation time and the exchange rate of the magnetization transfer pathway k_{ex} :

$$PTE \approx k_{BA} \cdot T_{1A} = k_{ex}. T_{1A} = \frac{k_{ex}}{R_{1A}} \qquad (2.28)$$

In other words, the greater the magnetization exchange between pools and the longer the magnetization is stored within the modified water signal, the stronger the CEST effect.

2.3.2.2 CEST process and the Z-spectrum

In general, the CEST process be divided into separate phases:

(1)The frequency selective RF saturation

(2) The following normal excitation pulse is applied, and the read-out of the modified water signal is achieved

In magnetization transfer experiments, saturation refers to the reduction of net magnetization in a solute pool by applying RF irradiation at the Larmor frequency of the spins within the pool, with a duration t_{sat} and an B_1 amplitude. Through chemical exchange, this results in saturation accumulation in the water signal (See Figure 12). The excitation and readout of the reduced signal M_{zw} occur immediately after the presaturation phase (Vinogradov et al., 2013),enabling indirect solute quantification.

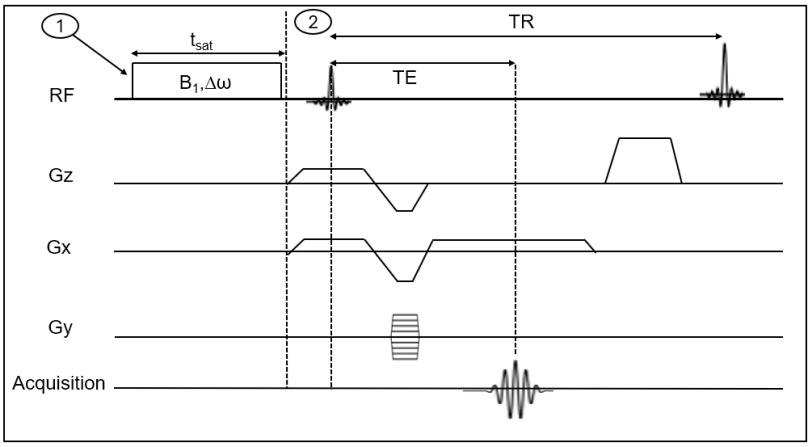

Figure 12: An example of CEST spin echo pulse sequence with continuous wave saturation pulse. The CEST sequence consists of two blocks: (1) the CEST irradiation block which the CEST-solute pool is saturated with saturation power B_1 during the saturation time t_{sat} and (2) the subsequent image excitation and read-out of the modified water proton signal

2.3.2.3 The Z-spectrum

The acquired images are obtained in CEST experiments by applying continuous RF irradiation over time at various frequency offsets (Δω) followed by subsequent water signal acquisition which is performed using a conventional MRI readout such as SE or GRE(Vinogradov et al., 2013) (See Figure 12). During this saturation phase, the equilibrium magnetization $M_{A,0}$ is reduced to M_{ZA} due to the saturation transferred from the solute pools (See Figure 13). Afterwards, the acquired water signals are normalized with the unsaturated equilibrium magnetization of water ($M\frac{0}{zA}$), one obtains what is referred to as the Z-spectrum:

$$Z\ (\Delta\omega) = \frac{\mathbf{MzA}(\Delta A)}{M_Z^0} \qquad (2.29)$$

where $\Delta\omega = \omega_{RF} - \omega_A$ is the multiple saturation frequency offsets with respect to the water resonance ω_A. In addition, the conventional MRI read out sequence for the water signal acquisition can produce one Z-spectrum for each individual pixel in the acquired MR image.

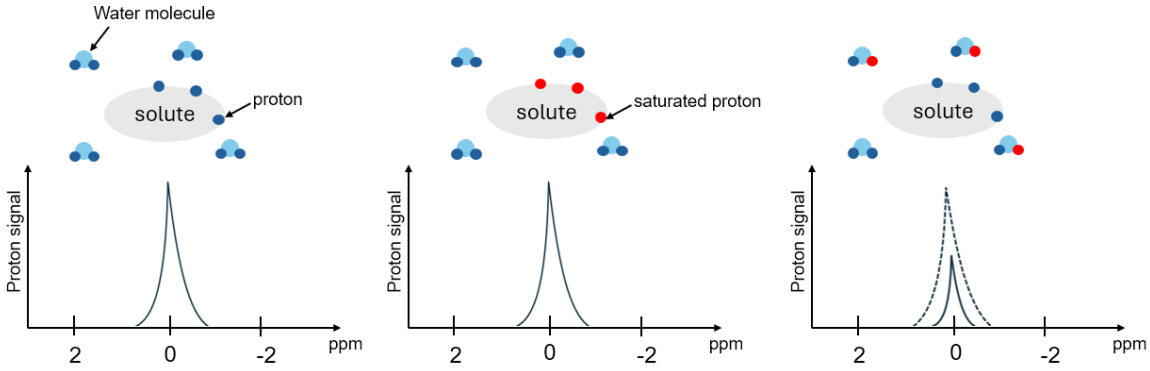

Figure 13: The diagram illustrates the principles of CEST process. The exchangeable proton on the solute can transfer RF saturation to the proton of surrounding water, resulting in a decrease in the water signal after excitation.

2.3.2.4 Factors influencing the Z-spectrum

- **Magnetic field strength**

In addition to the main factors like the exchange rate and metabolites concentration that mainly influence CEST contrast, several other parameters also contribute to the CEST effect. For example, the separation of resonance frequencies from the water signal depends on the strength of B_0. B_0 also affects the longitudinal relaxation times, impacting the saturation storage(J. Kim, Wu, Guo, Zheng, & Sun, 2015).

- **Relaxation rate**

The T_1 relaxation rate influences the time for saturation accumulation in the solute pool. A longer T_1 results in a stronger CEST effect in the steady state for a constant t_{sat}. In addition to T_1, T_2 relaxation also affects the CEST signal through the RF spillover effect. Specifically, exchangeable protons with a short T_2 relaxation rate are directly influenced by RF saturation from the bulk water pool(J. Kim et al., 2015).

- **RF irradiation amplitude and saturation time**

Magnetization is transferred from the exchangeable pool to the water pool by applying RF which involves two parameters: B_1 amplitude and t_{sat}. B_1 is used to target specific exchange regimes, with stronger RF amplitude more efficiently labeling faster-exchanging proton pools(Zaiss, Jin, Kim, & Gochberg, 2022). In contrast, reducing RF power attenuates the CEST effect, particularly for slow-exchanging proton pools. Figure 14 illustrates the characteristics of glucoCEST at different RF saturation levels. Since

hydroxyl groups are faster-exchanging pools, the CEST signal increases as saturation power rises(B. Wu et al., 2016b).

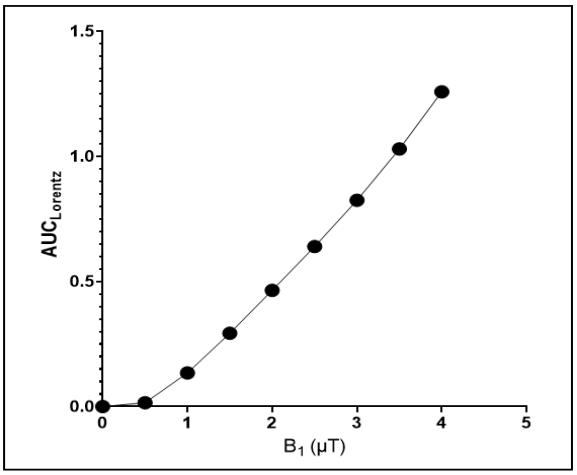

Figure 14: Characterization of glucoCEST dependence on B_1. The glucoCEST was performed at different B_1 power levels and the saturation duration of 1s, with a 60 mM 3-OMG phantom, diluted in phosphate buffered saline (PBS). The $AUC_{Lorentz}$ was calculated over the complete Lorentzian function range from -6 to 6 ppm.

- **pH effects**

CEST effect is influenced by pH, as proton exchange with water can be acid- or base-catalyzed. For paraCEST agents, pH affects the exchange rate, particularly when NH or OH groups are involved(Vinogradov et al., 2013; Zaiss & Bachert, 2013). the proton exchange rate constant rises, leading to a stronger CEST signal. However, this relationship can vary depending on the CEST agent. For instance, the CEST effect of 3-O-Methylglucose is stronger near neutrality, while D-GLC shows a stronger effect in more acidic environments(Anemone et al., 2021). This effect is most pronounced within a pH range of 6.0 to 8.0, with changes in the CEST peak intensity, especially at appropriate saturation B_1 levels(Anemone et al., 2021). In some cases, the pH of the environment can shift the CEST intensity, particularly for agents with amide protons. dditionally, factors like experimental conditions and different proton exchange mechanisms can modify pH's impact on the CEST signal(Vinogradov et al., 2013). Understanding how pH affects CEST agents helps refine the control and interpretation of the CEST signal.

2.3.3 GlucoCEST

As mentioned previously, CEST MRI is the MR imaging technique that enables the indirect detection of exchangeable protons, including amide, amine, or hydroxyl proton groups, in

low concentrations(Gochberg & Gore, 2017; McMahon, 2017). Glucose, which belongs to the hydroxyl group, is a primary energy source; it is considered one of the metabolic tracers used in medicine. By the combination of glucose and CEST MRI technique, glucoCEST is able to detect glucose uptake through its exchangeable hydroxyl proton group(Kentrup et al., 2017; J. Wang et al., 2016) (See Figure 15). That means glucose can be used as a contrast agent in MRI.

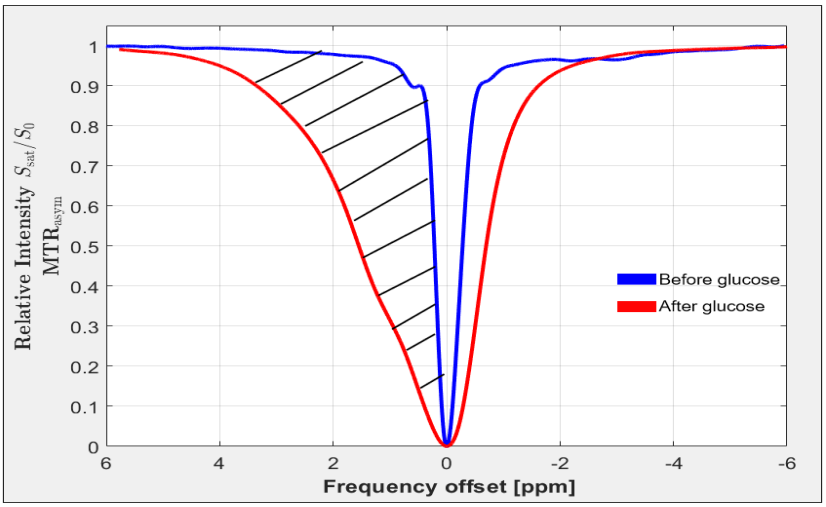

Figure 15: This graph illustrates the Z-spectrum acquired from a PBS phantom and a D-GLC phantom with a concentration of 60 mM, dissolved in PBS solution. The resonance range of glucose at 1.2, 2.1, and 2.9 ppm from water increases(Vinogradov et al., 2013). As the glucose concentration increases, the Z-spectrum broadens as the difference between the red and blue curves in the positive offset side.

2.3.3.1 D-glucose

D-glucose(D-GLC) is formed by glucose ($C_6H_{12}O_6$) that contains all -OH sites and has five distinct -OH group molecules in the structure (See Figure 16). This five distinct -OH protons are exchangeable with water proton. Glucose is also classified as an open-chain aldohexose where C-1 is a part of an aldehyde group. When dissolved in water, it forms a six-membered pyranose ring. This structure results in the C1 carbon becoming chiral, leading to two anomers, which are alpha (α) and beta (β)(De Graaf, 2007). In solution, these two major forms, α and β, have relative fractional concentrations of 0.36 and 0.64 at equilibrium conditions. It is important to note that when glucose crystals of a single anomer are dissolved, it can take several hours for the equilibrium between the anomers to be reached (de Graaf, 2007; Seidemo, 2023). This chemical shifts related to water

mainly relies on the temperature and pH of the glucose solution(S. Zhang, Trokowski, & Sherry, 2003).

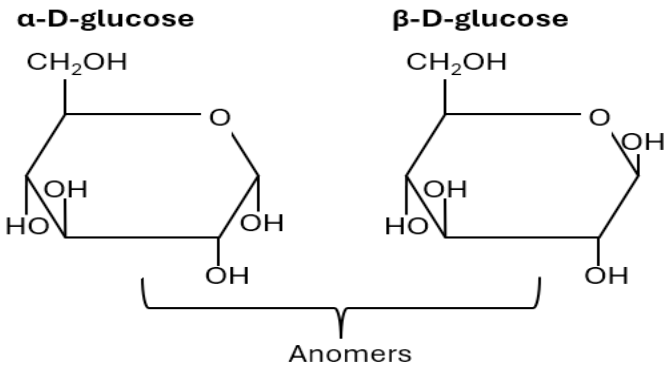

Figure 16: Glucose chemical structure and anomers

As illustrated in the figure 16 above, the -OH groups of α and β formation have several different chemical shifts from the water due to the position of the -OH group with a carbon atom. D-GLC is non-toxic and metabolizable, making it a safer contrast agent compared to ^{18}FDG which is used in PET. As the FDG competes with intrinsic D-GLC for hexokinase, inhibiting glycolysis and disrupting glucose metabolism, which can lead to cell death(Seidemo, 2023). However the applied FDG concentration is very low such as 1.0 g/kg, so it does not really compete(Rivlin & Navon, 2019). Recently, many studies have used D-GLC in monitoring and diagnosing cancer-related diseases, and it is considered a potential alternative to ^{18}FDG-PET techniques. However, it should be noted that D-GLC operates through a different mode of action compared to ^{18}FDG-PET(Consolino et al., 2020).

2.3.3.2 3-O-methyl-D-GLC (3-OMG)

3-O-methyl glucose has a similar chemical structure to D-GLC with 4-hydroxyl ($C_7H_{14}O_6$) but has one methyl group (-CH_3) (See Figure 17). 3-OMG is non-toxic, like D-GLC, but it is a nonmetabolizable derivative of glucose(Akansha Ashvani Sehgal et al., 2019). It utilizes the same transporters as D-GLC, so it competes with glucose for access to these transporter proteins. However, unlike D-GLC, 3-OMG is not further metabolized because it is not phosphorylated by hexokinase, the first enzyme involved in glucose metabolism. As a result, 3-OMG is trapped in the cell after transport, similar to radiolabeled FDG

molecules. Therefore, 3-OMG can be used as a contrast agent to measure steady-state tissue glucose concentration and assess glucose transportation.

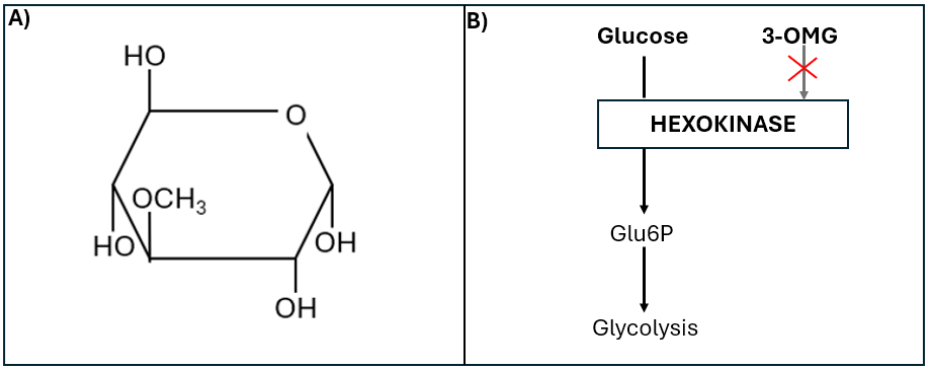

Figure 17: Chemical structures of 3-O-Methyl-D-GLC (A) and the schematic of phosphorylation pathway of Glucose and 3-OMG by Hexokinase.

2.3.3.4 CEST Data analysis interpretation and analysis

2.3.3.4.1 MTR_{asym} metrics

Post-processing of CEST data is essential for interpreting and quantifying CEST contrast(Gao et al., 2021; Murase, 2018; Vinogradov et al., 2013). To analyze the data, the CEST effect of each pool is separated. The most common method for Z-spectrum analysis is asymmetric analysis, which assumes that magnetization transfer between water molecules bound to larger macromolecules and direct saturation effects due to imperfect saturation pulses are symmetrical around the water resonance frequency. MTR_{asym} is computed by subtracting the signal intensities at two frequencies: the resonance frequency of interest and another on the opposite side of the Z-spectrum, then normalizing by the unsaturated signal. This quantifies the asymmetry between the two signals. The equation for MTR_{asym} is given by:

$$MTR_{asym} = MTR(\Delta\omega) - MTR(-\Delta\omega) = \frac{S_{sat}(-\Delta\omega) - S_{sat}(\Delta\omega)}{S_0}$$

2.3.3.4.2 Multi-Pool Lorentzian quantification method

For in-vivo studies, following segmentation and interpolation, the Z-spectra were analyzed using multi-pool Lorentzian fitting(I. Y. Zhou et al., 2017; Zhu et al., 2024). This approach improves the accuracy of component quantification and resolves peak overlap by isolating

the individual contributions to the Z-spectrum. A 5-pool model was applied using MATLAB's *lsqcurvefit* function, consisting of five inverted Lorentzian curves representing the DS, amide, amine, MT, and hydroxyl peaks. Signals were fit to the sum of 5 Lorentzian peaks:

$$Z(\Delta\omega) = 1 - \sum_{i=1}^{5} L_i(\Delta\omega). \tag{2.35}$$

Here, $\Delta\omega$ denotes the frequency offset from the water resonance, while $L_i(\Delta\omega)$ represents the Lorentzian lineshape function, expressed as:

$$L_i(\Delta\omega) = \frac{A_i}{1+\left[\frac{\Delta\omega-(\delta_{DS}+\Delta\delta_i)}{\Gamma_i/2}\right]^2} \tag{2.36}$$

Where A_i, Γ_i, and $\delta_{DS} + \Delta\delta_i$ denoted the peak amplitude, peak full width at half maximum, and the peak position, respectively. An example of starting values and boundaries conditions of the fitting parameters are presented in Table 9 of section 4.2.2.6.2.The area under the curve $AuC_{Lorentz}$ was calculated from the fitted functions, as an example shown in Figure 18, with the integration range from -6 ppm to 6 ppm.

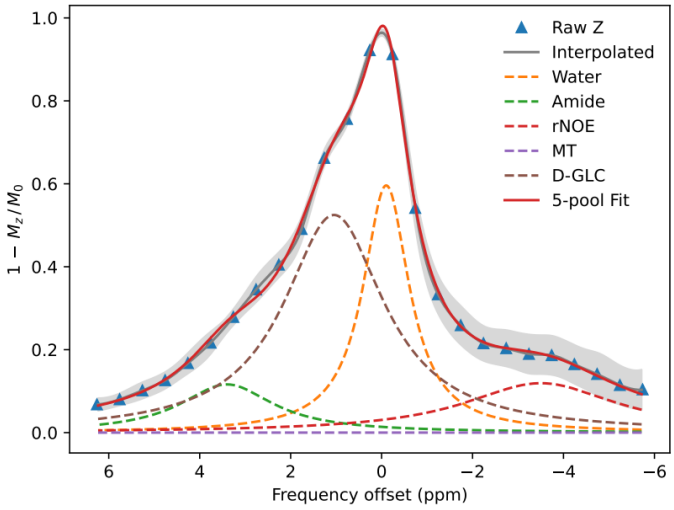

Figure 18: Representative glucoCEST Z-spectra of healthy animals in the pelvis region were obtained from pre-injection (D-GLC) to 40 minutes post-injection using the seg-FLASH sequence (with 2 µT and 1000 ms). These Z-spectra were analyzed using five-pool Lorentzian fitting with a pixel-wise method.

2.3.3.4.3 CEST data analysis procedure

According to the CEST data analysis, there are two different methods that are widely used:

1. ROI-based analysis
2. Pixel-wise analysis

2.3.3.4.3.1 ROI-based analysis

This method includes the following steps (See Figure 19):

1. Loading the data: Importing the CEST and S_0 datasets
2. Normalize the data by CEST data/baseline
3. ROI definition: Manually defining the specific region for analysis
4. Calculating signal intensity(S.I) values from the Z-spectrum
   a. Multiplying the data matrix by the ROI
   b. Averaging all signal values for each acquired frequency offset
5. B_0 correction: applying the interpolation algorithm
   a. applying the interpolation algorithm
   b. Determination of the global minimum
   c. Shifting the CEST spectrum so that the global minimum aligns with a frequency offset of 0 ppm.
6. CEST spectrum quantification: The CEST spectrum can be quantified by either MTR_{asym} or Multi-pool Lorentzian approach. The quantification is performed by calculating the area under the curve within a specific frequency offset range (MTR_{asym}) or by integrating the area under the curve over the Lorentzian function.

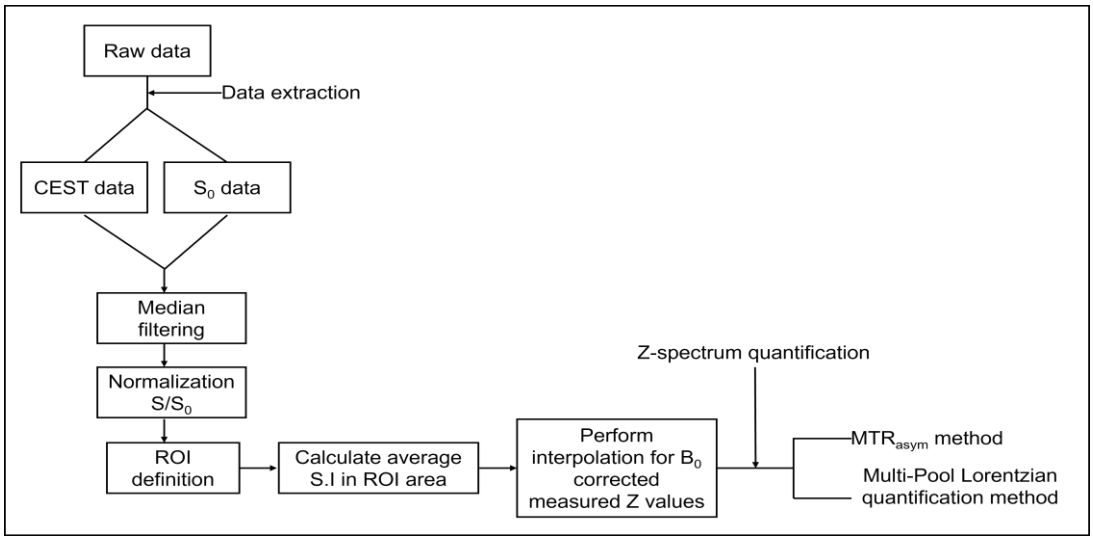

Figure 19: The diagram of voxel-based analysis pipeline

2.3.3.4.3.2 Pixel-wise analysis

In-vivo experiments, tissue regions examined by CEST often have data with low magnetic field homogeneity. Therefore, pixel-wise analysis is often used to increase the accuracy of Z-spectrum analysis and quantification. The key difference between pixel-wise and voxel-based methods is that each pixel is evaluated separately instead of averaging spectra over the ROI as in voxel-based methods. This method detects B_0 inhomogeneity-induced frequency shifts and applies B0 correction to each pixel (See Figure 20).

1. Loading the data: Importing the CEST and S0 datasets

2. Normalize the data by CEST data/baseline

3. ROI definition: Manually defining the specific region for analysis

4. At this step, step 5 from section 2.3.3.4.3.1 (ROI-based analysis) is applied to each pixel within the ROI

5. Global Z-spectrum calculations:

   a. Identifying the shared frequency range across all pixel-wise CEST spectra, accounting for potential variations due to B_0-related shifts.

   b. Averaging signal values at each frequency offset within this range, normalized to the fixed size of the ROI.

6. The quantification step based on the global CEST spectrum: The CEST spectrum can be quantified by either MTR_{asym} or Multi-pool Lorentzian approach. The quantification is performed by calculating the area under the curve within a specific frequency offset range (MTR_{asym}) or by integrating the area under the curve over the Lorentzian function.

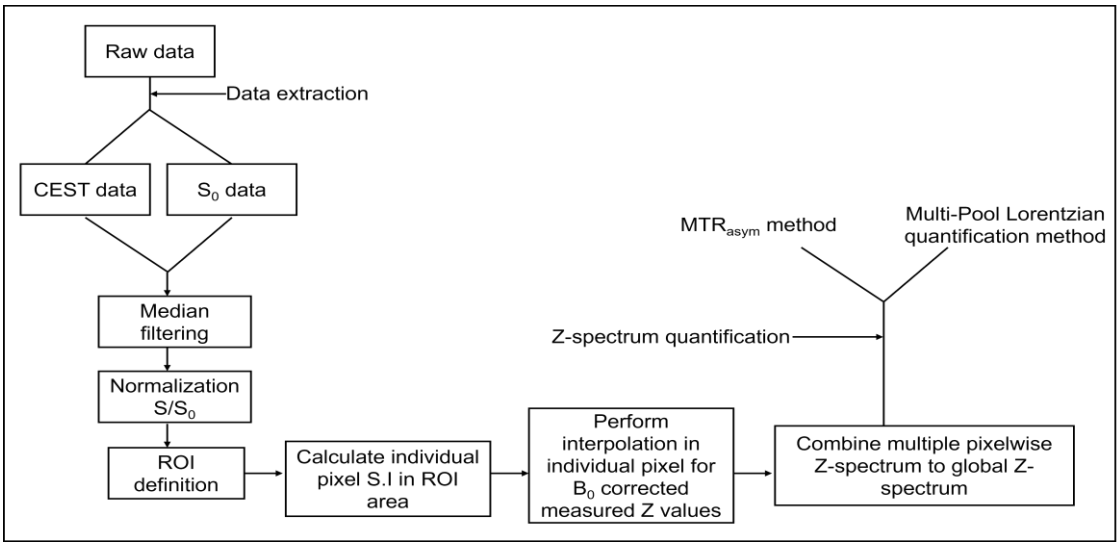

Figure 20: The diagram of pixel-wise analysis pipeline

3. Study 1: The application of CEST MRI in adipose tissue

3.1 Introduction

3.1.1 The anatomy and physiology of adipose tissue

3.1.1.1 White adipose tissue and brown adipose tissue

Adipose tissue is a connective tissue primarily composed of fat cells (adipocytes) and other cell types such as pre-adipocytes, macrophages, endothelial cells, fibroblasts, and leukocytes (Kwok, Lam, & Xu, 2016). It plays a vital role in energy storage and acts as a mechanical and thermal insulator. Fats are made up of long-chain triglycerides with three fatty acid chains. Mammals have three main types of adipose tissue: WAT, BAT, and beige adipose tissue.

WAT is the most abundant adipose tissue in the human body, primarily located in the visceral and subcutaneous depots (Figure 21B). It is spherical, consisting of large lipid vacuoles and various cell types, including immune cells (macrophages, neutrophils, lymphocytes), mesenchymal cells, and endothelial cells. WAT's main function is energy storage as fat and thermal insulation(Trayhurn & Beattie, 2001). It also acts as an endocrine organ and protects internal organs. After meals, fats are broken down into fatty acids and monoglycerides, and WAT stores lipids as triglycerides, which fuel body processes. Excessive white fat leads to obesity (Avram, Avram, & James, 2005).

Brown adipocytes, found in BAT (Figure 21A), differ from WAT in structure. BAT is located in the interscapular (iBAT), subscapular (sBAT), and cervical (cBAT) depots, with small amounts in perivascular structures, the epicardium, and kidneys. BAT has multiple small lipid droplets and abundant mitochondria. The triglycerides stored in these droplets serve as the primary fuel for non-shivering thermogenesis during cold exposure. BAT's metabolite exchange with mitochondria is more efficient than WAT's due to its increased lipid droplet surface area(CANNON & NEDERGAARD, 2004). BAT contains uncoupling protein 1, which uncouples oxidative phosphorylation from ATP production, generating heat instead of ATP. This thermogenesis process helps maintain energy balance and regulates glucose and fat metabolism(CANNON & NEDERGAARD, 2004). BAT also has more capillaries than WAT, facilitating oxygen and nutrient delivery and heat distribution. Its characteristic color comes from its higher mitochondrial iron content. In addition to BAT and WAT, the body also contains a type of fat called beige adipocytes(J. Wu et al., 2012). These cells have a structure similar to BAT but are located within WAT. Beige adipocytes

emerge in response to increased heat production demands, such as β-adrenergic stimulation, diet, or cold exposure. This process is known as browning(Chang et al., 2022).

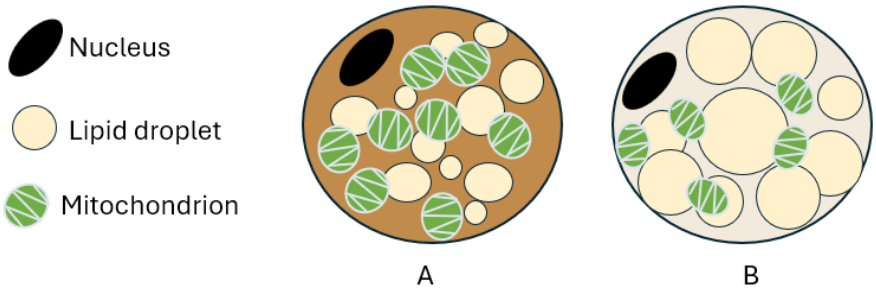

Figure 21: General characteristics of brown (A), white adipose tissue (B)

3.1.1.2 non-shivering thermogenesis

Adipose tissue functions as an endocrine organ that regulates glucose and lipid metabolism. When environmental temperatures fall below the thermoneutral range, BAT thermogenesis is triggered by sympathetic nervous system (SNS) stimulation. The SNS releases norepinephrine (NE), which activates β3-adrenergic receptors on brown adipocytes. This activation increases energy expenditure through mitochondrial uncoupling, where electrons bypass ATP production and generate heat instead, a process known as non-shivering thermogenesis. Fatty acids from triglycerides are the primary fuel for oxidation in brown mitochondria, while glucose serves as an important energy substrate. During cold exposure, glucose transporters (GLUT) 1 and 4 are activated in BAT, promoting glucose uptake for metabolism via glycolysis and mitochondrial oxidation(Maliszewska & Kretowski, 2021). In glycolysis, glucose is first phosphorylated by hexokinase 2 (HK2) into glucose-6-phosphate, which is then metabolized into pyruvate. Glucose also contributes to lipogenesis in BAT by providing carbon for glycerol and acetyl-CoA production. Recent studies using ^{18}F-FDG PET imaging, hyperpolarized [1-13C]pyruvate, and ^{129}Xenon uptake confirm active glucose metabolism in BAT(Branca et al., 2014).

3.1.2 MRI in the assessment of adipose tissue

3.1.2.1 Lipids in MRI and single-voxel MR spectroscopy

Triglycerides are the primary fat storage form in the body, composed of long-chain triglyceride molecules made up of glycerol and fatty acids. There are two main types of fats: saturated fatty acids, which contain twelve hydrogen atoms, and unsaturated fatty

acids, which have ten hydrogen atoms, two less than the maximum. Due to the different molecular environments of nuclei (chemical shift), lipids produce MR signals at different frequencies(Hamilton, Smith Jr, Bydder, Nayak, & Hu, 2011; Zancanaro et al., 1994). Triglyceride can be visualized by ^{1}H MR spectroscopy up to ten different peaks depending on the strength of the static magnetic field and T_2* (See Figure 22). The difference lipids peaks are assigned to their corresponding chemical position.

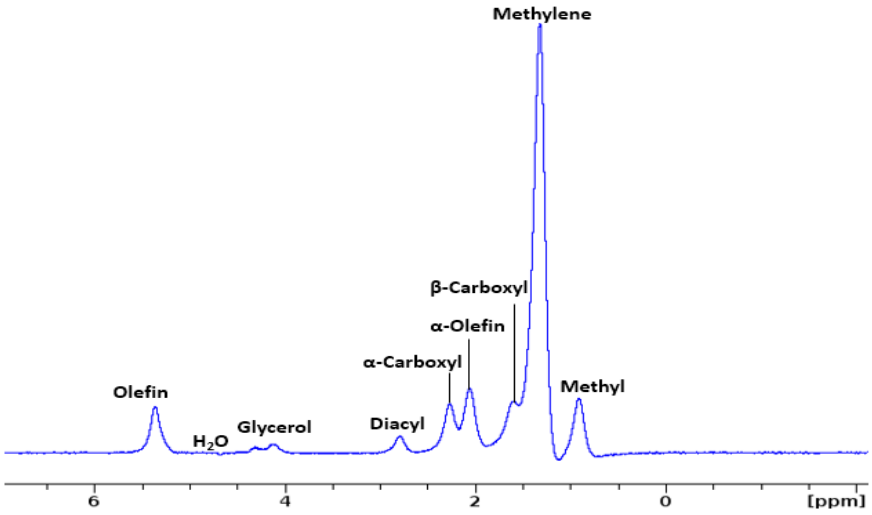

Figure 22: Schematic illustration of a triglyceride molecule was done by ^{1}H MR spectroscopy technique with water suppression mode

3.1.2.2 T_1, T_2 mapping

T_1 and T_2 mapping generates a parametric map from a series of images acquired at various relaxation times, which are longitudinal and transversal. They reflect two principles of mechanism in MRI: the time requirement for longitudinal magnetization back to equilibrium status and the loss of phase coherence of transverse magnetization. The relaxation times of tissues can reflect their different compositions(P. K. Kim et al., 2017). Therefore, T_1 and T_2 mapping techniques can be a potential quantitative biomarker for distinguishing tissue components based on the differences in their relaxation times(Nikiforaki & Marias, 2023).

3.1.2.3 Diffusion MRI

As introduced in section 2.2.2.3, DWI is a non-invasive imaging method of signal generation based on measuring the random Brownian motion of water molecules within a voxel of tissue. It can reflect insight into the microstructure of the tissues. Due to the

structural differences (as introduced in section 3.1.1) and the diffusion properties of fat being 100 times slower than water, water in WAT will be more restricted than in BAT. This results in WAT showing higher intensity signals than BAT in DWI, as seen in Figure 23(Steidle, Eibofner, & Schick, 2011).

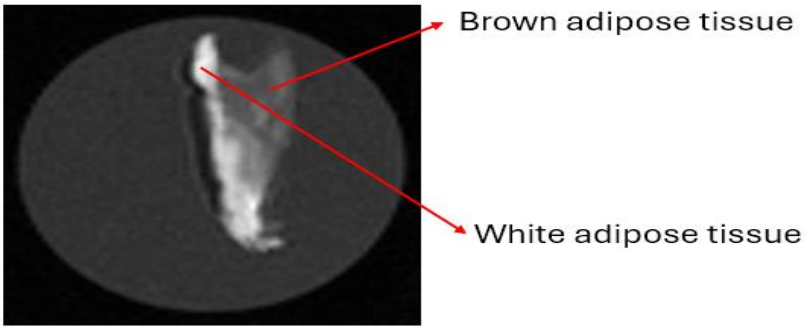

Figure 23: An example of DWI with b value = 650 s/mm^2 on adipose tissue. Because of the structural differences between the two types of adipose tissue in terms of lipid droplets, there is a difference in diffusion. In this figure, WAT has a higher signal than BAT.

3.1.3 Hypothesis and study objectives

According to the adipose tissue morphology, WAT has less extracellular and intracellular water content than BAT, which leads to WAT's lower water-to-fat ratio in comparison to BAT(Avram et al., 2005). Moreover, vascular structures and iron-rich mitochondria in BAT make the difference between BAT and WAT in terms of T_2, T_2*, and T_1 relaxation times and diffusion attenuation(Nikiforaki & Marias, 2023; Verma et al., 2017). Therefore, MRI enables quantifying the water-fat composition based on these features to characterize and differentiate BAT from WAT(Hamilton et al., 2011).

Since BAT plays an essential role in the body in terms of thermoregulation and especially metabolism, the morphology and quantification of BAT function is key for researchers to understand better the influence of BAT on metabolic disorders such as obesity or diabetes, thereby investigating appropriate treatment directions(Cypess et al., 2015; Walker et al., 2024).

Currently, PET imaging with ^{18}FDG has been the gold standard for measuring glucose uptake in BAT(Ricci et al., 2023). PET imaging works by using radiotracers like FDG, which mimic glucose, allowing researchers to visualize and quantify glucose uptake in active tissues such as BAT. However, PET imaging comes with significant drawbacks, particularly the exposure of patients to ionizing radiation(Nievelstein et al., 2012).

Repeated imaging, as is often necessary in longitudinal studies or clinical settings, poses increased health risks due to the cumulative radiation dose(Hosono et al., 2021).

CEST MRI is a non-ionizing imaging technique that can address this limitation. It can provide structural information of adipose tissue, which can be used to differentiate between BAT and WAT based on the structural differences between these two types of tissue. Additionally, the method utilizes the natural proton exchange between molecules, enabling the use of endogenous or biodegradable compounds like D-GLC as contrast agents. This not only provides further information to distinguish the two tissue types through glucose uptake, which is influenced by the vascularization structure of BAT, but also enables the study of the metabolic function of BAT.

We propose that CEST MRI and glucoCEST MRI have the potential to address the technical limitations of current imaging techniques by producing both structural and metabolic contrast, enabling measure BAT at rest and post activation.

Aim 1: To utilize CEST and glucoCEST MRI to characterize BAT and WAT by providing structural contrast

Aim 2: To demonstrate the capability of glucoCEST MRI in detecting BAT activation, thereby providing insights into the functional aspects of BAT.

Aim 2.1: Evaluating glucose uptake in brown adipose tissue using glucoCEST MRI, comparing two injection techniques: intravenous (i.v.) and intraperitoneal (i.p.).

Aim 2.2: Evaluating how glucose uptake changes when BAT is activated on ex vivo study (fresh tissue resembles vivo conditions).

3.2 Material and methods

This study was divided into two phases.

Phase 1: Implement CEST in ex vivo studies, followed by the application of glucoCEST in in vivo studies.

Phase 2: Apply glucoCEST in in vivo studies and later implement glucoCEST in ex vivo studies (fresh tissue resembling in vivo conditions).

3.2.1 Phase 1: Characterization of adipose tissue by CEST MRI

3.2.1.1 Animal preparation and MRI protocols

The tissues for ex-vivo studies were dissected from two male healthy C57BL/6 mice with an average age of 9 weeks. Lean muscle tissue from the flank, WAT from the visceral

area and BAT from the interscapular depot. These tissues were fixed separately into tubes with agarose 1%.

The study was induced by vertical Bruker 9.4T preclinical scanner (MRI protocols are shown in Table 2). A CEST sequence was used to acquire Z-spectra with various saturation pulse amplitude from 0.5μT to 3μT (interval:0.5μT) with the saturation time in the range 500 ms, 1000 ms, 2000ms and 3000 ms and frequency offsets ranging from -6ppm to 6ppm at interval of 0.25ppm, together with ±12ppm offsets. The saturation pulse was followed by RARE readout with parameters: Resolution: 0.3 x 0.3 mm^2, RARE factor = 16, TR = 37 ms, TE = 2580 ms

	Sequence type	TR (ms)	TE (ms)	Average	Resolution	b-values/echo/repetition time/others
1	DWI	500	20	2	0.156x0.156mm^2	0;650
2	MRS (PRESS)	2500	16.5	256	0.7x0.7x0.7mm^3	Water suppression
3	T_1 mapping	1	/	4	0.156x0.156mm^2	6
4	T_2 mapping	/	3.36	1	0.156x0.156mm^2	10

Table 2: The MRI sequences parameters that are used in the study

3.2.1.2 Data processing

All the acquired data were analyzed by using an in-house developed MATLAB environment (MathWorks, Natick, MA). Data are presented as mean ± SD unless otherwise stated.

- **T_1, T_2 mapping**

To determine the T_1 and T_2 relaxation time constants, the data were processed and analyzed using their respective models. For T1, the signal intensities were modeled as:

$$S = S_0\left(1 - e^{-\mathrm{TR}/T_1}\right),$$

Where S represents the measured signal intensity, S0 the fully recovered signal, and T1 the relaxation time constant.

For T_2, the decay was modeled as:

$$S = A_1 e^{-\mathrm{TE}/T_2} + A_3,$$

Where S is the measured signal intensity, A1 is the initial amplitude, T_2 the relaxation time constant, and A3 an offset parameter.

The extracted data were fitted to their respective models using non-linear least-squares fitting to estimate the relaxation time constants. Initial fitting parameters were S0= 60, T_1= 1000 ms, A1= 1, T_2= 10ms, and A3= 9.

Regions of interest (ROI) were manually selected using binary masks on average slice images. The mean signal intensities within the ROI were extracted across different repetition times (TR) for T_1 mapping and across multiple echo times (TE) for T_2 mapping.

All MR T_2 mapping data were analyzed by using Segment Medviso AB (version 3.3 R10187c).

- **CEST quantification**

The Z-spectrum is analyzed through a ROI-based Lorentzian fitting approach. The pipeline is described in the following steps:

1.Loading the data: Importing the CEST and S0 datasets

2.Normalize the data by CEST data/baseline

3.ROI definition: Manually defining the specific region for analysis

4.Calculating signal intensity values from the Z-spectrum

a. Multiplying the data matrix by the ROI

b. Averaging all signal values for each acquired frequency offset

5. B_0 Correction and Normalization

a. Uses spline interpolation to create a smoother frequency response over an extended range

b. Finds the minimum value in the spectrum of water and shifts the frequency offsets accordingly to correct for B_0 inhomogeneity.

6. Plot the data

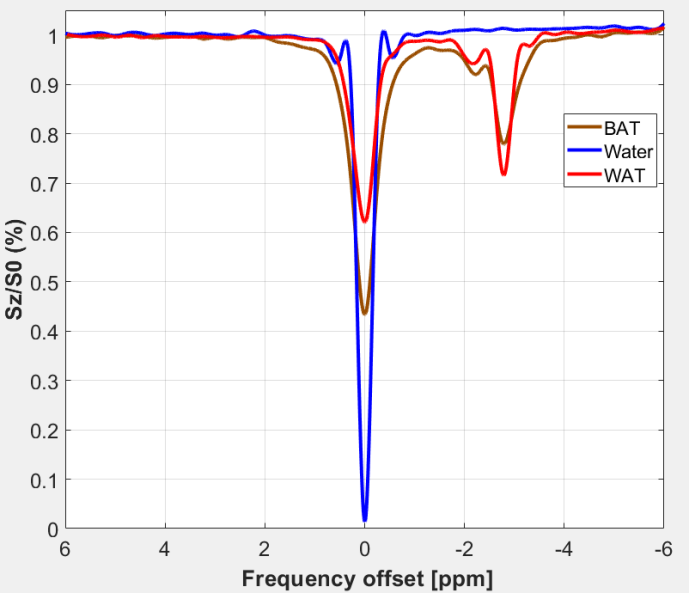

Figure 24: An example of Z-spectrum of adipose tissue: The plot illustrates the normalized signal intensity (Sz/S0) as a function of frequency offset (ppm) for different tissue types. The brown curve represents BAT, the blue curve shows water (reference signal), and the red curve represents WAT. After defining the ROI at the corresponding object region, the interpolation algorithm is applied to the data. The minimum value of the water spectrum is then found, identifying the peak with the higher amplitude between the two peaks, which is shifted to the offset position of 0 ppm.

3.2.2 Phase 2: Evaluation brown adipose tissue glucose uptake by CEST MRI

3.2.2.1 Animals

All experiments followed the National Institute of Health Guidelines for the Care and Use of Laboratory Animals (eighth edition) and the European Community Council Directive for the Care and Use of Laboratory Animals of 22 September 2010 (2010/63/EU). The study protocol was approved by the competent State Office for Food Safety and Consumer Protection (TLLV, Bad Langensalza, Germany; local registration number: 81-02.04.2021.A327).The study included 12 male C57BL/6 mice with an average age of 9 weeks. The animals were housed in a 12-hour light-dark cycle environment, provided with sufficient chow and water.

3.2.2.2 Experiment protocols

3.2.2.2.1 Animal Preparation

Animals were divided into 2 groups. In the first group (n = 6) mice underwent dynamic glucoCEST MRI before and after intravenous administration (i.v) of 3 doses of 12 mmol/kg

glucose with 3 subsequent acquisitions between 30 to 90 minutes post-injection (See Figure 25). The second group (n = 6) was scanned using the same protocol (i.e. dynamic series of 3 scans) before and after the intraperitoneal administration (i.p) of 4 and 6 mmol/kg glucose (See Figure 25). The blood glucose level was measured using a blood glucose meter. The animal was placed in a mouse cradle in supine position. During the MRI experiments, the mice were anesthetized with isoflurane (1-2%). A feedback-controlled warm-water heating system measured core body temperature with a rectal probe and maintained at 37 ℃. Respiratory gating, utilized to suppress breathing artifacts, involved continuous respiration monitoring. It ensured synchronization of data acquisition with the respiratory cycle by maintaining a rate of 35 ± 5 respiration cycles per minute. This was achieved by controlling the gas flow (air and isoflurane), ensuring accurate synchronization, and minimizing potential distortions in the acquired data.

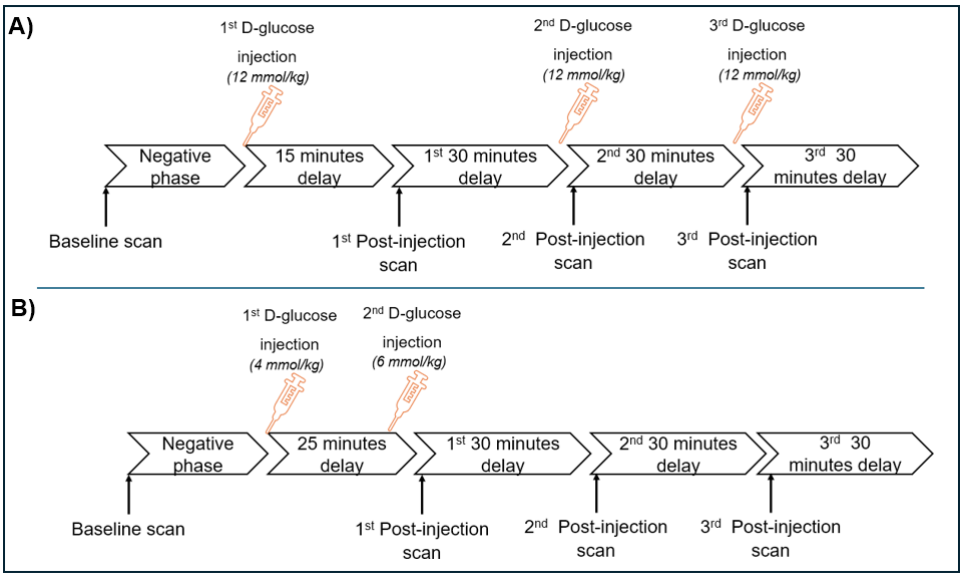

Figure 25: Schematic illustrations of the experimental setting and glucoCEST data acquisition schemes for both (A) i.v and (B) i.p. glucose administration. Each image series started with a pre-administration baseline image, followed by glucose injection protocols, and post-injection examination periods.

3.2.2.2.2 Ex-vivo study preparation

Two mice were sacrificed, and adipose tissue along with myocardium was harvested. For BAT activation, NE, a hormone released from SNS, activates β3-adrenergic receptors on brown adipocytes. In this study, NE was used at a concentration of 10 mM. To prepare a 1.5 M glucose solution, 5.4 grams of D-GLC was dissolved in 20mL of PBS. This solution

with 1.5 M glucose concentration was used for the experiment. The BAT and WAT were placed together in the same Eppendorf tubes, while the myocardium was stored separately in another tube. The tissues were scanned within two hours to ensure they remained viable. Each tissue underwent two scans across three phases:

- Negative phase: The tubes were filled with PBS.

- Glucose phase: The tubes were filled with a 1.5 M glucose solution.

- Stimulation phase with glucose: The same 1.5 M glucose solution was used, with the addition of 15 µL of NE.

3.2.2.2.3 MRI parameters

- **In-vivo Z-spectrum imaging**

A respiratory-gated CEST-RARE sequence was applied using a series of 5 Gaussian saturation pulses. Each pulse had a duration of 100 ms and was separated by a 0.010 ms inter-pulse delay with B_1 amplitude = 2 µT. The experiments were conducted at a 11.7T preclinical system (Bruker MR system BioSpec USR 117/16) with a cryoprobe serving as the trans-receiver coil. Saturation frequencies were applied in a range from -6 to +6 ppm at intervals of 0.5 ppm. S0 was set to 20ppm. Imaging parameters included: TR=1100 ms, TE=37.40 ms, RARE-Factor=16, Echo Spacing= 4.676 ms, Slice Thickness = 1 mm, Resolution= 260x260 mm^2.

- **Ex-vivo Z-spectrum imaging**

The glucoCEST parameters and set up was used similarly to in-vivo study

3.2.2.3 Data processing

All the acquired data were analyzed by using an in-house developed MATLAB environment (MathWorks, Natick, MA). Data are presented as mean ± SD unless otherwise stated.

- **CEST quantification**

The Z-spectrum is analyzed using a ROI-based Lorentzian fitting method. In the Z-spectrum analysis of the fat region, the frequency of fat will shift the entire spectrum and determine the offset 0 as the fat peak instead of the water peak. Therefore, the conventional quantification method will not be accurate. Therefore, the half-Lorentzian

method is applied to calculate the glucose uptake in adipose tissue. The pipeline is described in the following steps: This method includes the following steps:

1. Loading the data: Importing the CEST and S_0 datasets
2. Normalize the data by CEST data/baseline
3. ROI definition: Manually defining the specific region for analysis
4. Calculating signal intensity values from the Z-spectrum

a. Multiplying the data matrix by the ROI

b. Averaging all signal values for each acquired frequency offset

5. Extract the Frequency Offset Range
    a. The indices corresponding to frequency offsets of -3.4 is identified (based on the frequency offset of Fat)
    b. The spectrum is truncated to this range, then normalized by subtracting the minimum value and scaling to a range of 0 to 1.
6. B_0 correction: applying the interpolation algorithm
    a. applying the interpolation algorithm
    b. Determination of the global minimum
    c. Shifting the CEST spectrum so that the global minimum aligns with a frequency offset of 0 ppm.
7. Mirror the Left Side of the Spectrum
    a. The left side of the spectrum is extracted from the minimum intensity point
    b. A mirrored version of this segment is created and concatenated to the original left-side spectrum
8. Final Normalization and Combination of Corrected Data
    a. The left and right mirrored components are normalized separately
    b. They are concatenated to form a fully corrected and normalized spectrum
9. Find the minimum intensity: identify the lowest point in the corrected spectrum and its index
10. Compute asymmetry index and the area under the curve is obtained by summing asymmetry values over a defined range of offset of glucose (0.5 ppm to 3 ppm).

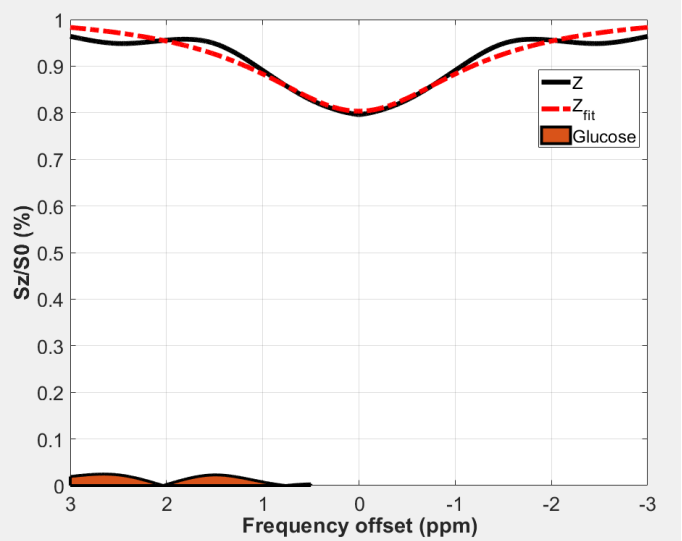

Figure 26: Representative Z-spectrum of healthy animals at the BAT region obtained post D-GLC injection. The black curve represents the Z-spectrum (raw data), the red dashed curve shows the fitted Z-spectrum (Zfit), and the orange curve indicates the glucose-related signal. The figure demonstrates the processing pipeline, which includes data normalization, ROI definition, B_0 correction, and spectrum mirroring, ultimately leading to a fully corrected and normalized Z-spectrum. The signal intensity values are calculated, and the asymmetry index is derived from the glucose-related region between 0.5 ppm and 3 ppm

3.2.2.4 Statistical analysis

All statistical analyses were performed using GraphPad Prism (version 9; GraphPad Software, Boston, MA, USA). Mann–Whitney U test was used to test the significance of the difference between the parameters of i.v and i.p groups. P <0.05 was considered statistically significant.

3.3 Results

3.3.1 Phase 1: Characterization of adipose tissue by CEST MRI

- ***Reference MRI techniques to distinguish the type of adipose tissue***

In this validation, we performed DWI, T_1, T_2 mapping to visualize the BAT and WAT based on structural differences between BAT and WAT, their signal intensities vary across different MRI weightings, allowing us to distinguish between them, as shown in Figure 27.

In the DWI images (Figures 27A & B), the distinction between BAT and WAT is clearly visible. This difference arises from the variation in water motion restriction in the two tissue types. Specifically, WAT shows more restricted water motion compared to BAT, which is

a result of WAT being less hydrated, containing more fat, and having larger unilocular fat droplets. In Figure 27B, when the diffusion weighting is low (b = 0 s/mm^2), the image represents the baseline without diffusion weighting, resembling typical T2-weighted images. In Figure 27A, at a higher b-value (b = 650 s/mm^2) it is more sensitive to slower-moving water molecules, which results in smaller diffusion distances and a higher diffusion weighting. This higher b-value shows the restricted water motion in WAT more than in BAT. As a result, WAT shows higher diffusion weighting compared to BAT.

In the T2-weighted image (Figure 27C) and DWI (Figure 27B), the S.I of BAT is lower than that of WAT, but WAT in Figure 27 shows higher S.I than DWI with b = 0 s/mm^2 . This is due to the acquisition of T2-weighted images using turbo spin-echo TSE sequences, where fat (such as in WAT) remains bright due to the J-coupling effects(Henkelman, Hardy, Bishop, Poon, & Plewes, 1992), making WAT appear brighter compared to BAT.

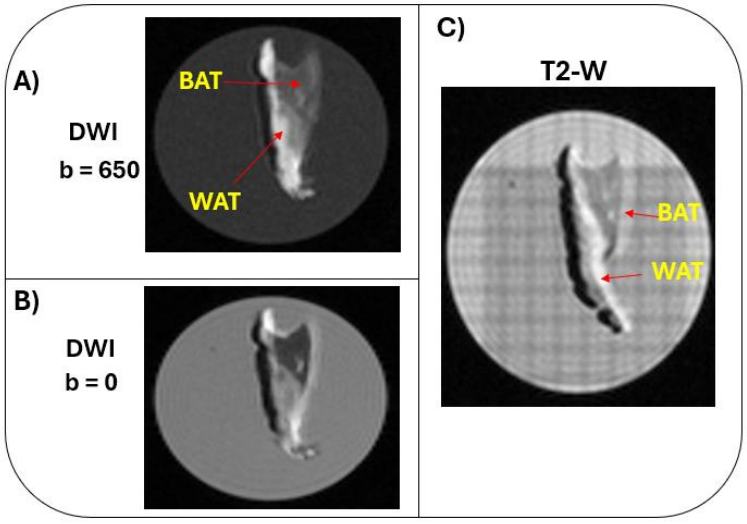

Figure 27: The illustration of the adipose tissue samples from interscapular region, which know BAT depot in rodent. This sample was embedded in PBS and measured with multiples MRI techniques: diffusion weighted image (A and B) and T_2 weighted images (C).

This structural difference also changes the T_1 and T_2 relaxation times of the tissue (see Table 3). The mean T_1 values for BAT were significantly higher than those of WAT (P <0.01), while the T_2 values of BAT were significantly lower than those of WAT in the ex-vivo samples (P < 0.01). The T_2 of BAT is notably shorter than that of WAT, indicating distinct relaxation characteristics different due to the paramagnetic nature of iron in BAT disturbs the local magnetic field and accelerates the process of T_2 relaxation.

Parameter (ms)	BAT	WAT	P value
	Mean ± SD	Mean ± SD	
T_1	1066.333±134.546	819.167±73	<0.01
T_2	39.193±3.636	314.272±24.855	<0.01

Table 3: The comparison of T_1, T_2 relaxation time between BAT and WAT. Values are presented as mean ± standard deviation.

Figure 28A shows the anatomical image of interscapular tissue based on the T_2w image, with BAT and WAT ROI distinctly identified. The T_1 relaxation time curves are presented in Figure 28B and 28C, respectively. Both tissues show typical T_1 recovery behavior, with SI increasing non-linearly over time. The T_2 relaxation time curve for BAT is shown in Figure 28D, while the curve for WAT is presented in Figure 28E. BAT shows a higher signal intensity and a slower decay rate than WAT, suggesting the difference in relaxation properties can reflect structural differences.

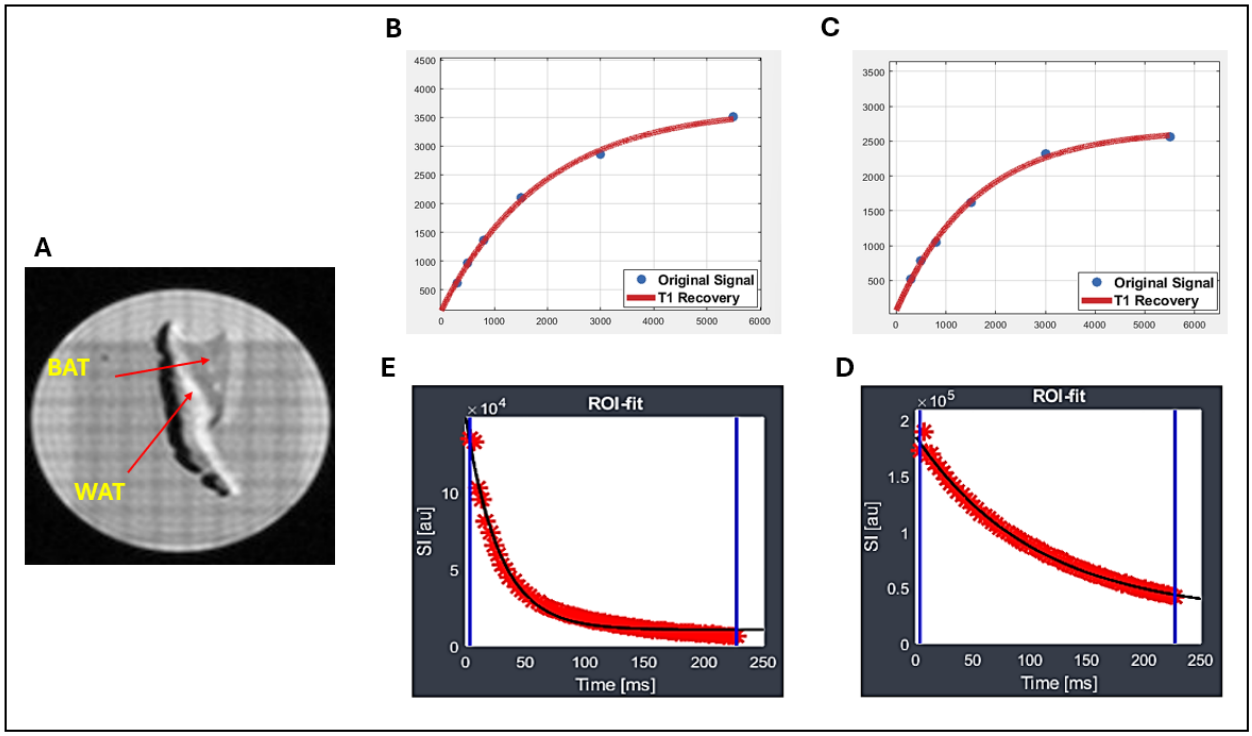

Figure 28: The illustration of interscapular adipose tissue sample. This sample was embedded in PBS and measured with MR T_1, T_2 mapping technique. (A) the anatomical structure of interscapular tissue; (B) T_1 relaxation curve of BAT; (C) T_1 relaxation curve of WAT; (D) T_2 relaxation curve of BAT; (E) T_2 relaxation curve of BAT.

In addition to differentiating the BAT and WAT by imaging, we also measured the MRS on adipose tissue. MRS was utilized to investigate adipose tissue in this study. Figure 29 reports the ^{1}H MRS spectrum of BAT (Figure 29A) and WAT (Figure 29B). The spectrum of WAT sample is better than a BAT sample in terms of spectral resolution. This difference is due to the higher iron content in BAT and the more homogeneous tissue structure of WAT. The most dominant peak observed in both spectra is the methylene group (~1.3 ppm). Other prominent resonances are demonstrated in the table beside the spectrum. In addition, the spectrum of WAT reveals the presence of an additional peak at 1.59 ppm and 4.10 ppm, corresponding to the β-carboxyl and glycerol resonance, located adjacent to the methylene peak (Figure 29C). Notably, this characteristic peak, labelled “C,G” is absent in the BAT spectrum, which reflecting the increased fat fraction in WAT. This spectral distinction further highlights the biochemical differences between BAT and WAT.

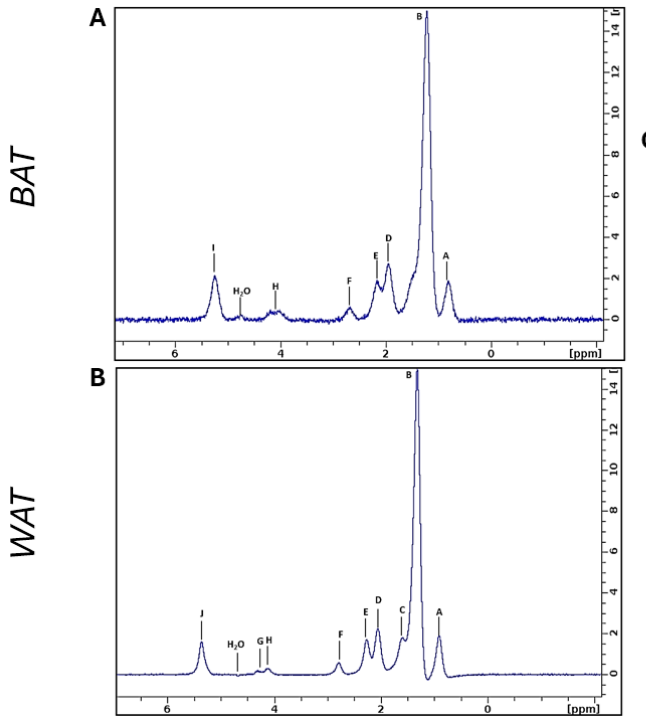

C

Peak	Chemical shift (ppm)	Type
A	0.90	Methyl
B	1.30	Methylene
C	1.59	β-Carboxyl
D	2.03	α-Olefin
E	2.25	α-Carboxyl
F	2.77	Diacyl
G	4.10	Glycerol
H	4.30	Glycerol
I	5.21	Glycerol
J	5.31	Olefin

Figure 29: ^{1}H MR spectroscopy (PRESS) of BAT(A) and WAT(B) water suppression technique was measured at a 9.4T machine. Nine peaks are resolvable by spectroscopy at 9.4T in WAT. Compared with WAT, two peaks are missing in BAT spectra (peak C at 1.59 ppm and peak G at 4.10 ppm). Resonance is assigned to protons of fatty acid chains and glycerol, which are underlined and identified by the letter (A-J) in the table (C). The table of fat peaks assignment frequencies was adapted from (Peterson, Trinh, & Månsson, 2021)

- ***CEST parameters validation***

The phantom containing interscapular tissue embedded in PBS (Figure 30A) was used to determine the optimal saturation power and time for distinguishing different adipose tissue types. In the Z-spectrum with saturation pulse powers ranging from 0.5 μT to 1.5 μT at a saturation time of 1000 ms (Scotti et al., 2018), BAT showed two distinct peaks at 0 ppm and approximately -3.4 ppm (Figure 30B). As B1 amplitude increased, the fat peak at -3.4 ppm became comparable to the water peak, especially at 1.5 μT, making it difficult to differentiate between fat and water peaks in tissues like muscle, BAT, and WAT. This overlap complicated data processing, so a B1 of 0.5 μT was chosen.

Further validation of saturation time with a fixed B1 of 0.5 μT revealed that the BAT spectrum peak became sharper and more defined at 3000 ms saturation time (Figure 29C). A small peak also appeared at -2.2 ppm in addition to the characteristic peak at -3.4 ppm. Therefore, the optimized parameters of B1 = 0.5 μT and saturation time = 3000 ms were selected for subsequent ex-vivo adipose tissue experiments.

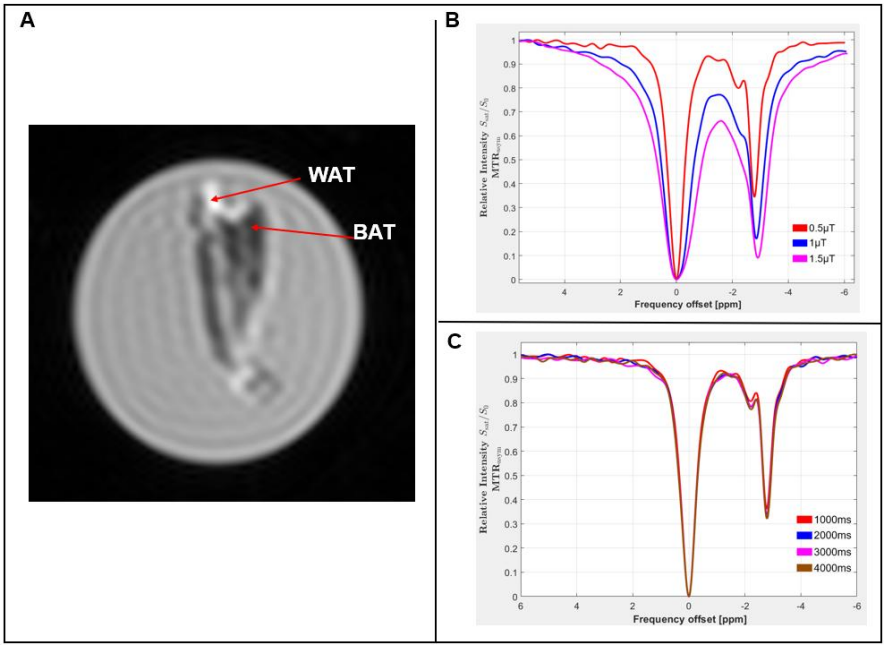

Figure 30: The effect of the B_1 amplitude and saturation time parameters on the CEST spectrum of BAT. (A) the anatomical image of interscapular tissue that embedded in PBS based on T_2W image, the red arrow indicates the BAT. (B)The Z-spectrum of BAT varies according to multiple B_1 saturation amplitude from 0.5 μT to 1.5 μT with a saturation time of 1000 ms. (C) The change of the Z-spectrum of BAT is based on the variation of saturation from 1000 ms to 4000 ms. With the parameters 0.5μT and 3000ms, the peak of BAT is more visible than the other parameters.

- ***Implementation of finalized CEST parameters for BAT and WAT distinguish***

Figure 31 shows the representative Z-spectra of BAT, WAT from the extracted tissues with the optimized parameters. Z-spectra shows two prominent peaks corresponding to the water and lipid direct saturation. In the WAT area, the main peak was from methylene protons at -3.5 ppm relative to the water resonance set at zero ppm. In WAT, the fat peak appears larger than in BAT due to the higher fat content in WAT. In contrast, the water dip in WAT is smaller compared to BAT due to the lower water fraction in WAT(Franz et al., 2018). In addition, a small peak occurs at the frequency offset around -2 ppm appears in both BAT and WAT. It might be the other triglycerides peaks which are relevant to the peaks shown in Figure 31. The Z-spectrum was obtained for the three areas: water, BAT and WAT, clearly showing the difference in fat content.

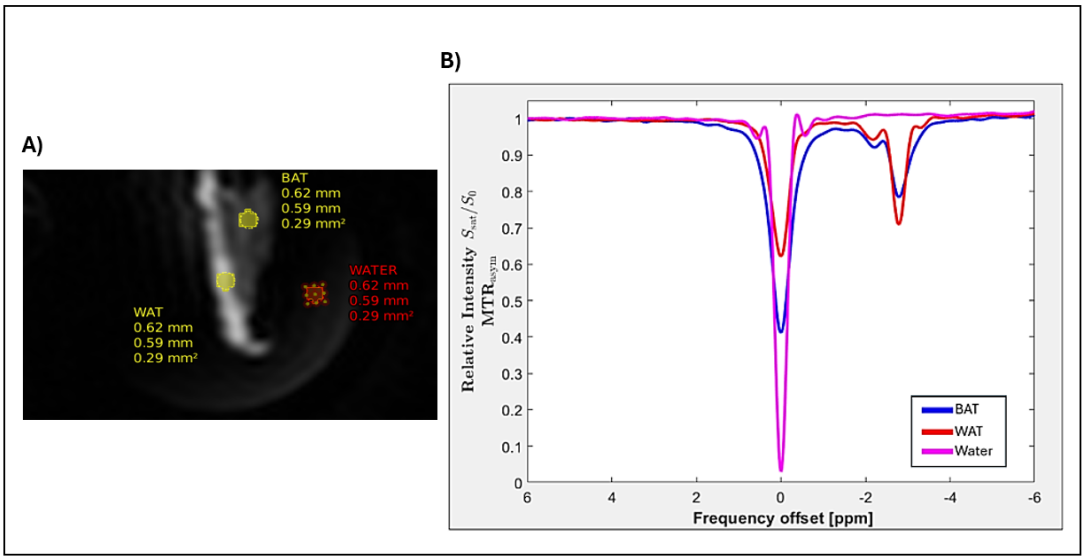

Figure 31: CEST spectrum from the extracted mice adipose tissue in the interscapular region. The ROIs were drawn at WAT, water and BAT (A). The purple curve represents the water peak as reference; the blue and red curves represent the BAT and WAT, respectively (B).

3.3.2 Phase 2: Evaluation brown adipose tissue glucose uptake by CEST MRI

- **Glucose administration validation**

To investigate the differences between i.v. and i.p. glucose administration methods, as well as the effects of varying glucose concentrations. Mice underwent i.v administration at doses of 12 mmol/kg glucose and i.p glucose administration at doses of 4 and 6 mmol/kg glucose with two injections. The blood glucose was measured by blood test kits over

multiple time points from pre-injection to post-injection 90 minutes (See Figure 32A) to differentiate two types of injection.

For glucose concentration evaluation, the i.v was applied, and blood glucose was monitored from 0 minutes to 180 minutes (See Figure 32B). The graph shows i.v. injection causes a rapid increase in blood glucose, peaking at 600 mg/dL at 20 minutes, followed by a decline and stabilization around 400 mg/dL. In contrast, i.p. injection gradually rises, reaching and stabilizing at 400–450 mg/dL from 40 minutes onward. This highlights faster but transient glucose elevation with i.v. and slower, sustained elevation with i.p; Figure 32B indicates a similar elevation of blood glucose at 30 minutes post-injection in both concentrations as 12 mmol/kg(red color) and 16 mmol/kg(black color) around 580-600mg/dL. The blood glucose of both concentrations rapidly declines from minute 30 to 120 and stabilizes around 180-200 mg/dL.

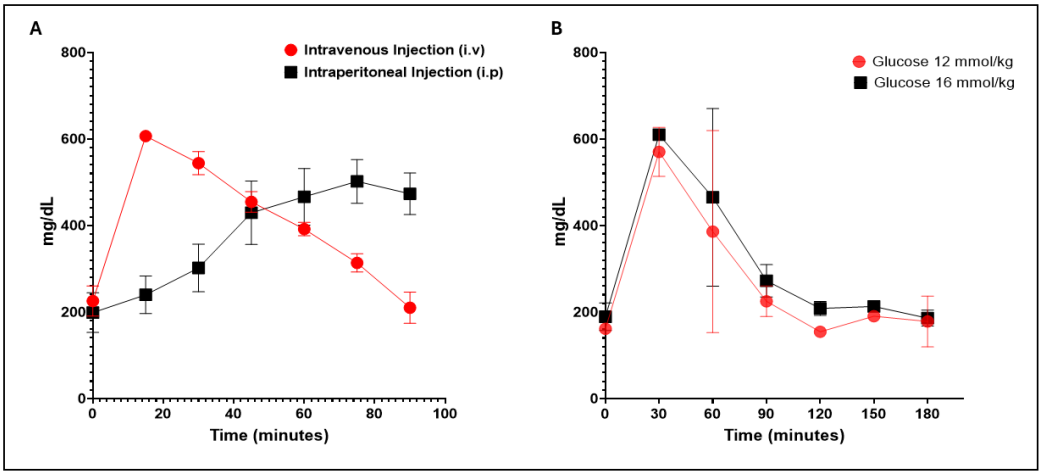

Figure 32: Blood glucose profiles following different glucose administration protocols.(A) This panel compares intravenous (i.v.) and intraperitoneal (i.p.) glucose administration methods. For i.v. injection, a glucose dose of 12 mmol/kg was administered. For i.p. injection, two doses of glucose (4 mmol/kg and 6 mmol/kg) were delivered via two separate injections. (B) This panel illustrates the optimization of glucose concentration via i.v. injection. Two different doses, 12 mmol/kg and 16 mmol/kg, were administered to evaluate the resulting blood glucose levels over time.

- **In-vivo study**

The $AUC_{Lorentz}$ values were analyzed by using half-Lorentzian fitting methos that described the section 3.2.2.3. Examples of representative Z-spectra of healthy animals at the BAT region were obtained from pre-injection to post-injection using i.v. method are shown in Figure 34. Figure 33 shows $AUC_{Lorentz}$ of glucoCEST MRI in two animal groups (n = 12)

receiving glucose via i.v. or i.p. injection. For the i.v. Group glucose was administered at 12 mmol/kg in three separate injections, spaced 30 minutes apart. For the i.p. group: an initial injection with a dose of 4 mmol/kg, followed by a second injection with a dose of 6 mmol/kg after 25 minutes. The MRI measurements for the i.p. group started after the second injection, while for the i.v. group, they began 15 minutes after the first injection. Scans were performed every 30 minutes thereafter.

The glucose uptake increased rapidly from minute 30 to minute 60, peaking at minute 60 ($AUC_{Lorentz}$ = 57.288±31.116), followed by a wash-out of glucose at 90 minutes ($AUC_{Lorentz}$ = 57.288±31.116) in the i.v administration group. In contrast, the glucose uptake slowly increased from minute 30 to minute 60 post-injection and remained steady until 90 minutes ($AUC_{Lorentz}$ = 28.715±16.018 at 30 minutes; $AUC_{Lorentz}$ = 41.364±30.031 at 60 minutes; $AUC_{Lorentz}$ = 48.727±29.138 at 90 minutes) in i.p injection group.

In addition, the Mann-Whitney U-test revealed significant differences in $AUC_{Lorentz}$ between the i.v. and i.p. routes of glucose administration at 60 minutes post-injection ($P < 0.05$). At 30 and 90 minutes, $AUC_{Lorentz}$ did not significantly differ between the two methods ($P > 0.05$). According to the glucose quantitative maps shown in Figure 35, the i.v. administration resulted in a more uniform uptake compared to the i.p. route.

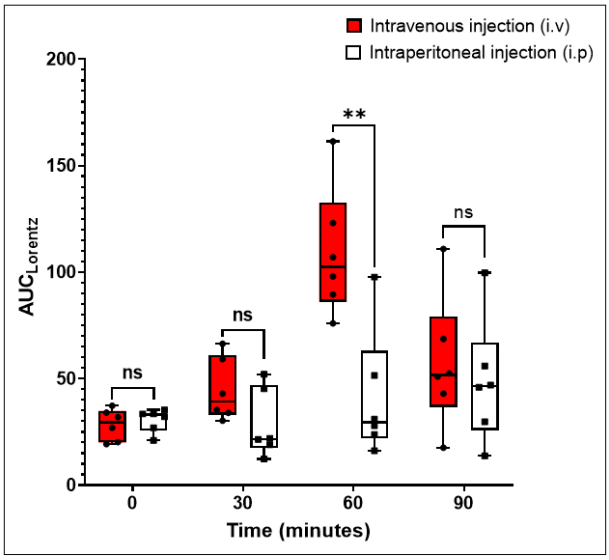

Figure 33: GlucoCEST effects change in $AUC_{Lorentz}$ obtained at 11.7T following glucose administration via two different routes: intravenous (i.v., red box) and intraperitoneal (i.p., white box) with a total of 12 animals . For the i.v. protocol, glucose was administered in three separate injections (12 mmol/kg per injection), and glucoCEST imaging was performed at 30, 60, and 90 minutes following each injection. For the i.p. protocol, an initial

dose of 10 mmol/kg was injected, followed by a second dose of 12 mmol/kg after 25 minutes. Imaging was conducted at 30, 60, and 90 minutes after the second injection.

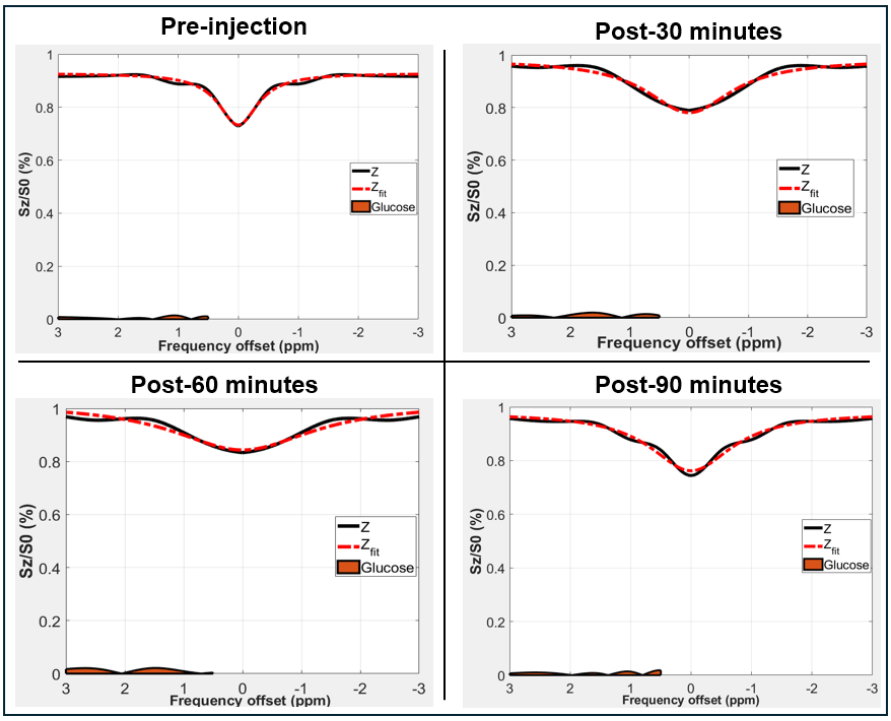

Figure 34: Representative Z-spectrum of healthy animals at the BAT region were obtained from pre-injection to 90 minutes post-injection with i.v. method (n=12). Glucose was administered at a dose of 12 mmol/kg in three separate injections spaced 30 minutes apart.

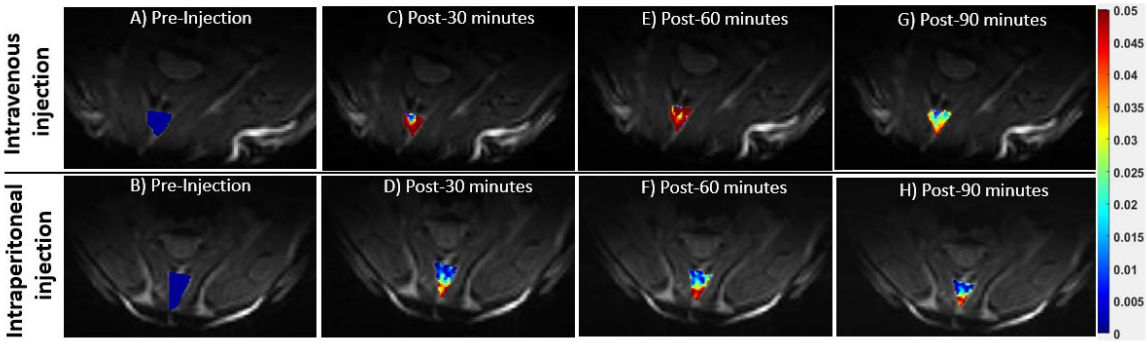

Figure 35: Quantitative maps are overlayed to T_2W anatomical images, and glucoseCEST contrast is shown only in the interscapular BAT region. GlucoCEST effects change in $AUC_{Lorentz}$ obtained at 11.7T upon i.v at doses of 12 mmol/kg glucose with three times injection and i.p glucose administration at doses of 4 and 6 mmol/kg glucose with two times injection (n=12). Data is reported as the $AUC_{Lorentz}$ before and every 30 minutes post-injection.

- **Ex-vivo stimulation study**

NE was used to trigger both α-adrenergic and β_3-adregergic receptors, which are involved in activating BAT thermogenesis in rodents. To investigate whether glucoCEST can detect BAT activation, the measurements were performed on adipose tissue phantoms in three different environments: baseline (PBS), 1.5 M glucose, and 1.5 M glucose combined with NE at a concentration of 10 mM.

For the phantom that contained only fresh adipose tissue with PBS, the glucoseCEST signal which calculated by $AUC_{Lorentz}$ values were 75.2 ± 33.83 for BAT and 44.2 ± 27.01 for WAT, indicating a relatively low signal in the absence of glucose (see Figure 33B).

With the adipose tissue embedded in a phantom filled with a 1.5 M glucose solution, we can observe from the Z-spectrum that $AUC_{Lorentz}$ increased in both tissue types, with BAT showing a higher value (202 ± 236.17) compared to WAT (85.5 ± 57.28), suggesting more significant glucose absorption in BAT.

For the phantom receiving both glucose and NE at a concentration of 10 mM, $AUC_{Lorentz}$ in BAT increased to 327.67 ± 213.84, indicating an enhanced glucose uptake response post-stimulation with NE (see Figure 36). In contrast, WAT showed no change (47.33 ± 27.06), suggesting a limited NE-induced glucose uptake effect in this adipose tissue. These results demonstrate a distinct response of BAT to glucose and NE, supporting its active metabolic role compared to WAT.

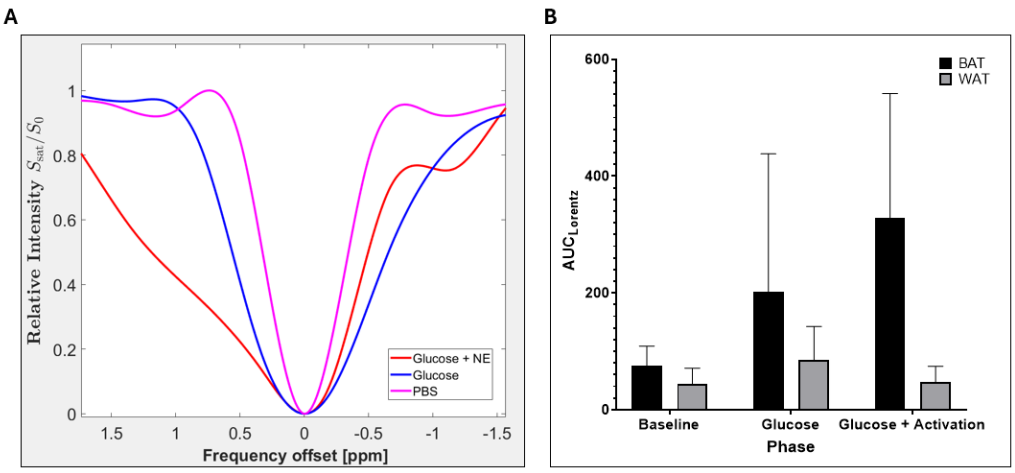

Figure 36: The CEST spectrum (A) and glucose uptake results (B) of BAT were measured under three different phantom conditions: Baseline (PBS), Glucose (1.5 M glucose), and Glucose + NE (1.5 M glucose with NE at concentration 10 mM). Panel A shows that the spectrum of BAT in glucose + NE becomes broader in the range of glucose offset

compared to the baseline and glucose-only conditions. The BAT glucoCEST increased compared to the baseline after pharmacological activation, while WAT glucoseCEST showed no difference before and after the addition of the activation drug. Two samples were used for each group: baseline, glucose phase, and glucose + activation drug.

3.4 Discussion

In this study, we developed the application of CEST MRI to characterize differences between BAT and WAT in mice quantitatively. In addition, we illustrated the ability of CEST imaging to map the adipose tissue based on the water and lipid signal through both ex-vivo and in-vivo experiments.

The results suggest that CEST and glucoCEST metrics may serve as biomarkers for evaluating the metabolic function of adipose tissue. BAT and WAT are distinctly different regarding anatomical structure and physiological functions. In particular, the structure of BAT is rich in iron-rich mitochondria and intracellular water, coupled with a high degree of blood perfusion. This, in turn, contributes to the differences in the CEST effect and glucose uptake of BAT in the tissue compared with WAT. The findings show that Z-spectrum can be a promising tool for distinguishing the BAT and WAT. It offers an opportunity to do non-invasive metabolic research and understand BAT function, particularly in thermogenesis and metabolic disorders.

Conventional imaging techniques, such as MRI mapping ^{1}H MRS, have long been utilized for assessing fat content and differentiating BAT from WAT. However, these methods cannot evaluate the physiological changes in BAT after activation. Although the basic principles of these methods are similar to those of CEST MRI techniques, CEST offers more advantages, including higher sensitivity compared to ^{1}H MRS, which often require longer acquisition time to gain the sufficient spectral solution(Hoefemann, Döring, Fichtner, & Kreis, 2021; Lee & Choi, 2022). In addition, rapid techniques have been developing to accelerate the CEST MRI over the years, which helps to do animal experiments more effectively(Cheema et al., 2025; Heo et al., 2017; Villano et al., 2021; Q. Wu et al., 2024; Y. Zhang, Zu, Liu, & Zhou, 2023). Rapid CEST MRI techniques can also help perform dynamic glucose tests to investigate the vascular kinetics in BAT and compare it with dynamic contrast-enhanced MRI using gadolinium (M. Kim et al., 2022; Yaligar et al., 2020), which can remain in the body and result in multiple conditions, such

as kidney injury, skin problems(Bower, Richter, von Tengg-Kobligk, Heverhagen, & Runge, 2019; Ramalho et al., 2016).

BAT is characterized by a high vascular density, which plays an important role in thermogenesis and metabolism. Moreover, glucose plays an important role in BAT functioning, as it is one of the primary energy sources to support thermogenesis through the oxidation of fat and glucose. Therefore, in addition to distinguishing BAT and WAT based on the difference in the CEST spectrum, the glucoCEST technique also plays an important role in assessing the differences between these two tissues regarding vascular structure and metabolic properties. Because BAT has a dense vascular system and more substantial glucose uptake, the glucose signal of BAT will be higher than that of WAT, providing more detailed information on the microstructure and vascular function of adipose tissue. In addition, when BAT is activated, glucose uptake increases dramatically to meet high energy demands, and this is an important physiological marker distinguishing BAT from WAT. Therefore, as the non-invasive technique for detecting exogenously administered glucose uptake in BAT, glucoCEST can offer implications for BAT's characterization and activity monitoring.

Our findings revealed distinctive glucose uptake patterns in BAT between i.v. and i.p. injections. Specifically, i.v. administration demonstrated rapid uptake and clearance, whereas i.p. injections led to sustained enhancement. This discovery is of particular interest for projects investigating pharmacological BAT activation in metabolic research, as the maximum lifetime of a pharmacologically activated BAT tissue is around 40-60 minutes(Cypess et al., 2015; Whittle, Relat-Pardo, & Vidal-Puig, 2013). Accordingly, it suggests that i.v. injection in the context of glucoCEST quantification in BAT yields more reliable results than i.p. injection, considering that the maximum uptake of glucose occurs at around 60 minutes post administration, leading to a sharp change in the Z-spectrum. In this experiment, WAT's small size and high-fat content in the interscapular region made glucose uptake analysis challenging. As a result, only BAT could be effectively analyzed in this study.

In addition, the ex-vivo study also demonstrated that the glucoCEST technique effectively differentiates BAT from WAT based on differences in glucose uptake, like the in-vivo experiments performed in this study. The vascular perfusion was accompanied by the activation of BAT thermogenesis through adrenergic receptor stimulation. Therefore, the

ex-vivo experiments further revealed that glucoCEST can distinguish BAT from WAT and assess BAT activity before and after stimulation with NE. The increased $AUC_{Lorentz}$ in BAT following NE stimulation indicates enhanced glucose uptake, reflecting its metabolic activation.

Regarding the ex-vivo BAT stimulation study, there are still some technical limitations in preparing the phantom. In embedding fresh tissue into the phantom, we have not yet found an optimal method to fix the tissue's position in the phantom quickly, which can lead to the formation of air bubbles in the phantom, affecting the image quality. It is crucial to keep the tissue fresh, similar to its condition in the mouse body (within two hours), which limits the use of embedding materials such as agarose, as it may alter the tissue's properties. Another consideration in our study is the choice of pharmacological stimulation. As we used NE as the primary activation drug, future studies should compare BAT activation following NE stimulation versus CL 316,243. This selective β3-adrenergic receptor agonist has been used in previous adipose tissue research(Cai et al., 2024). This comparison between these two activation drugs may provide deeper insights into the BAT's functionality and its metabolic consequences. In this ex-vivo phase, the tissue condition is similar to the live tissue in the body. Therefore, using an activation drug, this tissue can reflect a similar thermogenesis ability to the interscapular tissue in the body. Additionally, this phase controls and evaluates the dosage of the activation drug and glucose concentration, providing crucial information before inducing this protocol in future in-vivo studies.

Our study highlights the potential of glucoCEST MRI for non-invasive detection of glucose uptake in BAT. These findings have implications for characterizing BAT activity, especially in projects investigating pharmacological activation in metabolic research. Our findings indicate that i.v. injection is the preferred route for glucose administration, as it provides a more reliable quantification of BAT glucose uptake within the optimal metabolic activation window. This preliminary study represents the first successful demonstration of the glucoCEST technique for detecting exogenously administered glucose uptake kinetics in BAT using MRI. Based on our findings, we recommend the i.v. route of glucose administration.

4. Study 2: Using glucoCEST to evaluate sepsis-induce kidneys injury

4.1 Introduction

4.1.1 Sepsis and Acute kidney injury

Sepsis is a severe condition in which a whole body's immune system excessively responds by releasing proteins and other chemicals to fight infection. Bacterial infections are the common cause of sepsis but can be caused by fungi, parasites, or viruses entering the body. Sepsis can lead to body temperature, heart rate, and respiratory rate alterations associated with the systemic inflammatory response syndrome (SIRS) criteria(Marik & Taeb, 2017). SIRS is the term used to describe physiological changes due to a harmful stressor.

Kidneys are the most common and earliest organs affected by sepsis, resulting in S-AKI. Acute kidney injury (AKI) is the most common and life-threatening complication of sepsis, with a mortality rate of up to 40%, particularly in the elderly. In critically ill patients, sepsis accounts for 45-70% of all cases(Hoste et al., 2018). AKI is a condition defined by a sudden or rapid decrease in the renal filtration function, impairing the kidneys' ability to remove waste and maintain fluid balance in the body. AKI has a unified definition and staging based on the End-stage kidney disease (RIFLE) criteria, including the Risk, Injury, Failure, and Loss of kidney function commenced by the Acute Dialysis Quality Initiative. The RIFLE criteria defined and staged AKI based on the elevated serum creatinine level with or without reduced urine output. Besides that, other classification systems have been used to define the AKI in the last two decades are the Acute Kidney Injury network criteria and kidney disease: Improving Global Outcomes criteria(Xiao et al., 2022).

4.1.2 Pathophysiology of AKI

4.1.2.1 Microvascular dysfunction

The development of AKI causes significant microcirculatory dysfunction which consists of arterioles, capillaries, and venules, marked by increasing heterogeneity in regional blood flow distribution. This condition alters the proportion of capillaries exhibiting different flow patterns, resulting in increased capillaries with continuous flow while those with intermittent or stopped flow. It results in increased leucocyte, platelet rolling, and adhesion with a concomitant reduction in blood flow velocity and microthrombi formation, ultimately disrupting microvascular flow. In addition, it also leads to increasing vascular permeability

and worsening interstitial edema due to endothelial injury, which is associated with an altered barrier function(Chvojka et al., 2008).

4.1.2.2 Inflammation

As in the normal pathway of the body's immune system, it fights against infection, and tubular and endothelial cells, through peritubular circulation, release inflammatory mediators like cytokines and chemokines. This mediator can also be exerted through filtration in the glomerulus, affecting tubular cells in the lumen. The typical cytokines generated and delivered into the circulating blood are tumor necrosis factor α (TNF-α), IL-6, and interleukin-8 (IL-8). They have been recognized as pathogen- and damage-associated molecular patterns, including the families of pathogen-associated molecular patterns (PAMPs) and damage-associated molecular patterns (DAMPs).

Inflammation also stimulates the increasing production of nitric oxide, one of the common elements contributing to mechanisms responsible for S-AKI, like microcirculatory alternations, oxidative stress, and endothelial cell dysfunction. It is activated by the inducible nitric oxide and responds to maintain the normal vascular tone in the kidney. However, excessive nitric oxide expression impairs mitochondrial respiration, resulting in cellular damage(Chvojka et al., 2008).

4.1.2.3 Glucose metabolism in sepsis induced acute kidney injury

Kidneys, considered neurometabolic organs, are essential in maintaining the body's glucose balance via gluconeogenesis, glucose filtration, and glycogenolysis. Gluconeogenesis and glycogenolysis are essential in endogenizing glucose to maintain plasma glucose levels(Wen et al., 2021).

Under normal conditions, the kidneys utilize and metabolize glucose in three ways to maintain glucose homeostasis. First, the kidneys reabsorb glucose into the bloodstream from the glomerular filtration. Second, it releases glucose into the circulation through gluconeogenesis. In this way, gluconeogenesis occurs in the cells of the proximal tubule that is located in cortex. It involves the synthesis of glucose from non-hexose precursors such as glycerol, lactate, pyruvate, and glucogenic amino acids. It consists of 11 enzyme-catalyzed reactions. Lastly, the kidneys take up glucose from circulation to fuel cellular activities and functions(C. Liu et al., 2024). In the endogenous production of glucose in circulation, in addition to the processing of gluconeogenesis, glycogenolysis is also

involved. This is the process in which glycogen is converted to glucose-6-phosphate by glucose-6-phosphatase and its subsequent hydrolysis to free glucose.

During AKI, the kidneys' structure and function are influenced by factors such as renal blood flow, glomerular and peritubular microcirculation, tubular cell function, bioenergetics, and proteome alterations. Proximal tubular epithelial cells in the kidney cortex are the largest group of tubular cells and have high energy demands, primarily met through mitochondrial fatty acid oxidation. Due to their high metabolic activity, they are especially susceptible to hypoxia and other forms of injury(Kruger et al., 2019). Under physiological conditions, due to reduced oxygen supply in proximal tubular cells, they rely on glycolysis instead of fatty acid oxidation (C. Liu et al., 2024). That means the cells must use energy sources other than atty acid oxidation in low oxygen conditions to improve hypoxic conditions(Wen et al., 2021).

4.1.3 Hypothesis and study objectives

Sepsis, a systemic infection caused by circulating bacteria and their toxins, remains a leading cause of mortality worldwide. Among its severe complications, AKI stands out. Studies have reported that sepsis accounts for 20% of global annual deaths, with 40-70% of AKI cases associated with sepsis. Notably, sepsis-related AKI has a mortality rate of approximately 50%(Zarbock et al., 2023). Early diagnosis of AKI is crucial for effective treatment and intervention.

In clinical practice, diagnostic methods primarily rely on parameters such as blood urea nitrogen (BUN) and serum creatinine (SCr)(Faix, 2013). However, these tests often exhibit low sensitivity and specificity(X. Y. Wang et al., 2019). Currently, renal biopsy remains the gold standard for diagnosis, but it is an invasive method and challenging to perform in critically ill patients(Konigsfeld et al., 2019). The diagnosis of AKI poses a significant challenge due to limitations in non-invasive monitoring techniques(Katagiri, Wang, Gore, Harris, & Takahashi, 2021). However, with the advancement of MRI techniques, early detection of AKI has become feasible. Advanced MRI techniques can provide detailed information on both morphology and function(Selby & Francis, 2025). For instance, dynamic contrast-enhanced MRI and arterial spin labeling (ASL) allow the assessment of tissue perfusion and oxygenation levels(W. T. Zhao et al., 2023). DWI is a promising non-invasive method for quantifying renal functional impairment. DWI leverages the random Brownian motion of water molecules to characterize tissue properties, enabling the

description of AKI characteristics(Goyal, Sharma, Bhalla, Gamanagatti, & Seth, 2012). In addition, quantitative renal magnetic resonance relaxometry can provide information on renal structure and function based on the changing of T_1 and T_2 relaxation times of the tissue composition(W. T. Zhao et al., 2023). It is a potential biomarker that can used to evaluate renal perfusion, ischemia/oxygenation, oedema, fibrosis, hydration and comorbidities, which reduce specificity(Buchanan et al., 2021). Although conventional MR techniques offer valuable insights into renal disorders, they are limited in their ability to provide metabolic information.

CEST emerges as a novel molecular MRI technology that addresses this limitation by detecting endogenous metabolites and their microenvironment. Both exogenous and endogenous CEST contrasts have demonstrated efficacy in various renal injury models, including AKI induced by renal ischemia-reperfusion and unilateral ureteral obstruction(Kentrup et al., 2017; J. Liu et al., 2018). Notably, endogenous CEST agents like amides and hydroxyl protons show potential in monitoring the progression of diabetic nephropathy and early AKI(J. Liu et al., 2018; F. Wang et al., 2016; Q. Zhang et al., 2023). Furthermore, recent advances in glucoCEST MRI allow the assessment, diagnosis, and monitoring of inflammatory or cancerous diseases, marking a significant advance in diagnosing complex diseases using non-invasive methods.

In this investigation, our aim was to explore the potential of glucoCEST MRI in diagnosing SI-AKI. We hypothesized that the observed changes in hemodynamics and suppressed cellular metabolism associated with S-AKI would manifest as detectable alterations in glucoCEST MRI signal. Additionally, due to the difference in oxygen supply that decreases from the cortex to the medulla because of the shunting of cortical blood flow, this may create a difference in glucose CEST signals between the cortex and medulla(Y. Chen, Fry, & Layton, 2017). Thus, we sought to introduce glucoCEST MRI as a noninvasive tool for effectively identifying and distinguishing AKI cases.

4.2 Material and methods

The experiment was first evaluated on in vitro phantoms with different types of glucose and concentrations. After the validation step, the experiment continued in vivo. The validation step was conducted to assess the behavior of glucoCEST effects under different conditions, such as B_1 and saturation time. Additionally, this phase helped to identify the optimal sequence and CEST parameters before applying the protocol in the in-vivo stage.

4.2.1 Phase 1: In-vitro validation

4.2.1.1 Chemical and Phantom preparations

D-GLC powder was obtained from WWR Chemical, LLC (Ohio, USA), while 3-OMG powder was sourced from Sigma-Aldrich (Switzerland). For in-vitro studies, solutions of D-GLC and 3-OMG were prepared in 20 mM phosphate-buffered saline(PBS) containing four different concentrations (20, 40, 60, 80 mM). The injectable solutions of D-GLC and 3-OMG for in-vivo experiments were prepared in PBS solvent to obtain a 1.5 M concentration.

4.2.1.2 MRI protocol

The studies were performed on 11.7 T Bruker Biospec system (BioSpin, Bruker Corp., Ettlingen, Germany) using a 72 mm ^{1}H quadrature volume resonator.

We evaluated three different pulse sequences (See Table 4):segmented-FLASH, UTE, and RARE—using a phantom containing four different concentrations (20, 40, 60, and 80 mM) under various B_1 amplitudes (0.5, 1, 1.5, 2, 2.5, 3, 3.5, and 4 μT) and saturation durations ranging from 500 to 3000 ms in 500 ms intervals. Z-spectra were obtained with RF saturation frequencies ranging from -6 ppm to 6 ppm in 5 ppm intervals.

Sequences ⟶ ---------- Parameters ↓	Segmented-FLASH	RARE	UTE
TR (ms)	1061.25	1100	3005.593
TE (ms)	2.906	37.408	0.600
Slice thickness (mm)	1	1	1
Resolution (mm^2)	0.611x0.611	0.611x0.611	0.611x0.611
Segment size	10	/	/
Flip angle (^{0})	15	16	10
RARE factor	/		/
Polar Undersampling	/	/	2
Projections	/	/	142

Table 4: The MRI parameters for invitro validation

4.2.1.3 Data processing

All the CEST spectrum were processed by using In-house MATLAB scripts (MathWorks, Natick, MA, USA).

Quantification by using the Lorentzian fitting method

For the data analysis, regions of interest (ROIs) were manually segmented based on a T_2 weighted image as the first step. For CEST data processing, we use pixel-wised Lorentzian fitting method (See Figure 37) that already described in section 2(section 2.3.3.4.3.2). Additionally, due to the differences in chemical structure, there are variations in the frequency offset between D-GLC and 3-OMG(A. A. Sehgal et al., 2019). As a result, the use of the multi-pool Lorentzian analysis method shows differences in the boundary parameters between the D-GLC and 3-OMG pools, as shown in Table 5. The components/Lorentzian functions were quantified over the ppm range from -6 to 6.

A) Parameters for D-GLC

Parameters	Water	D-GLC
Amplitude (%)	0.9 (0.02 to 1)	1.5 (0.02 to 4)
Line width (ppm)	1.4 (0.3 to 10)	1 (0.5 to 3)
Frequency offset (ppm)	0 (-1 to 1)	1.28 (1 to 2.4)

B) Parameters for 3-OMG

Parameters	Water	3-OMG
Amplitude (%)	0.9 (0.02 to 1)	1.5 (0.02 to 4)
Line width (ppm)	1.4 (0.3 to 10)	1 (0.5 to 3)
Frequency offset (ppm)	0 (-1 to 1)	1.2 (1 to 2.4)

Table 5: The initial values and boundary constraints for the two-pool Lorentzian fitting are defined by three key parameters: frequency offset (ppm), linewidth (ppm), and amplitude (%) for D-GLC and 3-OMG

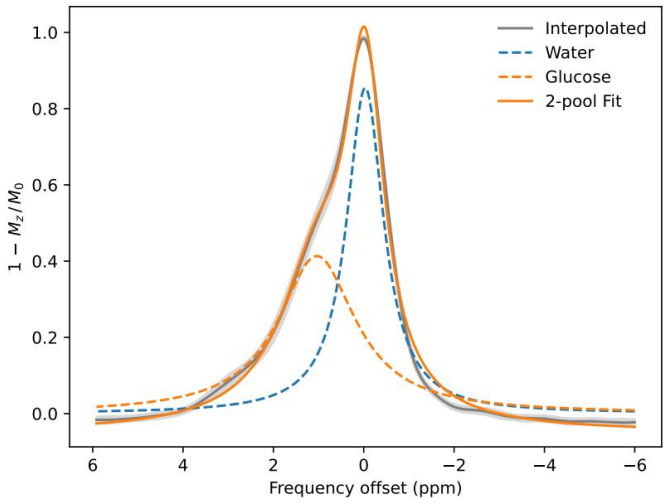

Figure 37: Representative Z-spectrum was analyzed using the two-pool Lorentzian fitting method with D-GLC phantom at a concentration of 60 M dissolved in PBS. The components/Lorentzian functions were quantified over the ppm range from -6 to 6.

4.2.2 Phase 2: In-vivo experiments

4.2.2.1 Animals

All animals' studies followed the National Institute of Health Guidelines for the Care and Use of Laboratory Animals (eighth edition) and the European Community Council Directive for the Care and Use of Laboratory Animals of 22 September 2010 (2010/63/EU). The study protocol was approved by the competent State Office for Food Safety and Consumer Protection (TLLV, Bad Langensalza, Germany; local registration number: 81-02.04.2021.A327). A total of 32 adult male C57BL6/J mice with age ranging from 9 to 12 weeks were included in our study. The animals were housed in a 12-hour light-dark cycle environment, provided with sufficient chow and water.

4.2.2.2 Septic model

Systemic infection was initiated using the PCI disease model(W. T. Zhao et al., 2023). Stool samples were pooled from healthy non-vegetarian donors to optimize bacterial content and deactivate reactive oxygen species. These stool suspensions were meticulously prepared and then stored in aliquots at -80°C until required for experimentation.

For the induction of sepsis, animals were first anesthetized with 2% isoflurane. Subsequently, an aliquot of feces was diluted with saline at a ratio of 1:4 (v/v), and a

precise volume of 5 µL per gram of body weight was intraperitoneally administered into the right lower quadrant of the abdomen using a 21-gauge cannula.

4.2.2.3 Injection protocol

Prior to undergoing MRI scanner, mice underwent the placement of i.v. line in the tail, through which a specific solution of D-GLC or 3-OMG was administered. These solution were prepared at a concentration of 12 mmol/kg

4.2.2.4 Blood test and Immunohistochemical evaluation

- Blood test: Blood glucose levels were measured before and after MRI one hour using a blood test kit. In addition, after the mice were dissected, blood samples were collected and stored at 4 °C for an additional 12 hours to allow for precipitation. The serum was then extracted through blood centrifugation. Several blood indices, including creatinine, urea, and high-density lipoprotein (HDL) were measured using an automatic biochemical analyzer. The measurements have performed by our collaborator “SynLab” from Cologne University hospital, Germany.

- Immunohistochemistry (IHC): The mice kidneys were fixed in phosphate-buffered formaldehyde solution (4%) for 24 h, dehydrated in alcohol. The kidney is cut in half coronally (10 µm), typically along the longest plane. Afterward, a thin layer of OCT compound (Sakura Tissue-Tek O.C.T. Compound, Sigma, 4583) is applied to a disposable mold (Epredia, 18985-1) to help with tissue embedding. Cryosections were stored at -80ºC. IHC has been performed by our collaborator, Dr. Stephan Niland from Institute of Physiological Chemistry and Patho-biochemistry, university of Munster, Germany. The IHC data was analyzed by ImageJ software Fiji (version 1.54p; Fiji Is Just ImageJ, NIH, Maryland, USA)

- **IHC protocol:** Cryosections (10 µm) were retrieved from a -80 °C freezer, brought to room temperature, thawed, and air-dried for 30 minutes. Sections were fixed in cold acetone (-20 °C) for 10 minutes, then dried again for 10 minutes. After outlining with a hydrophobic Dako pen and drying for 10 minutes, slides were washed three times with PBS, carefully replacing solutions to prevent drying. Blocking was performed for 30 minutes at room temperature using 2% horse serum and 0.1% BSA in DPBS (Gibco 14200-083); for hexokinase staining, 100 µg/ml rabbit anti-mouse antibody (Sigma M9537) was added. After washing, sections were incubated overnight at 9 °C with

primary antibodies (1:200 in blocking buffer), followed by PBS washes and incubation with secondary antibodies (1:500) for 1.5 hours at room temperature in the dark. The antibodies were used depending on the target protein: for GLUT1, GLUT2: goat anti rabbit-Alexa Fluor 488 (Invitrogen A11034); for HK2: donkey anti mouse-Alexa Fluor 488 (Invitrogen A21202). After another PBS wash, sections were incubated with WGA-TRITC (1:200, Invitrogen W849) for 2 hours, then stained with 20 µM Hoechst 33342 (Thermo Scientific 62249) in cell culture PBS, 100 µl per section, 5 min at room temperature in the dark. Sections were mounted with Dako Fluoromount, cover-slipped, and placed in a moist chamber in the refrigerator overnight. The next day, slides were sealed with nail polish and imaged using a Zeiss LSM800 confocal microscope with a 10x objective.

4.2.2.5 MRI scan protocol

4.2.2.5.1 Animal Preparation

The animal was placed in a mouse cradle in supine position. During the MRI experiments (See Figure 38), the mice were anesthetized with isoflurane (1-2%). A feedback-controlled warm-water heating system measured Core body temperature with a rectal probe and maintained at 37 ℃. Respiratory gating, utilized to suppress breathing artifacts, involved continuous respiration monitoring. It ensured synchronization of data acquisition with the respiratory cycle by maintaining a rate of 35 ± 5 respiration cycles per minute. This was achieved by controlling the gas flow (air and isoflurane), ensuring accurate synchronization, and minimizing potential distortions in the acquired data.

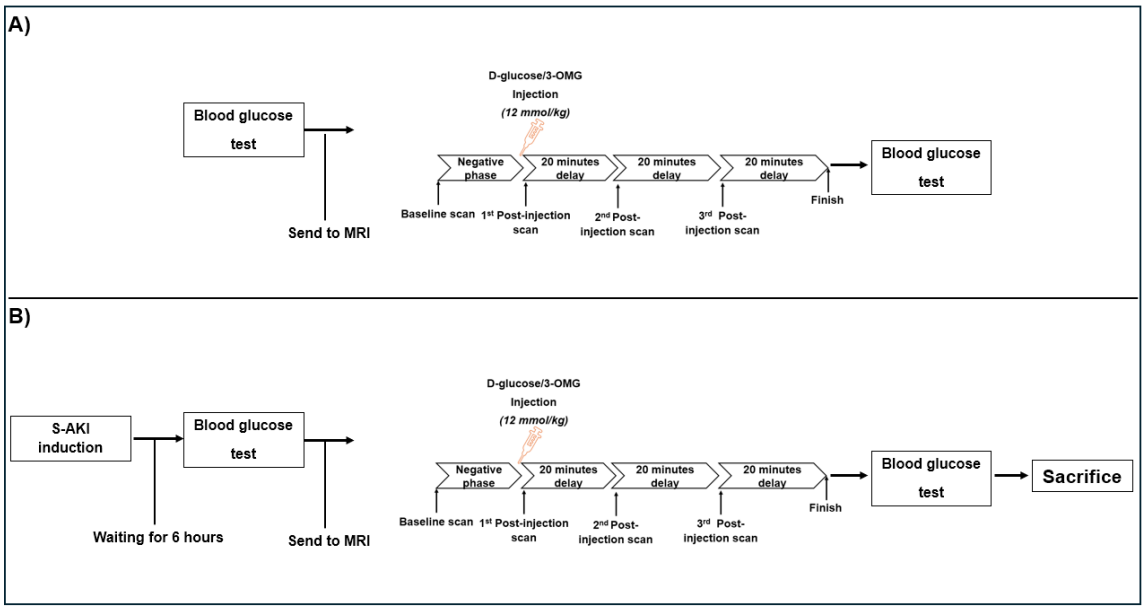

Figure 38: Schematic illustrations of the experimental setting and glucoCEST data acquisition schemes for both (A) control group and (B) sepsis group. Each image series started with a pre-administration baseline image, followed by glucose injection, and post-scanning periods.

4.2.2.5.2 MRI protocols

All experiment were performed on a MRI experiments were performed Bruker Biospec 11.7 T system running ParaVision 7.0.0 (BioSpin, Bruker Corp., Ettlingen, Germany).

For invivo studies, a 72 mm ^{1}H quadrature volume coil and 4-channel surface array coil combination (BioSpin, Bruker Corp., Ettlingen, Germany) was used. The CEST weighted images were acquired by using the optimal parameters of phantom studies with RF saturation power B_1 = 2 µT and pulse duration = 1000 ms. 28 offsets from -20 ppm to 20 ppm were acquired using an interleaved scheme (frequence offsets interval: 0.5 ppm). Additional MR acquisitions were performed to map relaxation times (See Table 6) : For T_1 mapping utilized an inversion recovery RARE sequence with six inversion times (TIs: 300-5500 ms), while T_2 mapping was performed using modified multi-slice multi-echo sequence with 10 echo times (TEs: 6.5-65.01 ms).

Sequences ⟶ / Parameters ↓	**Segmented-FLASH**	**T_1 mapping RARE**	**T_2 mapping Modified multi-slice multi-echo (MSME)**
TR (ms)	1061.25	5500, 3000, 2325, 1650, 975, 300	2500
TE (ms)	2.906	6.65	6.5, 13, 19.5, 26, 32.5, 39, 45.5, 52, 58.5, 65.01
Slice thickness (mm)	1	1	1
Resolution (mm^2)	0.611x0.611	0.611x0.611	0.611x0.611
Segment size	10	/	/
Flip angle (^{0})	15	90	90
Pulse duration (ms)	1000	/	/
Pulse amplitude (µT)	2	/	/
Offset range (ppm)	-6 to 6	/	/
Offset gap (ppm)	0.5	/	/
Number of offsets	28	/	/
RARE factor	/	2	/
T_1 Experiments	/	6	/
Echo Images	/	/	10

Table 6: Scan sequence and parameters that are used in the septic study. These sequences were performed at 11.7T preclinical system.

4.2.2.6 Data processing

4.2.2.6.1 T_1, T_2 mapping

The mapping is analyzed based on the algorithm and software that is described in study 1. Regions of interest (ROIs) were drawn manually in the renal pelvis, medulla and cortex

4.2.2.6.2 GlucoCEST

We used the same method that used for in-vitro data with adding more pools information that describe in Table 7. In addition, the values of other pools like APT, NOE and MTC also were extracted from the multi-pool Lorentzian analysis method (See Figure 39). It can provide more information about changes in mobile proteins and peptides, which reflect the disease-related changes in the kidneys at the molecular and cellular levels(J. Liu et al., 2018). $AUC_{Lorentz}$ (calculated over the complete Lorentzian function range from -6 to 6 ppm). Regarding the CEST@2 ppm that correlate to the creatine concentration(K. Cai et al., 2015), we referred the fitting parameters for creatine-CEST (Cr-CEST) from (Z. Cai et al., 2024): Frequency offset (ppm): 3.5 (3.0 to 4.0); Line width (ppm): 0.5 (0.1 to 5); and amplitude (%): 2 (0.01 to 20).

A) Parameters for D-glucose

Parameters	Water	Amide	NOE	MT	D-glucose
Amplitude (%)	0.9 (0.02 to 1)	0.025 (0 to 0.2)	0.02 (0 to 0.4)	0.1 (0 to 1)	1.5 (0.02 to 4)
Line width (ppm)	1.4 (0.3 to 10)	0.5 (0.4 to3)	3 (1 to 5)	25 (10 to 100)	1 (0.5 to 3)
Frequency offset (ppm)	0 (-1 to 1)	3.5 (3.5 to 3.5)	-3.5 (-3.5 to -3.5)	-1.5 (-3 to -1)	1.28 (1 to 2.4)

B) Parameters for 3OMG

Parameters	Water	Amide	NOE	MT	3OMG
Amplitude (%)	0.9 (0.02 to 1)	0.025 (0 to 0.2)	0.02 (0 to 0.4)	0.1 (0 to 1)	1.5 (0.02 to 4)
Line width (ppm)	1.4 (0.3 to 10)	0.5 (0.4 to3)	3 (1 to 5)	25 (10 to 100)	1 (0.5 to 3)
Frequency offset (ppm)	0 (-1 to 1)	3.5 (3.5 to 3.5)	-3.5 (-3.5 to -3.5)	-1.5 (-3 to -1)	1.2 (1 to 2.4)

Table 7: The initial values and boundary conditions for the five-pool Lorentzian fitting are defined by three key parameters: frequency offset (ppm), linewidth (ppm), and amplitude (%) for D-GLC and 3-OMG

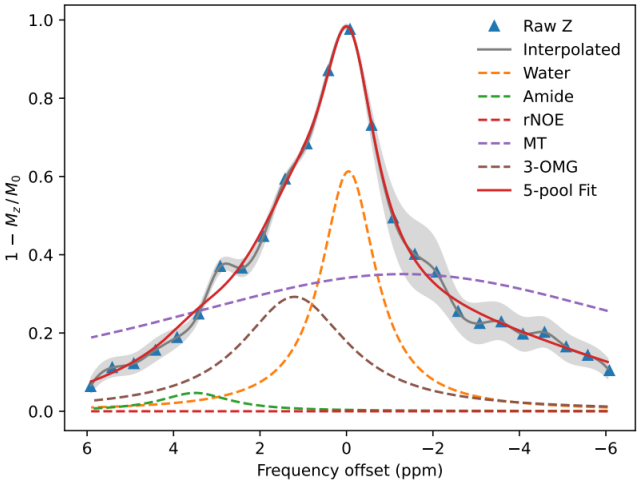

Figure 39: Representative glucoCEST Z-spectra of healthy animals in the pelvis region were obtained from pre-injection (D-GLC) to 40 minutes post-injection using the seg-FLASH sequence (with 2 μT and 1000 ms). These Z-spectra were analyzed using five-pool Lorentzian fitting with a pixel-wise method. The components/Lorentzian functions were quantified over the ppm range from -6 to 6.

4.2.2.6.3 Amide Concentration Independent Detection (AACID)

AACID is an index used to quantify image contrast that can reflect tissue intracellular pH. It is calculated as the ratio of the CEST effect at 2.0 ppm (assigned to the amine proton offset) and 3.5 ppm (assigned to the amide proton offset), normalized by the CEST effect at 5.6 ppm. The equation used for this calculation, as referenced from (Albatany, Meakin, & Bartha, 2022):

$$\mathrm{AACID}_{2.0} = \frac{M_{Z3.5\,\mathrm{ppm}} \times \left(M_{Z5.6\,\mathrm{ppm}} - M_{Z2.0\,\mathrm{ppm}}\right)}{M_{Z2.0\,\mathrm{ppm}} \times \left(M_{Z5.6\,\mathrm{ppm}} - M_{Z3.5\,\mathrm{ppm}}\right)}$$

The ratio of amine and amide proton offset is normalized by the CEST effect at 5.6 ppm. The normalized values in this equation were adjusted based on the offsets in our experiment, as we set the frequency offset range from -6 to 6 ppm. Due to the resonance frequency shifting (B_0 correction), we could not apply the normalized value at 6 ppm according to the original equation.

4.2.2.7 Statistical Test

All statistical analyses were performed using GraphPad Prism (version 9; GraphPad Software, Boston, MA, USA). Mann–Whitney U test was used to test the significance of the difference between the parameters of the control and septic groups. Pearson correlation test was used to evaluate the correlation relationship between imaging parameters and blood biochemical markers. $P < 0.05$ was considered statistically significant.

4.3 Results

4.3.1 Phase 1: In-vitro validation

Phantoms with varying glucose concentrations dissolved in PBS were tested to evaluate the effects of saturation power, saturation duration, and glucose concentration on glucoCEST signal. These phantoms were measured using different MRI pulse sequences: Segmented-FLASH, CEST UTE, and CEST RARE to compare glucoCEST signal differences across acquisition methods. The validation was to identify the optimal sequence, as well as parameters such as B_1 and saturation time, to enhance the glucoCEST signal effectively and make it suitable for in vivo experiments. The glucoCEST effect was analyzed using the two-pool Lorentzian fitting with pixel-wise method (Section 4.2.1.3), and the Z-spectra are shown in Figure 42.

Figure 40A shows data for a 60 mM D-GLC phantom with a saturation duration of 1000 ms, demonstrating the relationship between B_1 amplitude and $AUC_{Lorentz}$. As B_1 amplitude increases, $AUC_{Lorentz}$ rises, with CEST UTE and CEST Seg-FLASH sequences showing more pronounced increases compared to CEST RARE. At low B_1 (below 2 μT), $AUC_{Lorentz}$ is similar across all sequences, but above 2 μT, the difference becomes more apparent. CEST Seg-FLASH shows the highest $AUC_{Lorentz}$ at higher B1 amplitudes, while CEST RARE shows a slower increase, indicating lower sensitivity to B1 changes. When B1 exceeds 3 μT, $AUC_{Lorentz}$ decreases for all sequences, with CEST Seg-FLASH decreasing at 3 μT and CEST UTE and RARE decreasing at 3.5 μT. Additionally, the effect of varying saturation duration on the CEST effect was evaluated at B_1 = 2 μT. $AUC_{Lorentz}$ increases from 500 ms to 1000 ms, then plateaus for longer saturation durations. CEST Seg-FLASH and CEST UTE show a stronger effect, while CEST RARE exhibits a lower CEST effect, consistent with the trends observed across other sequences.

Figure 40B presents similar trends for a 60 mM 3-OMG phantom at saturation duration 1000 ms and B_1 amplitudes from 1 μT to 4 μT. As with D-GLC, CEST UTE and CEST

RARE show increased CEST effects at higher B1 values over 3 µT, while CEST FLASH reaches a plateau at 3.5 µT and 4.0 µT. CEST UTE and Seg-FLASH produce stronger effects than CEST RARE.

Finally, Figure 40B also shows that, for the 60 mM 3-OMG phantom at B_1 = 2 µT, the CEST effect increases with saturation time from 500 ms to 1000 ms and plateaus for longer durations. CEST RARE shows a lower effect compared to CEST UTE and Seg-FLASH.

This validation indicates that CEST seg-FLASH and CEST UTE sequences are more responsive to parameter changes than CEST RARE, particularly at higher B_1 power levels and longer saturation durations. Furthermore, the results suggest that a saturation time of 1000 ms, along with B_1 = 2µT(Anemone et al., 2021), based on parameters from the previous study, could be the optimal values for applying in vivo experiments.

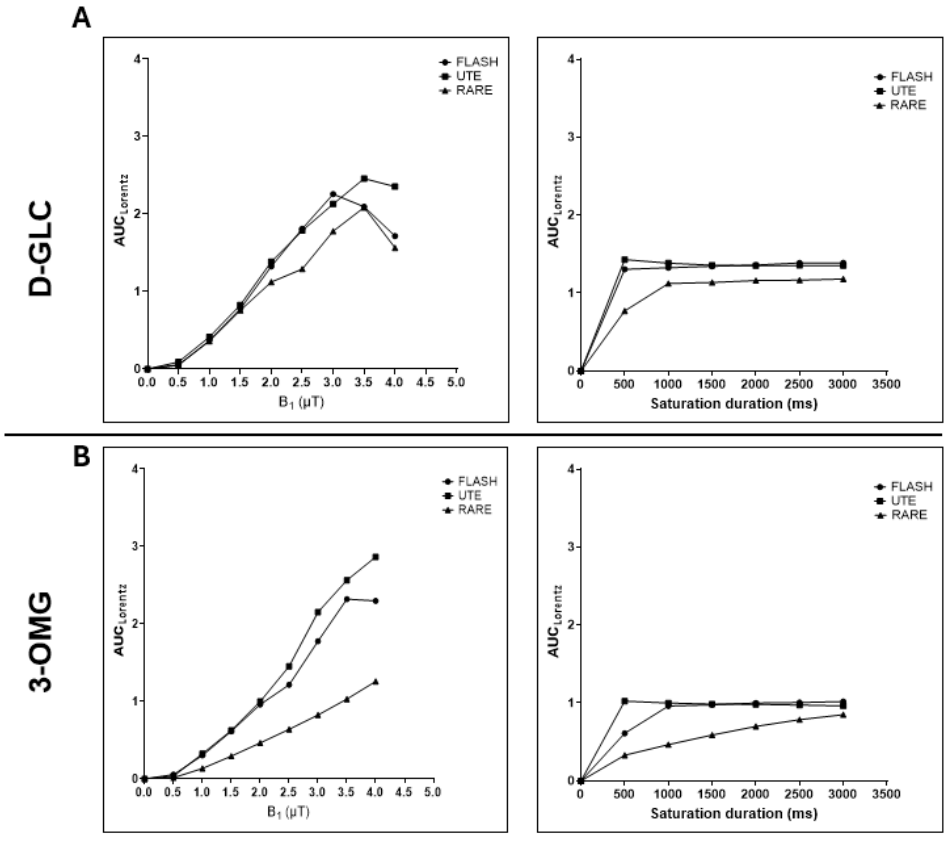

Figure 40: Characterization of glucoCEST at different B_1 power, concentration and saturation time. (A) GlucoCEST dependence on B_1 at the saturation duration of 1s and saturation time from a 60 mM D-GLC phantom at the B_1 power of 2 µT (calculated over the complete Lorentzian function range from -6 to 6 ppm), (B) GlucoCEST dependence on B_1 at the saturation duration of 1s and saturation time from a 60 mM 3-OMG phantom

at the B_1 power of 2 µT (calculated over the complete Lorentzian function range from -6 to 6 ppm)

To assess the glucose concentration-dependent properties of D-GLC and 3-OMG, phantoms with varying glucose concentrations were tested (Figure 41). Figure 41A shows a linear relationship between D-GLC concentrations (20 to 80 mM) and AUCLorentz values at a B_1 = 2 µT and t_{sat} = 1000 ms. The data demonstrates proportionality up to 80 mM, with a linear regression (R^2 = 0.9843) yielding the equation Y = 0.02112*X + 0.08562, where Y is the glucoCEST contrast and X is glucose concentration in mM. This indicates that the glucoCEST signal increases with glucose concentration, confirming its ability to quantify glucose effectively within this range.

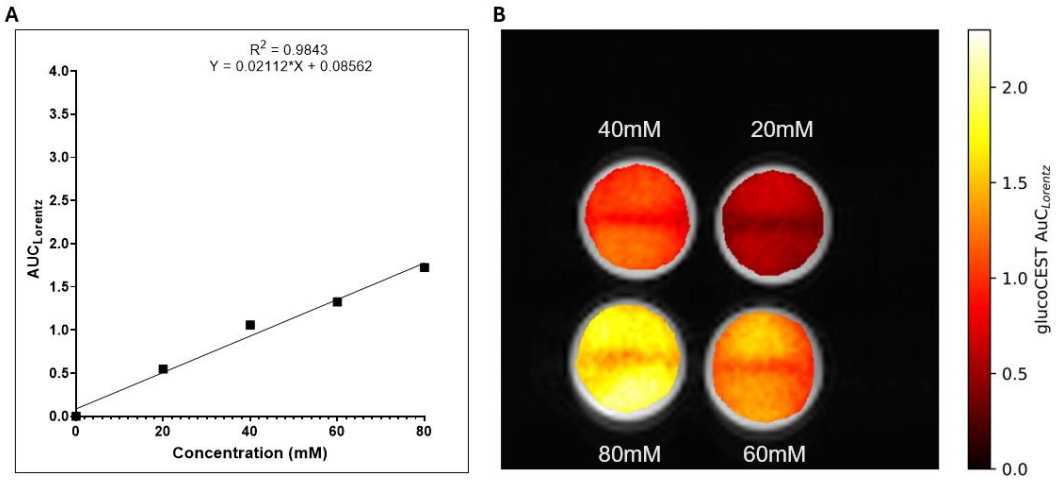

Figure 41: Characterization of glucoCEST at different concentrations (using 4 phantoms with glucose concentrations ranging from 20 to 80 mM, prepared with PBS). (A) The glucoCEST contrast demonstrates a linear relationship with different glucose concentrations, remaining proportional up to a concentration of 80 mM, as reflected by the corresponding $AUC_{Lorentz}$ contrast values, with B_1 = 2.0 µT and pulse duration = 1000 ms, (B) glucoCEST contrast at 20, 40, 60, and 80 mM , with B_1 = 2.0 µT and pulse duration = 1000 ms,

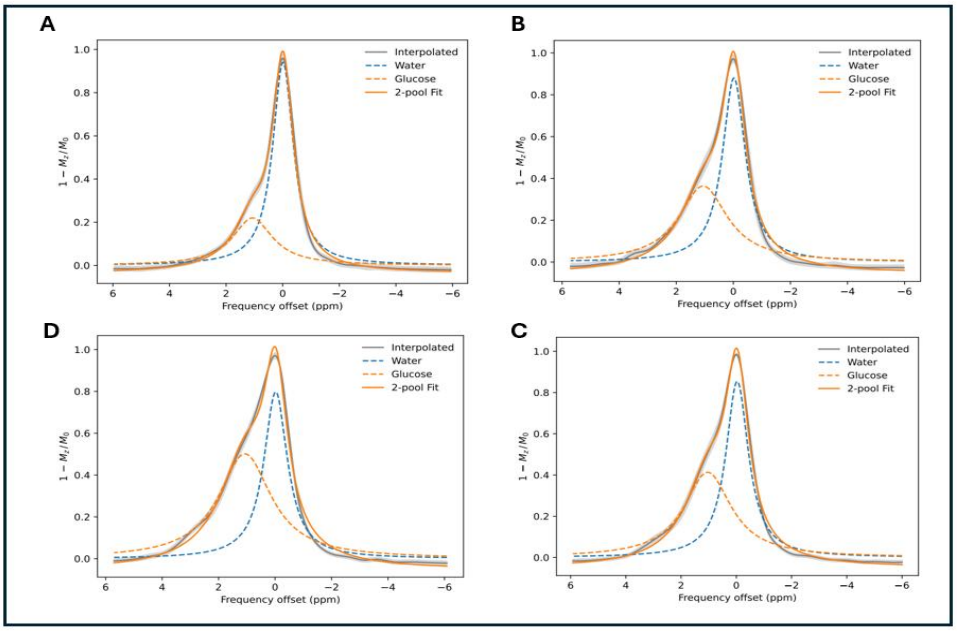

Figure 42: Z-spectrum of D-GLC invitro phantom at different concentrations (four phantom, acquired using 2 μT and 1000 ms). A, the D-GLC phantom at 20 mM concentration. B, the D-GLC phantom at 40 mM concentration. C, the D-GLC phantom at 60 mM concentration. D, the D-GLC phantom at 80 mM concentration.

4.3.2. Phase 2: In-vivo experiments

4.3.2.1 MR assessment of S-AKI

We assessed multiple MRI parameters such as T_1, T_2, and CEST to understand the variations in MRI signals in S-AKI kidneys.

4.3.2.1.1 MR relaxometry of AKI

The T_1 and T_2 mapping techniques were implemented to evaluate changes in molecular water exchange within and outside the cells during the early stages of S-AKI, which involve inflammatory cell infiltration, renal tubular collapse, cellular swelling, and interstitial edema. In addition, T_2 mapping was measured before and after the injection of D-GLC and 3-OMG to assess whether glucose had any effect on the T_2 mapping characteristics of the tissue. As demonstrated in Figure 43 and 44, there was no notable difference in the T_1 and T_2 relaxation times between the injured and healthy kidneys.

- **D-GLC injection group:** Figure 43A shows that the T_2 values in the septic group tended to decrease compared to the control group in all three regions: pelvis (49.211 ± 5.029 vs 63.879 ± 5.642, $P < 0.05$), medulla (27.892 ± 5.737 vs 40.217 ± 4.970, $P < 0.05$), and cortex (25.329 ± 3.259 vs 31.185 ± 2.825, $P < 0.05$) in the pre-injection

phase. This significant difference suggests a septic condition because of poor perfusion and increased water viscosity. This difference is most prominent in the pelvis region. In addition, T_2 values at 60 minutes after glucose injection in the control group tended to decrease compared to the pre-glucose injection time in all three regions: pelvis (53.736 ± 1.836 vs 63.879 ± 5.642, *P <0.05*), medulla (37.439 ± 6.518 vs 40.217 ± 4.970, *P* > 0.05), and cortex(32.816 ± 2.421 vs 31.185 ± 2.825, *P* > 0.05). In the septic group, the T_2 values were almost unchanged before and after glucose injection in all three regions: pelvis (49.211 ± 5.029 vs 48.813 ± 5.641), medulla (27.892 ± 5.737 vs 29.006 ± 4.342), and cortex (25.329 ± 3.259 vs 26.934 ± 3.565). This result suggests that glucose may affect the properties of urine, increasing urine viscosity. In the septic group, there was almost no difference in the T_2 values before and after glucose injection due to reduced blood flow.

- **3-OMG injection group:** Figure 43B show the difference in T_2 values between the control and septic groups before glucose injection in the D-GLC group was also found in the 3-OMG group. In the control group, the T_2 values did not change significantly between the pre-and post-injection times in the three regions: pelvis (64.420 ± 9.902 vs 56.172 ± 8.109, ns), medulla (42.967 ± 3.552 vs 38.278 ± 3.427, ns), and cortex (33.614 ± 0.958 vs 34.416 ± 3.431, ns), although the T_2 values tended to decrease after injection. This suggests that 3-OMG does not affect the nature of water and urine like D-GLC . This change was similar in the septic group (50.399 ± 5.723 vs 46.181 ± 4.412, ns), medulla (34.240 ± 5.302 vs 32.105 ± 5.965, ns), and cortex (25.738 ± 3.151 vs 25.152 ± 5.031, ns).

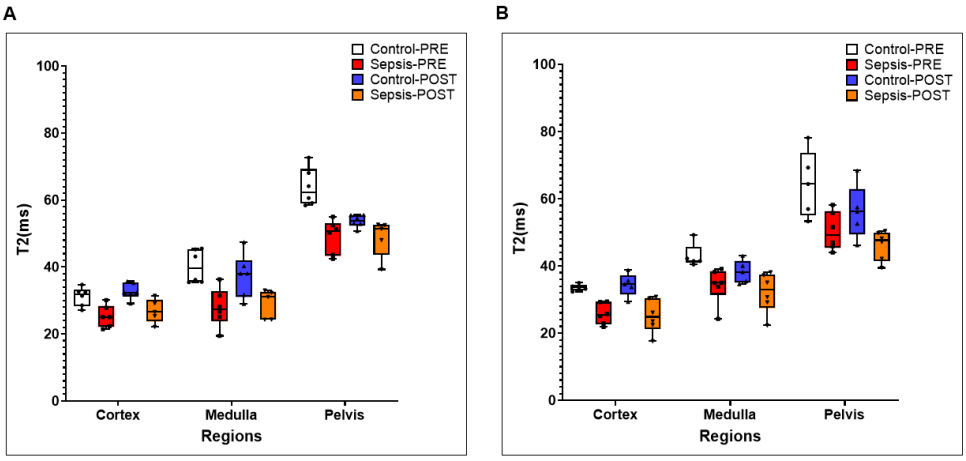

Figure 43: This graph demonstrates the changes in T_2 values at pre-injection and post-injection time points for two glucose contrast agents (D-GLC and 3-OMG), compared in

the control and septic groups. Panel A shows the T_2 values measured in the control and septic groups for D-GLC (n = 6 per group), comparing the pre-injection and post-injection T_2 values. Panel B shows the T2 values measured for 3-OMG, with the same comparison between pre- and post-injection within the control and septic groups (n = 6 per group). Error bars indicate standard deviation (SD).

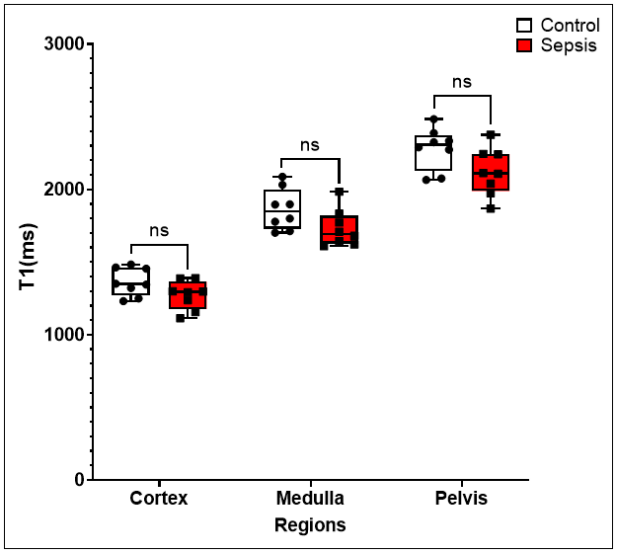

Figure 44: This graph demonstrates the T_1 value changes at pre-injection compared in the control (n = 8) and septic groups (n = 8) in the pelvis, medulla and cortex regions. Error bars indicate SD. Statistical significance is denoted as follows: *P < 0.05, **P < 0.01, ***P < 0.001, and n.s. (not significant).

4.3.2.1.2 Change in APT, NOE and MTC in disease and healthy groups

To investigate the changes in MRI signals in S-AKI beside the glucoCEST index, we analyzed additional four CEST MRI metric: APT, NOE, MTC, and CEST-effect at 2 ppm (including creatine metabolite). These effects were quantified based on the CEST-MRI signal using five-pool Lorentzian fitting with pixel wise analysis method that described in section 4.2.2.6.2 (See Figure 39). The index was analyzed in the medulla and cortex of the kidneys at baseline.

- **APT and NOE**

Figure 45A presents the APT values in the medulla and cortex during the pre-injection phase, including both the control group (n = 16) and the sepsis group (n = 16). No significant differences were observed between septic and control animals in the medulla or cortex. While a slight decrease in APT values was seen in the septic group, this effect was more pronounced in the cortex compared to the medulla, where the values were

slightly lower in the cortex. This result suggests that sepsis did not significantly alter APT-based metabolic exchange processes.

Figure 45B illustrates NOE values in the medulla and cortex of the kidney at pre-injection phase. The same APT trend was found for the NOE in the medulla region. In the cortex region, the NOE value was slightly higher in the septic group compared to the control. In general, the NOE did not show significant differences between septic and control animals in the medulla and cortex regions. Although minor fluctuations were noted, these variations were not statistically significant, indicating that NOE contrast remains stable regardless of sepsis-induced metabolic changes.

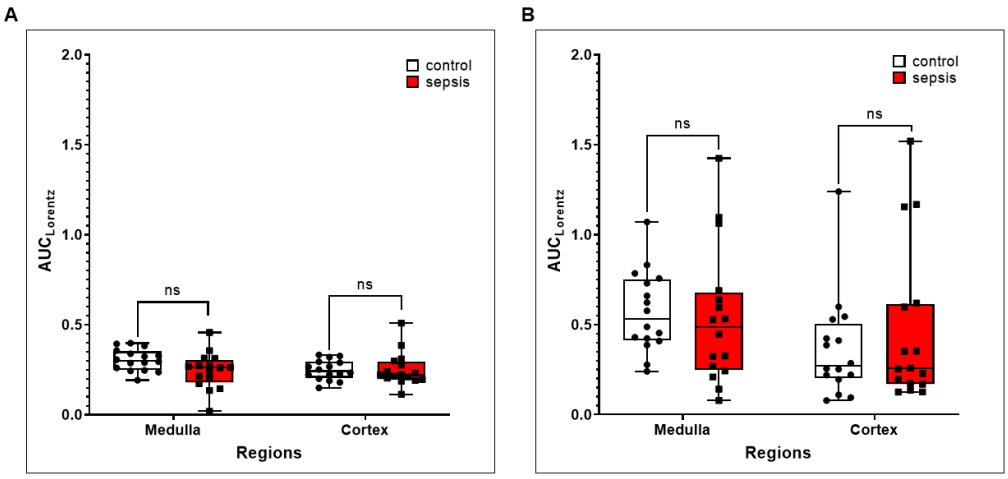

Figure 45: This graph shows the changes in APT and NOE values at pre-injection in the control (n = 16) and septic (n = 16) groups across the medulla and cortex regions: (A) APT; (B) NOE. Error bars represent SD. Statistical significance is denoted as follows: *P < 0.05, **P < 0.01, ***P < 0.001, and n.s.

- **MTC and Cr-CEST**

MTC: The MTC signal variations are shown in Figure 46A, depicting magnetization transfer contrast across kidney regions. No significant differences were observed between septic and control groups across medulla and cortex regions. This suggests that MTC contrast, which reflects macromolecular interactions, is not significantly impacted by sepsis in this disease model.

CEST contrast at frequency offset 2 ppm (including Cr-CEST): Cr-CEST metric was used to evaluate changes in creatine by comparing the control and septic groups. Figure 46B shows the $AUC_{Lorentz}$ values in the medulla and cortex. In the septic group, the creatine

$AUC_{Lorentz}$ values were slightly reduced in (0.751 ± 0.243 vs 0.587 ± 0.370) and cortex(0.368 ± 0.193 vs 0.294 ± 0.245) compared to the control group. This difference was insignificant, suggesting that in the septic model for 6-hours, there was no substantial change in creatine kinase metabolites.

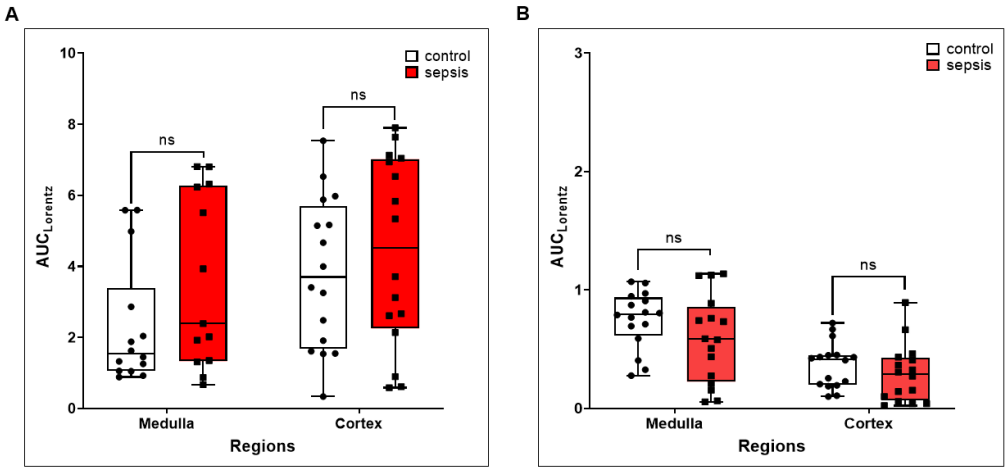

Figure 46: This graph shows the changes in MTC and Cr-CEST values at pre-injection in the control (n = 16) and septic (n = 16) groups in the medulla and cortex regions: (A) MTC; (B) Cr-CEST. Error bars represent SD. Statistical significance is denoted as follows: **P* < 0.05, ***P* < 0.01, ****P* < 0.001, and n.s.

4.3.2.1.3 Change in AACID value in disease and healthy groups

The AACID value was calculated based on pH sensitivity using the equation from section 4.2.2.6.3. This value was measured in the pelvis, medulla, and cortex before and after glucose injection in the D-GLC (control n = 8, sepsis n = 8) and 3-OMG (control n = 8, sepsis n = 8) groups. The goal was to evaluate pH differences between the control and sepsis groups and assess any changes in pH after glucose injection.

- **D-GLC injection group:** Figure 47A shows that in the septic group, AACID values were slightly higher than the control group across all regions (pelvis: 2.099 ± 0.395 vs 2.127 ± 0.254, *P* > 0.05; medulla: 2.150 ± 0.323 vs 2.063 ± 0.265, *P* > 0.05; cortex: 1.928 ± 0.214 vs 1.985 ± 0.117, *P* > 0.05) at pre-injection, indicating no significant pH change despite a decreasing trend. Post-injection, AACID values remained unchanged in the septic group. In contrast, the control group showed significant increases in the pelvis (post-20: 3.208 ± 0.433 vs 2.299 ± 0.627, *P* < 0.05; post-60: 3.129 ± 0.853 vs 1.964 ± 0.397, *P* < 0.05). The medulla and cortex showed no significant changes. These results suggest that glucose induces pH changes, especially in the pelvis, where

glucose concentration is higher. In the septic group, pH changes were minimal due to reduced blood flow.

- **3-OMG injection group:** Figure 47B shows that in the septic group, AACID values were higher than in the control group at pre-injection (pelvis: 2.467 ± 0.517 vs 1.970 ± 0.148, $P < 0.05$; medulla: 2.419 ± 0.428 vs 2.008 ± 0.093, $P > 0.05$; cortex: 2.225 ± 0.367 vs 1.956 ± 0.100, $P > 0.05$). This trend was similar to D-GLC but was statistically significant in the 3-OMG group, possibly due to variability in the animals' condition. Post-injection, the control group showed increased AACID values, especially in the pelvis, while no significant change was observed in the septic group. Like D-GLC, 3-OMG induced pH changes in the pelvis, suggesting it also affects the urine pH environment.

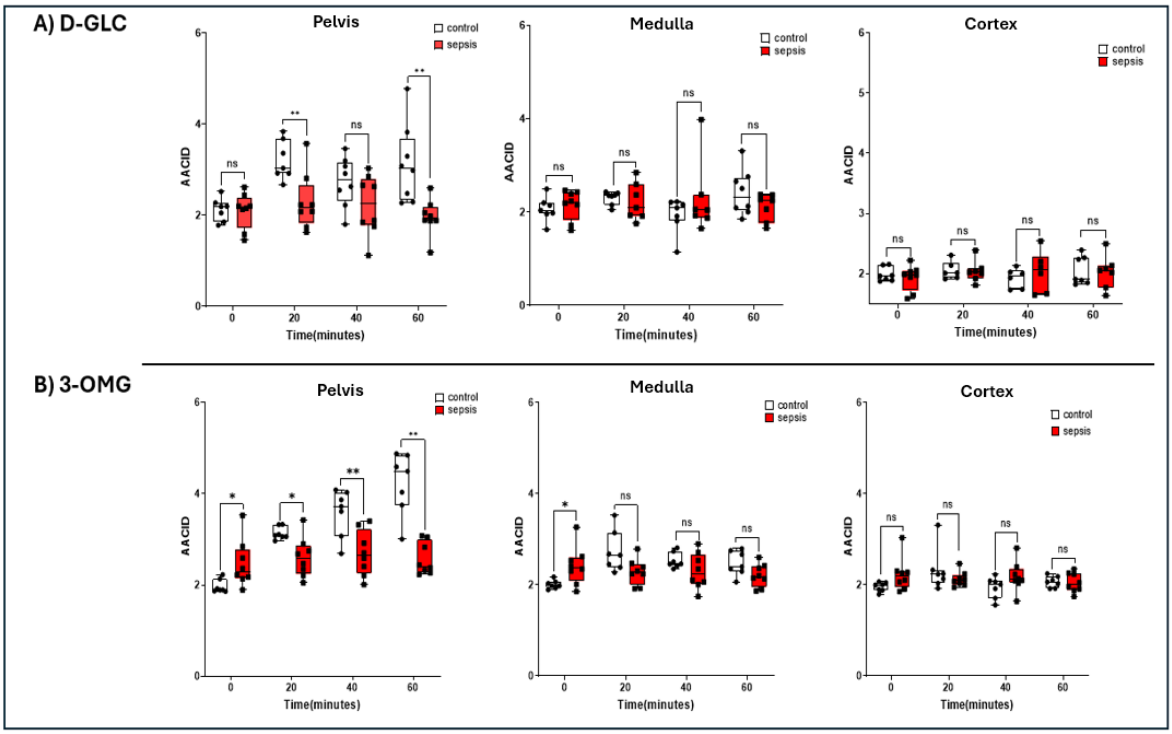

Figure 47: This graph shows the changes in AACID values at pre- and post-injection (using D-GLC and 3-OMG) in the control (n = 8) and septic (n = 8) groups for each substance across the pelvis, medulla and cortex regions: (A) D-GLC groups; (B) 3-OMG groups. Error bars indicate SD. Statistical significance is denoted as follows: *$P < 0.05$, **$P < 0.01$, ***$P < 0.001$, and n.s.

4.3.2.1.4 GlucoCEST signal of D-GLC, Methyl in Sepsis-AKI

- **D-GLC group results:**

Figures 49 and 50 show representative Z-spectra and color maps from a control and septic animal, comparing pre- and post-glucose injection. GlucoCEST was used to quantify glucose uptake and metabolism across three kidney regions (pelvis, medulla, cortex) at four time points: pre-injection, and 20-, 40-, and 60-minutes post-injection, with glucose administered at 12 mmol/kg. This approach helps better understand the kinetics of glucose in the tissue in healthy and septic conditions, providing a comprehensive profile of glucose metabolism. The $AUC_{Lorentz}$ values were analyzed using a five-pool Lorentzian fitting method (Section 4.2.2.6.2).

Baseline: No significant differences were found between the septic and control groups in all regions (Figure 48). The control group showed slightly higher $AUC_{Lorentz}$ values in the pelvis (0.547 ± 0.070 vs. 0.419 ± 0.168), medulla (0.367 ± 0.107 vs. 0.258 ± 0.178), and cortex (0.204 ± 0.085 vs. 0.175 ± 0.106), but the differences were not statistically significant.

Post-injection 20 minutes: In the control group, a significant increase in glucose signal was observed, particularly in the pelvis and medulla (Figure 48). The septic group showed a lower response. In the pelvis, the $AUC_{Lorentz}$ in the control group increased to 1.580 ± 0.291, while in the sepsis group, it remained low at 0.526 ± 0.327 ($P < 0.001$). A similar trend was observed in the medulla (1.001 ± 0.295 vs. 0.357 ± 0.259, $P < 0.05$), and the cortex showed a slight but significant increase in the control group (0.320 ± 0.128 vs. 0.152 ± 0.074, $P < 0.05$).

Post-injection 40 minutes: The control group maintained a high glucose signal across all regions, while the septic group showed persistently low signals (Figure 48). In the pelvis, the control group remained significantly elevated (1.243 ± 0.499 vs. 0.378 ± 0.176, $P < 0.001$), while no significant difference was found in the medulla (0.505 ± 0.224 vs. 0.304 ± 0.185, $P > 0.05$) and cortex (0.221 ± 0.117 vs. 0.208 ± 0.132, $P > 0.05$).

Post-injection 60 minutes: The $AUC_{Lorentz}$ in the control group gradually declined but remained higher than in the septic group (Figure 48). In the pelvis, the control group's AUCLorentz was 1.201 ± 0.482, significantly higher than the septic group (0.367 ± 0.224, $P < 0.001$). In the medulla, the control group showed a significant reduction (0.515 ± 0.143 vs. 0.283 ± 0.226, $P < 0.05$). No significant difference was observed in the cortex (0.226 ± 0.106 vs. 0.149 ± 0.124, ns).

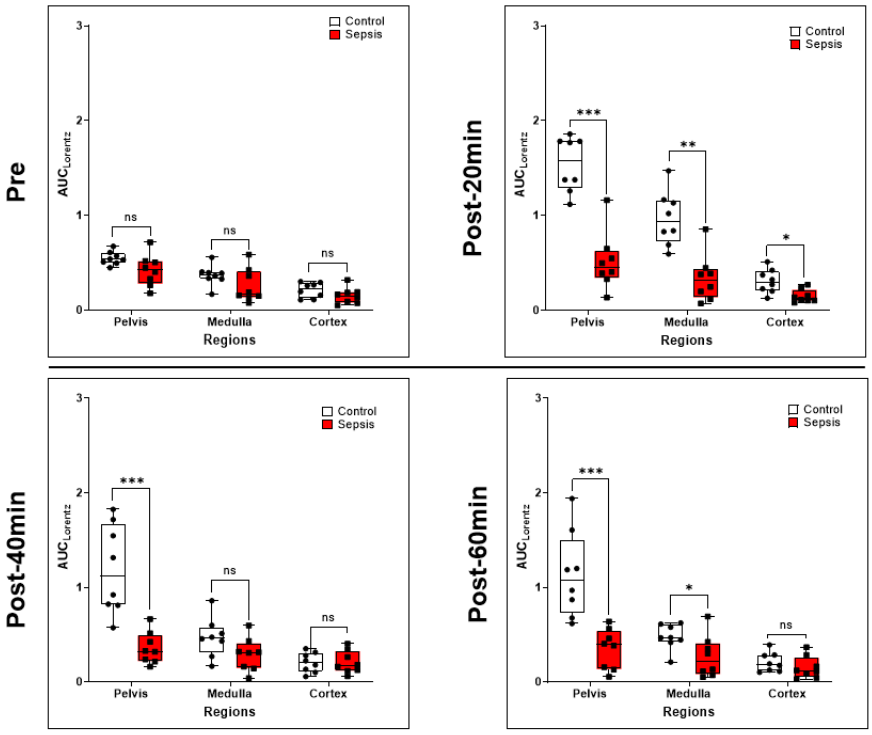

Figure 48: This graph shows the changes in glucoCEST signal at pre- and post-injection using D-GLC glucose as a contrast agent (12 mmol/kg, i.v.) between the control (n = 8) and septic (n = 8) groups across the pelvis, medulla, and cortex regions. Error bars represent SD. *P < 0.05; **P < 0.01; ***P < 0.001; n.s.

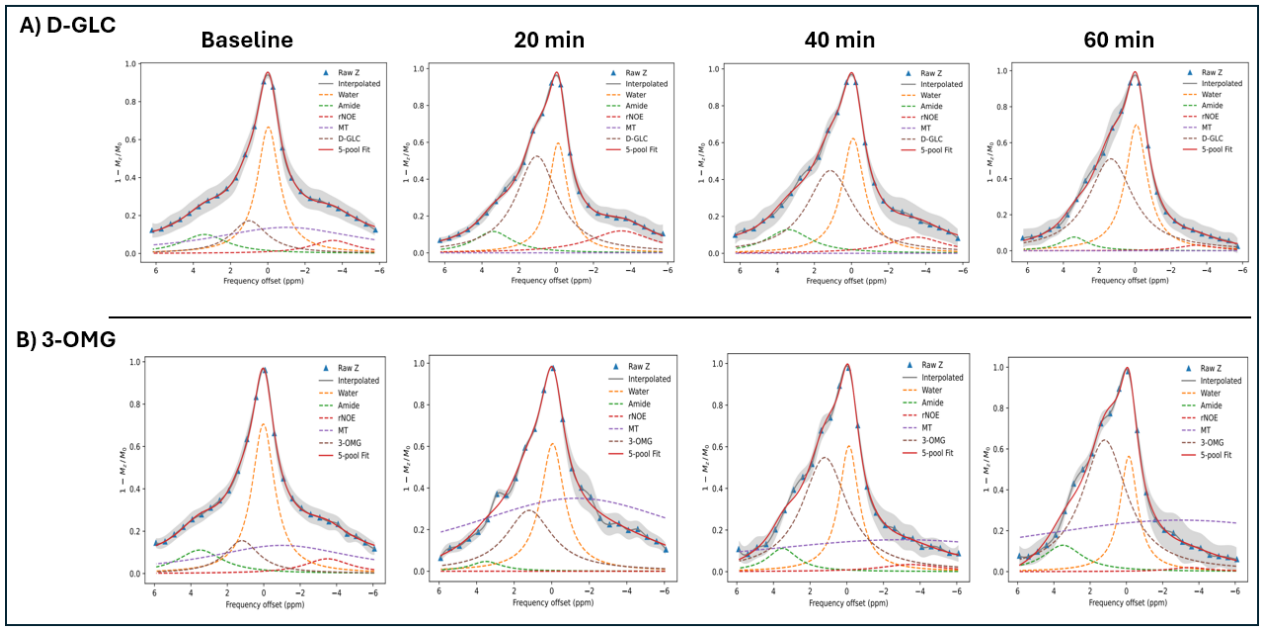

Figure 49: Representative glucoCEST Z-spectra of healthy animals in the pelvis region were obtained from pre-injection to 60 minutes post-injection using the seg-FLASH sequence (with 2 μT and 1000 ms), comparing two contrast agents (12 mmol/kg i.v.): (a) D-GLC and (b) 3-OMG. These Z-spectra were analyzed using five-pool Lorentzian fitting with a pixel-wise method.

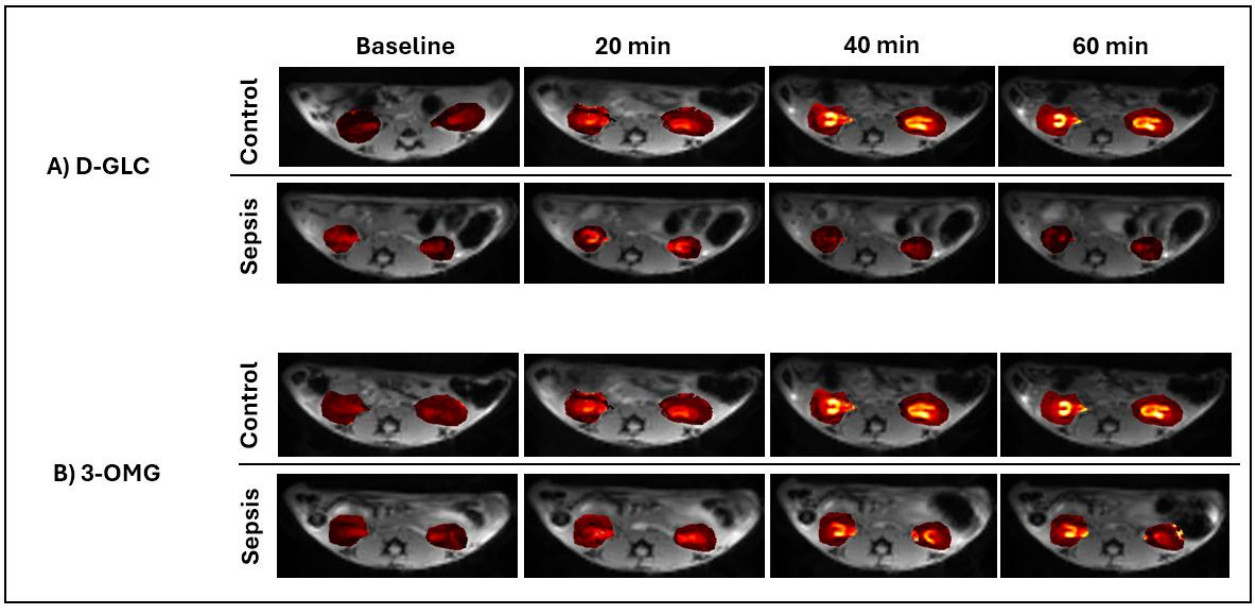

Figure 50: Representative glucoCEST maps of healthy and S-AKI animals were obtained from pre-injection to 60 minutes post-injection using the seg-FLASH sequence (with 2 µT and 1000 ms), comparing two contrast agents (12mmol/kg i.v.): (A) D-GLC and (B) 3-OMG. These color maps were analyzed using a five-pool Lorentzian fitting with a pixel-wise method.

- **3-OMG group results:**

We applied the same protocol for the 3-OMG injection as used for the D-GLC injection. 3-OMG was administered at a dose of 12 mmol/kg to both the healthy (n = 8) and septic (n = 8) groups. Mice were then measured by glucoCEST MRI at four time points: pre-injection and post-injection at 20, 40, and 60 minutes. This evaluation illustrates the trends of the glucose signal observed in the 3-OMG group and compares them to those in the D-GLC administration group.

Baseline: No significant differences were found between the control and septic groups at pre-injection (Figure 51). $AUC_{Lorentz}$ values in the pelvis, medulla, and cortex were comparable across both groups (Figure 51), indicating stable baseline glucoCEST signals before injection.

Post-injection 20 minutes: A significant reduction in the $AUC_{Lorentz}$ was observed in the septic group in both the pelvis (0.792 ± 0.300 vs. 1.475 ± 0.218) and medulla (0.535 ± 0.255 vs. 1.002 ± 0.228) compared to the control group (Figure 51). The 3-OMG group showed a similar trend, with the cortex signal of the control group (0.388 ± 0.108) closer

to the sepsis group (0.327 ± 0.166). This suggests that both D-GLC and 3-OMG increase glucose uptake in the pelvis and medulla regions, while the septic group shows reduced glucose uptake.

Post-injection 40 minutes: The trend continued, with significant differences between the control and septic groups in the pelvis (1.983 ± 0.242 vs. 0.890 ± 0.326) and medulla (1.082 ± 0.263 vs. 0.616 ± 0.236). The cortex signal showed no significant difference between the groups (control: 0.404 ± 0.045, sepsis: 0.334 ± 0.089). Compared to D-GLC, the 3-OMG group showed a slight increase in the control group's signal and a slight decrease in the septic group (Figure 51).

Post-injection 60 minutes: The septic group showed little change in glucose signal compared to the 20 and 40-minute phases (0.925 ± 0.356), significantly lower than the control group (2.257 ± 0.285, $P < 0.001$). In contrast, the control group showed a continued increase in the pelvis signal and a decrease in the medulla (0.826 ± 0.196). The cortex signal in both groups remained similar (control: 0.297 ± 0.056, sepsis: 0.367 ± 0.187).

This final time point showed that the glucoCEST signal in the control group continued to rise in the pelvis, while it decreased in the medulla (Figure 51). In the septic group, the signal remained stable. The glucoCEST signal was consistently higher in the control group for both D-GLC and 3-OMG injections, with a decreasing trend in the medulla and cortex after 60 minutes in both groups. However, the pelvis signal in the 3-OMG group continued to rise, unlike the D-GLC group, where it decreased across all regions.

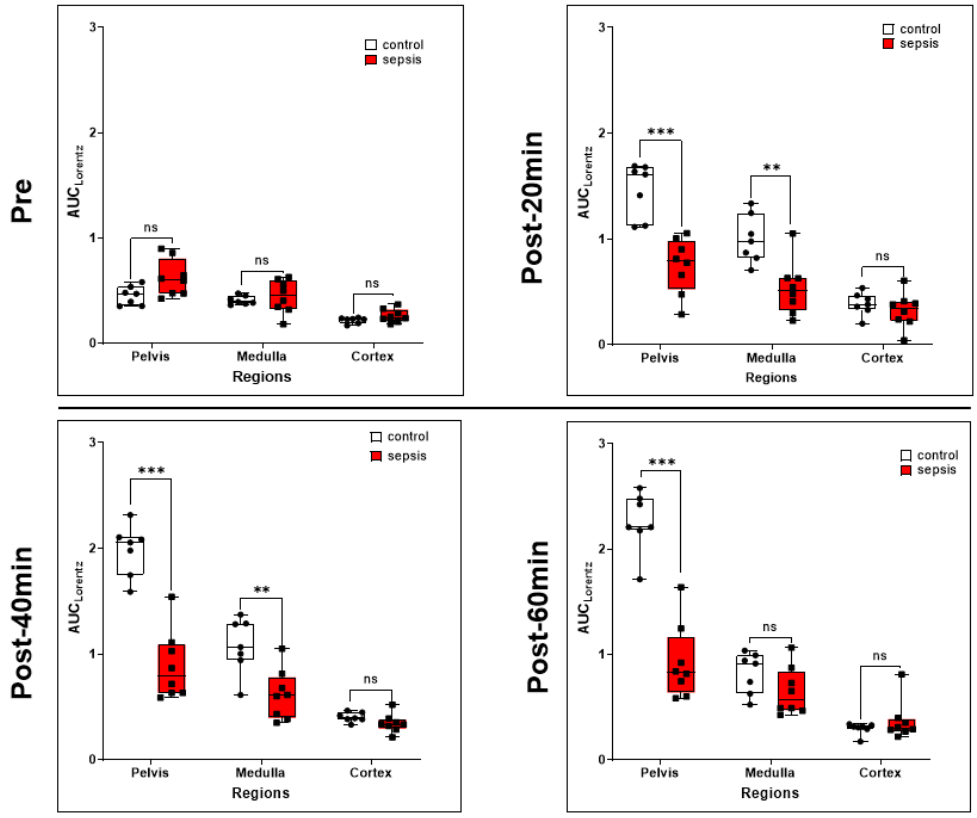

Figure 51: This graph shows the changes in glucoCEST signal at pre- and post-injection using 3-OMG glucose as a contrast agent (12 mmol/kg, i.v.) between the control (n = 8) and septic (n = 8) groups across the pelvis, medulla, and cortex regions. Error bars represent SD. *P < 0.05; **P < 0.01; ***P < 0.001; n.s.

4.3.2.2 Histological and blood test presentation

- **Serum markers**

This investigation aimed to (1) verify and confirm the glucoCEST results and (2) interpret these results in relation to serum markers. Blood was collected from septic mice one hour after MRI scanning, following six hours of sepsis, and analyzed separately for D-GLC and 3-OMG to examine their effects on blood markers in the S-AKI group (see Figure 52).

After seven hours of infection, creatinine levels significantly increased in the septic group injected with D-GLC (P = 0.0394), with levels rising from 0.188 ± 0.043 mg/dL in controls to 0.314 ± 0.093 mg/dL in the septic group. The 3-OMG-injected septic group showed a similar increase in creatinine (0.281 ± 0.121 mg/dL), but this was not statistically significant (P = 0.3394).

Urea levels also increased significantly in the septic groups (Figure 52). In the D-GLC(septic group), urea levels were 57.86 ± 10.843 mg/dL, and in the 3-OMG(septic group), levels were 56.143 ± 7.010 mg/dL, both significantly higher than the control group (26.50 ± 1.732 mg/dL, $P = 0.0061$).

HDL levels were significantly reduced in both septic groups compared to controls (30.250 ± 4.573 mg/dL). In the D-GLC (septic group), HDL decreased to 19.857 ± 6.283 mg/dL ($P = 0.0091$), and in the 3-OMG GLC(septic group), it decreased to 19.714 ± 5.823 mg/dL ($P = 0.0152$).

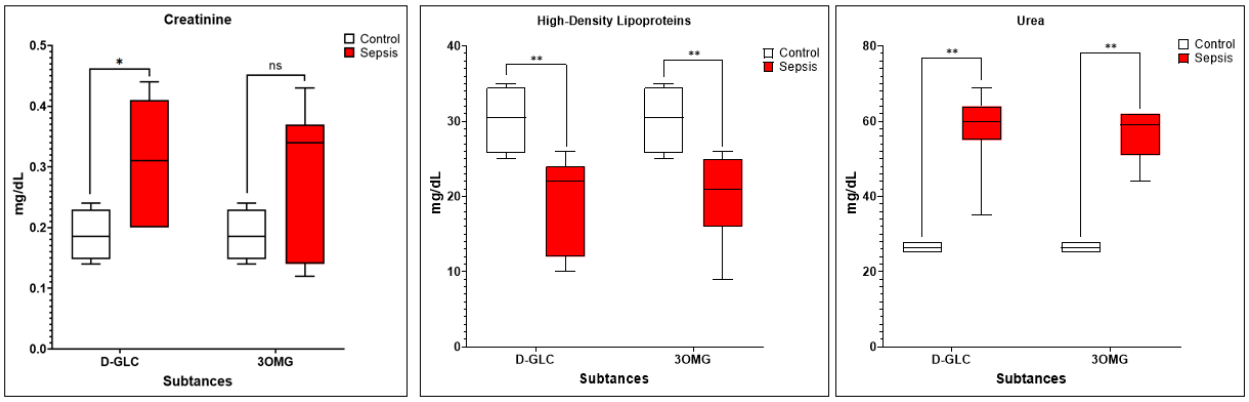

Figure 52: Comparison of biochemical markers between control (n = 4) and sepsis groups (n = 14) for two the two contrast agents: D-GLC and 3-0MG (12 mmol/kg). The box plots show creatinine measurements, high-density lipoproteins (HDL), and urea. Asterisks indicate significant differences between the control and sepsis groups. A single asterisk (*) indicates a $P < 0.05$, while double asterisks (**) indicate a $P < 0.01$.

- **Blood glucose**

In addition to confirming results with glucoCEST MRI, blood glucose levels were measured to assess changes following D-GLC and 3-OMG injections. These indices also reflect the impact of 3-OMG on blood glucose as a non-metabolized glucose. Figure 53 shows blood glucose measurements at two time points: before and one hour after MRI scanning. In the D-GLC group (Figure 53A), the septic group's blood glucose was significantly lower than the control group before injection (209 ± 49.3 vs. 44.6 ± 8.8, $P < 0.001$). After injection (12 mmol/kg, i.v.), blood glucose increased in both groups (541 ± 75.7 vs. 320 ± 61.0, $P < 0.001$). In the 3-OMG group (Figure 53B), blood glucose increased in the control group but less than in the D-GLC group (196 ± 17.0 vs. 304.4 ± 52.2). In the septic group, blood glucose slightly increased after 3-OMG injection (45.4 ± 10.4 vs. 77.8

± 11.6), suggesting that 3-OMG affects blood glucose levels, despite not being metabolized like D-GLC.

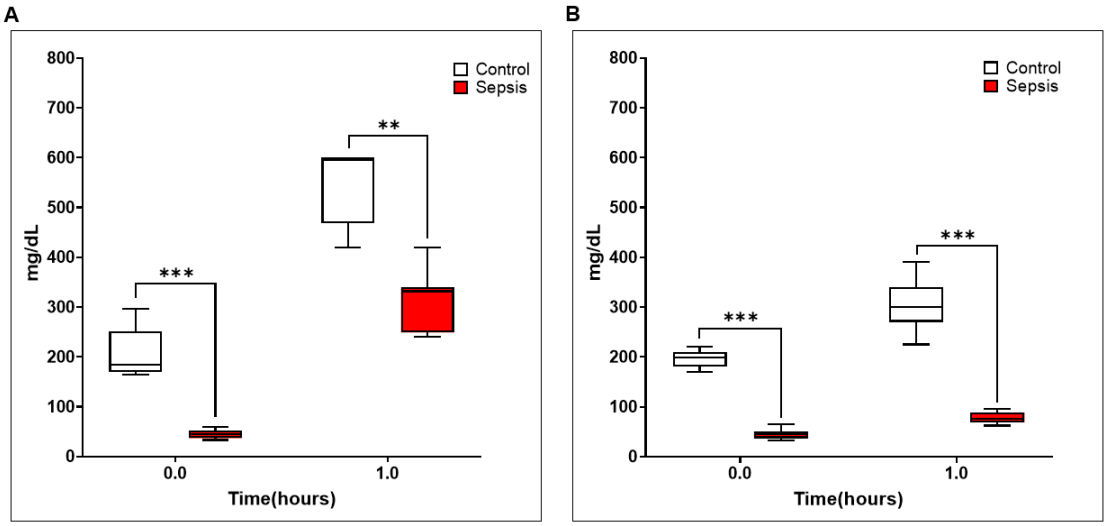

Figure 53: Graphs illustrate blood glucose levels in the control and septic groups using two the two different contrast agents: D-GLC (n = 16) and 3-OMG (n = 16) by i.v administration (dose: 12 mmol/kg) , D-GLC (A) and 3-OMG (B). Blood glucose levels were measured before and after MRI one hour using a blood test kit. Error bars represent SD. *P <0.05; **P <0.01; ***P <0.001; n.s.

4.3.2.3 Inter-parameter correlation results

To assess the relevance of MRI-derived biomarkers in S-AKI, Pearson correlation analysis was performed between imaging parameters (e.g., glucoCEST, T_1/T_2 mapping, AACID) and blood biochemical markers (e.g., glucose, creatinine, urea, HDL, LDL, CK). This analysis aimed to evaluate how well MRI metrics reflect systemic and renal metabolic changes.

- **GlucoCEST and Blood test**

Table 8 presents the correlation analysis between blood-based biochemical indices and glucoCEST signal across kidney regions (pelvis, medulla, cortex), summarized in Table 8A (D-GLC group) and Table 8B (3-OMG group). These correlations were assessed pre- and post-glucose injection, as well as for pre- and post-injection subtraction (delta). In the D-GLC group (Panel A), strong to very strong correlations were observed between post-injection glucose levels and CEST signal in all kidney regions ($r > 0.70$, with $r = 0.942$ in the cortex). In the 3-OMG group (Panel B), moderate to strong correlations were noted, especially in the cortex and medulla. Lipid-related markers (e.g., HDL, LDL, non-HDL) and

creatinine showed moderate correlations with CEST signal changes, particularly in the D-GLC group. Correlation strength and patterns varied depending on the compound administered and the kidney region analyzed.

A) D-GLC

Lab/MRI index	CEST-signal (Pre)			CEST-signal (Post)			CEST-signal (delta)		
	Pelvis	Medulla	Cortex	Pelvis	Medulla	Cortex	Pelvis	Medulla	Cortex
Glucose (Pre)	0.385 (n.s)	0.301 (n.s)	0.328 (n.s)	-	-	-	0.942 (***)	0.606 (*)	0.606 (*)
Glucose (Post)	-	-	-	0.760 (*)	0.819 (***)	0.728 (**)	0.765 (**)	0.716 (**)	0.620 (*)
Glucose (Delta)	-	-	-	-	-	-	0.171 (n.s)	0.450 (n.s)	0.305 (n.s)
Creatinine	0.175 (n.s)	0.397 (n.s)	0.159 (n.s)	-0.47 (n.s)	-0.478 (n.s)	-0.28 (n.s)	-0.53 (n.s)	-0.527 (n.s)	-0.29 (n.s)
Urea	-0.21 (n.s)	-0.261 (n.s)	-0.484 (n.s)	-0.83 (**)	-0.672 (n.s)	-0.48 (n.s)	-0.84 (**)	-0.732 (*)	-0.64 (*)
HDL	0.092 (n.s)	-0.539 (n.s)	-0.053 (n.s)	0.675 (*)	0.779 (**)	-0.05 (n.s)	0.607 (n.s)	0.512 (n.s)	0.420 (n.s)
LDL	-0.32 (n.s)	-0.558 (n.s)	-0.275 (n.s)	0.099 (n.s)	0.275 (n.s)	-0.28 (n.s)	0.012 (n.s)	0.241 (n.s)	0.064 (n.s)
Non-HDL	-0.23 (n.s)	-0.796 (**)	-0.467 (n.s)	0.188 (n.s)	0.352 (n.s)	-0.47 (n.s)	0.185 (n.s)	0.212 (n.s)	-0.02 (n.s)
CK	0.096 (n.s)	-0.312 (n.s)	0.056 (n.s)	0.525 (n.s)	0.537 (n.s)	0.056 (n.s)	0.518 (n.s)	0.340 (n.s)	0.076 (n.s)
Triglyceride	0.001 (n.s)	-0.453 (n.s)	-0.111 (n.s)	0.329 (n.s)	0.354 (n.s)	-0.11 (n.s)	0.270 (n.s)	-0.170 (n.s)	-0.35 (n.s)

B) 3-OMG

Lab/MRI index	CEST-signal (Pre)			CEST-signal (Post)			CEST-signal (delta)		
	Pelvis	Medulla	Cortex	Pelvis	Medulla	Cortex	Pelvis	Medulla	Cortex
Glucose (Pre)	-0.53 (*)	-0.147 (n.s)	-0.455 (n.s)	-	-	-	-0.53 (*)	-0.147 (n.s)	-0.455 (n.s)
Glucose (Post)	-	-	-	0.808 (***)	0.662 (**)	0.185 (n.s)	-0.52 (*)	-0.131 (n.s)	-0.435 (n.s)
Glucose (Delta)	-	-	-	-	-	-	0.765 (***)	0.474 (n.s)	0.149 (n.s)
Creatinine	0.11 (n.s)	-0.470 (n.s)	-0.291 (n.s)	-0.09 (n.s)	-0.105 (n.s)	0.191 (n.s)	-0.28 (n.s)	-0.240 (n.s)	-0.429 (n.s)
Urea	0.541 (n.s)	0.024 (n.s)	0.115 (n.s)	-0.68 (*)	-0.697 (*)	-0.285 (n.s)	-0.77 (**)	-0.574 (n.s)	-0.207 (n.s)
HDL	-0.55 (n.s)	-0.312 (n.s)	-0.40 (n.s)	0.689 (*)	0.659 (*)	0.133 (n.s)	0.861 (***)	0.816 (**)	0.580 (n.s)
LDL	-0.24 (n.s)	-0.195 (n.s)	-0.056 (n.s)	-0.29 (n.s)	-0.209 (n.s)	-0.43 (n.s)	-0.02 (n.s)	0.206 (n.s)	0.344 (n.s)
Non-HDL	0.024 (n.s)	0.145 (n.s)	0.073 (n.s)	-0.30 (n.s)	-0.281 (n.s)	-0.43 (n.s)	-0.11 (n.s)	0.064 (n.s)	0.363 (n.s)
CK	0.188 (n.s)	0.297 (n.s)	0.168 (n.s)	0.467 (n.s)	0.410 (n.s)	-0.07 (n.s)	0.392 (n.s)	0.309 (n.s)	0.039 (n.s)
Triglyceride	-0.04 (n.s)	0.059 (n.s)	-0.160 (n.s)	0.217 (n.s)	0.045 (n.s)	-0.224 (n.s)	0.270 (n.s)	0.156 (n.s)	0.073 (n.s)

Table 8: Correlation between glucoCEST signals and laboratory indices in D-GLC (A) and 3-OMG (B) groups. This figure illustrates the relationship between pre- and post-injection CEST signals and blood biochemical markers (e.g., glucose, creatinine, HDL, LDL, CK, etc.) across three kidney regions: pelvis, medulla, and cortex. Red: very strong correlation (r = 0.90–1.0); Yellow: strong (r = 0.70–0.90); Green: moderate (r = 0.50–0.70); Blue: weak or negligible (r < 0.50). Statistical significance is denoted as follows: **P* <0.05, ***P* <0.01, ****P* <0.001, and n.s.

- **CEST, mapping and Blood test**

Table 9 shows the correlation patterns between various laboratory indices and MRI-derived quantitative parameters in renal tissues (pelvis, medulla, cortex). In Panel A, T_1 and T_2 relaxation times (pre- and post-glucose administration) were analyzed. T_1 values showed weak correlations with most lab indices across all regions, except for a moderate-to-strong correlation between T_1 (Pre) in the medulla and CK levels (r = 0.742). T_2 parameters, especially T_2 (Pre) and T_2 (Post), showed stronger and more consistent correlations. For example, glucose (Post) and glucose delta had strong correlations with T_2 values in the pelvis and medulla (r ~ 0.68 to 0.78). Urea and creatinine showed moderate-to-strong correlations with T_2 signals in the medulla and cortex post-glucose, indicating T_2's sensitivity to renal functional changes. Panel B evaluates correlations between lab values and CEST contrast metrics (APT, NOE, and MTC). Fewer strong correlations were observed compared to relaxation times. Fewer strong correlations were observed compared to relaxation times. Notably, MTC in the medulla showed moderate

correlations with creatinine and LDL (r = 0.672 and 0.597, respectively), and APT signals had some association with HDL in both the medulla and cortex (r ≈ 0.50–0.58), while other parameters were mostly non-significant. In summary, T_2 relaxation times were the most sensitive to glucose and kidney markers, while T_1 showed a few relevant connections. CEST contrasts mainly correlated with lipid-related markers.

A)

Lab/MRI index	T1 (Pre)			T2 (Pre)			T2 (Post)		
	Pelvis	Medulla	Cortex	Pelvis	Medulla	Cortex	Pelvis	Medulla	Cortex
Glucose (Pre)	0.457 (n.s)	0.437 (n.s)	0.456 (n.s)	0.784 (**)	0.73 (**)	0.686 (*)			
Glucose (Post)	-	-	-	-	-	-	0.50 (n.s)	0.705 (*)	0.698 (*)
Glucose (Delta)	-	-	-	-	-	-	-	-	-
Creatinine	0.172 (n.s)	-0.432 (n.s)	0.003 (n.s)	-0.46 (n.s)	-0.654 (*)	-0.636 (*)	-0.44 (n.s)	-0.477 (n.s)	-0.406 (n.s)
Urea	-0.30 (n.s)	-0.469 (n.s)	-0.528 (n.s)	-0.83 (**)	-0.874 (**)	-0.795 (**)	-0.47 (n.s)	-0.657 (n.s)	-0.763 (*)
HDL	0.5 (n.s)	0.755 (**)	-0.103 (n.s)	0.446 (n.s)	0.292 (ns.)	0.118 (n.s)	0.172 (n.s)	0.319 (n.s)	0.477 (n.s)
LDL	0.292 (n.s)	0.375 (n.s)	-0.054 (n.s)	-0.34 (n.s)	-0.295 (n.s)	-0.46 (n.s)	0.680 (*)	-0.309 (n.s)	-0.483 (n.s)
Non-HDL	-0.14 (n.s)	0.463 (n.s)	-0.351 (n.s)	-0.13 (n.s)	-0.036 (n.s)	-0.191	0.160 (n.s)	0.155 (n.s)	0 (n.s)
CK	0.1 (n.s)	0.742 (**)	0.132 (n.s)	0.251 (n.s)	0.168 (n.s)	0.044 (n.s)	0.567 (n.s)	0.560 (n.s)	0.620 (n.s)
Triglyceride	0.299 (n.s)	0.226 (n.s)	-0.359 (n.s)	0.138 (n.s)	-0.244 (n.s)	-0.199 (n.s)	0.539 (n.s)	0.349 (n.s)	0.480 (n.s)

B)

Lab/MRI index	APT		NOE		MTC	
	Medulla	Cortex	Medulla	Cortex	Medulla	Cortex
Glucose (Pre)	0.100 (n.s)	0.085 (n.s)	-0.018 (n.s)	-0.063 (n.s)	-0.222 (n.s)	-0.410 (n.s)
Creatinine	0.003 (n.s)	0.025 (n.s)	-0.114 (n.s)	0.071 (n.s)	0.672 (*)	0.139 (n.s)
Urea	-0.292 (n.s)	-0.212 (n.s)	-0.155 (n.s)	0.152 (n.s)	0.311 (n.s)	0.498 (n.s)
HDL	0.508 (n.s)	0.448 (n.s)	0.271 (n.s)	0.113 (n.s)	-0.597 (n.s)	-0.370 (n.s)
LDL	0.049 (n.s)	0.168 (n.s)	0.331 (n.s)	0.287 (n.s)	-0.631 (*)	0.047 (n.s)
Non-HDL	0.091 (n.s)	0.007 (n.s)	0.060 (n.s)	0.006 (n.s)	-0.593 (n.s)	0.057 (n.s)
CK	0.294 (n.s)	0.423 (n.s)	0.055 (n.s)	0.080 (n.s)	-0.287 (n.s)	-0.376 (n.s)
Triglyceride	0.587 (n.s)	0.333 (n.s)	-0.158 (n.s)	0.036 (n.s)	0.062 (n.s)	-0.360 (n.s)

Table 9: Correlation between relaxation parameters (T_1, T_2) and CEST MRI index (APT, NOE, MTC) with laboratory indices in D-GLC and 3-OMG groups. (A) shows the correlation of T_1 and T_2 (pre and post-injection) with lab markers. (B) depicts the association between APT, NOE, and MTC metrics with the same biomarkers. Color coding: Red (very strong), Yellow (strong), Green (moderate), Blue (weak/negligible), with correlation ranges as above. The values reflect metabolic and structural MRI responsiveness to glucose analog administration. Statistical significance is denoted as follows: *P <0.05, **P <0.01, ***P <0.001, and n.s.

- **GlucoCEST and Blood test**

Table 10 shows the correlation matrices between serum biomarkers and AACID values in different renal regions (pelvis, medulla, cortex), assessed at both pre- and post-injection time points for D-GLC (A) and 3-OMG (B).

- In the D-GLC group (Table 10A):

Post-injection AACID values in the cortex strongly correlated with LDL (r = 0.895), while moderate-to-strong correlations were observed between urea and AACID values in pelvis and medulla (r = 0.750 and 0.537). Pre-injection CEST signal in the cortex showed a moderate correlation with AACID (r = 0.525), and post-injection CEST signals in the pelvis were significantly associated with AACID (r = 0.686).

- In the 3-OMG group (Figure 12B):

Stronger correlations were found, especially between post-injection glucose and AACID values in the pelvis and medulla (r = 0.681 and 0.416). HDL and non-HDL cholesterol showed strong inverse correlations with AACID in the cortex post-3-OMG (r = –0.717 for non-HDL), indicating AACID's sensitivity to lipid profiles. A robust correlation between pre-injection CEST signal and AACID in the cortex was observed (r = 0.797), supporting its role in detecting glucose analog uptake.

Overall, these matrices suggest that both AACID and CEST parameters are sensitive to renal metabolic changes following glucose analog administration, with slight differences in regional and biomarker-specific responses between the D-GLC and 3-OMG groups.

A) D-GLC

Lab/MRI index	AACID (Pre)			AACID (Post)		
	Pelvis	Medulla	Cortex	Pelvis	Medulla	Cortex
Glucose (Pre)	-0.035 (n.s)	-0.231 (n.s)	0.178 (n.s)	-	-	-
Glucose (Post)	-	-	-	0.559 (n.s)	0.256 (n.s)	0.057 (n.s)
Creatinine	0.284 (n.s)	0.459 (n.s)	0.131 (n.s)	-0.404 (n.s)	0.321 (n.s)	0.162 (n.s)
Urea	0.233 (n.s)	0.309 (n.s)	-0.200 (n.s)	-0.700 (*)	0.537 (n.s)	0.285 (n.s)
HDL	0.035 (n.s)	-0.274 (n.s)	0.173 (n.s)	0.750 (n.s)	0.375 (n.s)	0.436 (n.s)
LDL	-0.011 (n.s)	-0.030 (n.s)	-0.061 (n.s)	-0.015 (n.s)	0.680 (*)	0.895 (***)
Non-HDL	0.171 (n.s)	-0.073 (n.s)	-0.062 (n.s)	0.166 (n.s)	0.597 (n.s)	0.456 (n.s)
CK	-0.028 (n.s)	-0.148 (n.s)	0.008 (n.s)	0.440 (n.s)	0.319 (n.s)	0.086 (n.s)
Triglyceride	0.322 (n.s)	-0.015 (n.s)	0.170 (n.s)	0.183 (n.s)	0.272 (n.s)	-0.126 (n.s)
CEST-signal (Pre)						
Pelvis	0.355 (n.s)	-	-	-	-	-
Medulla	-	-0.183 (n.s)	-	-	-	-
Cortex	-	-	0.525 (*)	-	-	-
CEST-signal (Post)						
Pelvis	-	-	-	0.686 (**)	-	-
Medulla	-	-	-	-	0.190 (n.s)	-
Cortex	-	-	-	-	-	-0.241 (n.s)

B) 3-OMG

Lab/MRI index	AACID (Pre)			AACID (Post)		
	Pelvis	Medulla	Cortex	Pelvis	Medulla	Cortex
Glucose (Pre)	-0.510 (n.s)	-0.506 (n.s)	-0.484 (n.s)	-	-	-
Glucose (Post)	-	-	-	0.681 (*)	0.416 (n.s)	-0.454 (n.s)
Creatinine	0.226 (n.s)	0.436 (n.s)	0.370 (n.s)	-0.616 (n.s)	-0.513 (n.s)	0.083 (n.s)
Urea	0.035 (n.s)	0.273 (n.s)	0.286 (n.s)	-0.755 (*)	-0.394 (n.s)	-0.413 (n.s)
HDL	-0.764 (*)	-0.343 (n.s)	-0.302 (n.s)	0.748 (*)	0.372 (n.s)	-0.049 (n.s)
LDL	-0.333 (n.s)	0.362 (n.s)	0.469 (n.s)	0.128 (n.s)	0.355 (n.s)	-0.420 (n.s)
Non-HDL	-0.508 (n.s)	-0.181 (n.s)	-0.091 (n.s)	0.211 (n.s)	0.448 (n.s)	-0.717 (*)
CK	-0.344 (n.s)	-0.414 (n.s)	-0.387 (n.s)	0.310 (n.s)	0.472 (n.s)	-0.355 (n.s)
Triglyceride	-0.640 (*)	-0.516 (n.s)	-0.557 (n.s)	-0.038 (n.s)	-0.336 (n.s)	-0.133 (n.s)
CEST-signal (Pre)						
Pelvis	0.402 (n.s)	-	-	-	-	-
Medulla	-	0.510 (n.s)	-	-	-	-
Cortex	-	-	0.797 (***)	-	-	-
CEST-signal (Post)						
Pelvis	-	-	-	0.698 (n.s)	-	-
Medulla	-	-	-	-	0.417 (n.s)	-
Cortex	-	-	-	-	-	0.207 (n.s)

Table 10: This figure shows the correlation of AACID values and glucoCEST signals with laboratory indices in D-GLC (A) and 3-OMG (B), including both pre- and post-injection AACID values and their relationship with blood biomarkers and CEST signal changes in the pelvis, medulla, and cortex. Color coding: Red (r = 0.90–1.0), Yellow (r = 0.70–0.90), Green (r = 0.50–0.70), Blue (r < 0.50). The matrix highlights how AACID may reflect pH- or metabolite-related shifts in septic kidney physiology after different glucose administrations. Statistical significance: *P <0.05, **P <0.01, ***P <0.001, n.s.

4.3.2.4 Immunohistochemistry results

To assess renal GLUT1, GLUT2, and HK2 expression, we performed indirect immunofluorescence with high-resolution microscopy, expressing the values as percentage of area (%Area).

Figure 54 shows distinct differences in GLUT expression between control and septic mice. In the control group, the proximal convoluted tubules (PCT) appear more rounded with less space, indicating healthier tubules. This is further supported by the increased expression of HK2 in the septic group (Figure 55), suggesting tubule degeneration and higher immune cell presence. GLUT1 and GLUT2 expressions were higher in the control group. Specifically, in the cortex, GLUT1 and GLUT2 %Area was 53.30 and 58.92, respectively, while in the medulla, they were 62.23 and 44.74. In contrast, the septic group showed a reduced GLUT expression, with %Area of 40.09 (GLUT1) in the cortex and 37.44 in the medulla, and %Area of 34.17(GLUT2) in the cortex and 31.33 in the medulla. Additionally, the septic group had higher HK2 expression, with %Area values of 59.77 in the cortex and 51.75 in the medulla, compared to 30.82 and 30.73 in the control group.

These results suggest that septic conditions lead to a downregulation of GLUT transporters and an upregulation of HK2 expression, which may be indicative of metabolic shifts and cellular stress in the kidney.

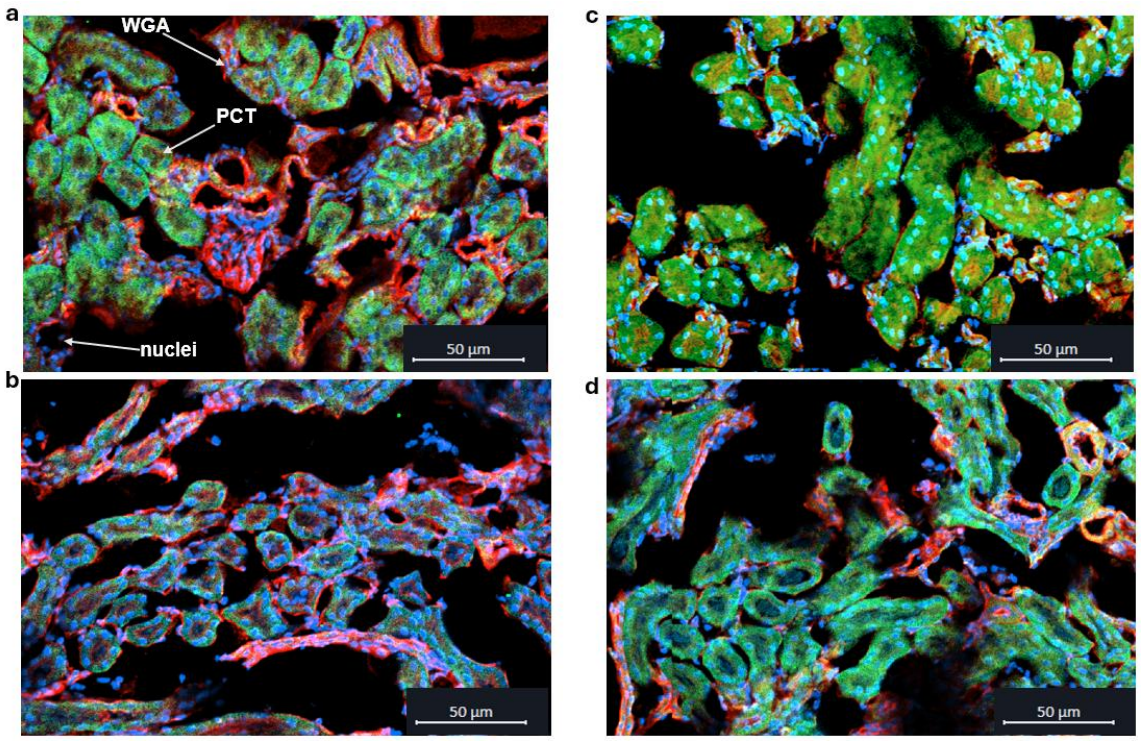

Figure 54: Assessment of the expression of GLUT in the kidney of control mice compared to septic mice. Representative images of GLUT1 (a,b) and GLUT2 (c,d). Nuclei were counterstained as blue, Wheat germ agglutinin (WGA) as red and GLUT around PCT as green.

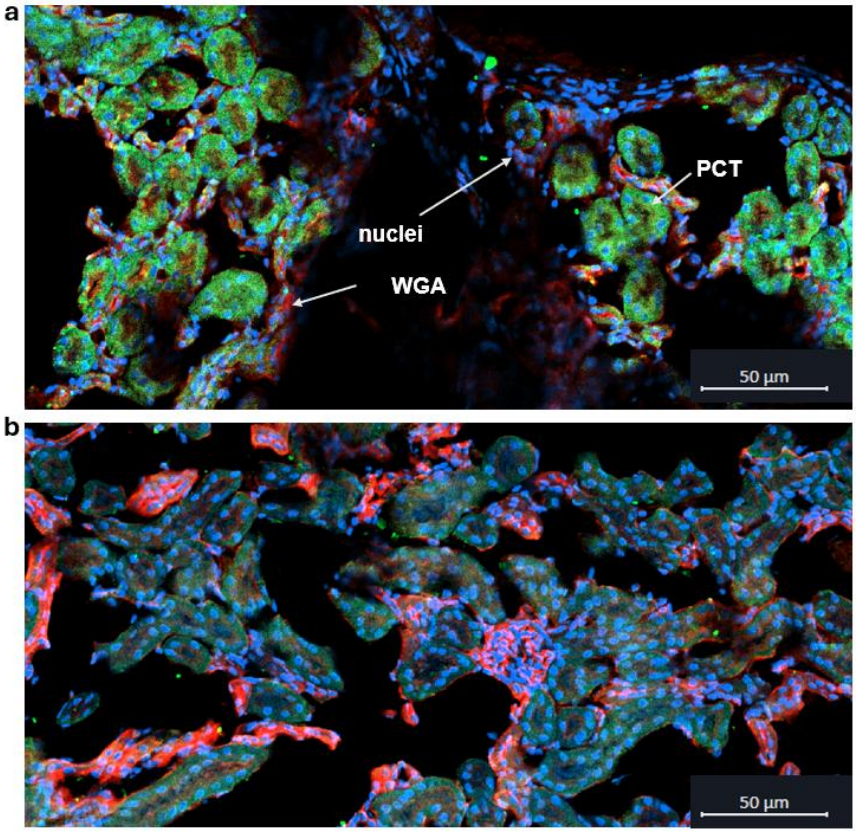

Figure 55: Assessment of the expression of HK2 in the kidney of control mice compared to septic mice. Representative images of HK2 (a) in control mice and HK2 (b) in septic mice. Nuclei were counterstained as blue, WGA as red and GLUT around PCT as green.

4.4 Discussion

- **In-vitro validation phase:**

The results showed the influence of MRI parameters, such as t_{sat} and B_1 level, on the glucose CEST effect across different pulse sequences. The validation phase is essential for selecting the optimal CEST parameters to maximize the effect. Both D-GLC and 3-OMG phantoms show similar trends in the CEST effect for varying B_1 power and t_{sat} values. In the D-GLC phantom, with t_{sat} of 1000 ms and B_1 levels ranging from 0.5 to 4 µT, the CEST effect increases as B_1 increases from 0.5 to 3 µT. However, beyond 3 µT, the effect decreases, likely due to high power saturation pulses leading to water direct saturation effects (P. Z. Sun, Lu, Wu, Xiao, & Wu, 2013). Moreover, choosing a lower B_1 value can be advantageous for CEST contrast detection, as it helps reduce MTC, which can interfere with the CEST effect(G. Liu, Song, Chan, & McMahon, 2013). In this dependence parameter validation, we also observed that the CEST effect acquired with

B_1 = 2 μT reached a plateau at longer t_{sat} (>1000 ms), which indicates that it is approaching steady-state conditions(Phillip Zhe Sun, 2012).

The results show that the CEST effect for the D-GLC phantom is slightly stronger than the 3-OMG phantom when using the same B_1 (under 3μT) and saturation time parameters. This difference can be explained by the mutarotation process, where the alpha and beta anomers ratio affects the exchange rate, as the beta anomer has a faster exchange rate. For example, 3-OMG has a β:α ratio of 58:42, while D-GLC has a β:α ratio of 64:36(Anemone et al., 2021).

This validation also demonstrates differences in the CEST signal between the UTE, seg-FLASH, and RARE pulse sequences. The CEST effects of UTE and seg-FLASH are similar, but the RARE sequence shows a weaker glucose signal. As shown in Table 9, UTE and seg-FLASH have much shorter TE values than RARE. A longer TE prevents magnetization from returning to its initial value, reducing the signal during subsequent rephases, explaining the lower CEST effect observed with RARE. Furthermore, the T1* effect, caused by factors such as flip angle, TR, and RF inhomogeneity, contributes to the reduced glucoCEST effect observed with the RARE sequence (Bhuva et al.).

- **In-vivo phase:**
  - **Laboratory results**

In this study, index like creatinine, HDL and urea were analyzed from the blood. It was used to detect inflammation of the body. However, these parameters normally are underestimated due to the influence by factors such as muscle mass structure and other factors(Ávila, Mora Sánchez, Bernal Amador, & Paniagua, 2025; Baxmann et al., 2008).

According to the laboratory blood results, creatinine increased significantly in the sepsis group compared to the control group. The elevation of creatinine in diseased group happened due to the reduction of glomerular filtration capacity in S-AKI (Peerapornratana et al., 2019). Reducing the kidney's function increases the accumulation of creatinine in the blood. It causes the accumulation of urea, as urea is a protein degradation product filtered by the kidneys and excreted in the urine. The blood results show that urea had the same increasing trend as creatinine in the septic group. In inflammatory disease, HDL indicates the systemic response to an infection as it plays an important role in vascular protection, immune regulation and anti-inflammation. As a result, HDL decreases in the septic group, and this change would be a sign of lipid metabolism disorders and endothelial damage(Jiang et al., 2023).

Besides creatinine, urea and HDL, other blood metrics such as LDL, Non-HDL, creatine kinase (CK), and triglycerides were analyzed. In the six-hour S-AKI model, no significant changes were observed in LDL, Non-HDL, CK, or triglyceride levels between the control and sepsis groups, likely due to the insufficient severity of the inflammatory response and kidney damage within this short timeframe(Roveran Genga et al., 2017; Z. Zhang, 2015).

❖ **Immunohistochemistry**

The IHC results show that the structure of PCT changed in the septic group. It could be responsible for the decreased glucoCEST signal, as kidney function related to reabsorption and filtration is impaired. In addition, the higher presence of nuclei in the septic group suggests more apparent immune cells as a sign of inflammation(L. Chen et al., 2018). Furthermore, the over-expression of HK2 in the septic group suggests that hypoxia, which is known to trigger the activation of hypoxia-inducible factors, contributes to these changes(J. Chen, Li, Sun, Li, & Chen, 2024). It could indicate an adaptive response to low oxygen conditions, potentially altering the metabolic pathways in the kidneys.

The observed differences in the glucoCEST contrast after the application of D-GLC or 3-OMG were reflected in higher $AUC_{Lorentz}$ values in pelvis for 3-OMG. This suggests that the use of 3-OMG may have additional effects on renal tissue structure and function. It is already recognized that uncontrolled high glucose levels can increase free radical production, which disrupts the nicotinamide adenine dinucleotide (NADH) redox ratio and leads to oxidative stress at the cellular level(Scheen, Giraud, & Bendjelid, 2021; Tain, Xu, Zhou, Li, & Cai, 2016; Thakur, Alcoreza, Cazares, & Chattopadhyay, 2021). However, due to the limited scope of this thesis, further investigation is required to assess the toxicity effects of using D-GLC and 3-OMG.

❖ **The interpretation of MRI data**

S-AKI has been considered an acute inflammatory disease. In the acute inflammatory phase, some alterations occur in the kidneys, such as cell swelling, capillary leakage, and interstitial edema formation(Konigsfeld et al., 2019). It leads to a change in relaxation times. The change was observed on T_2 mapping; it showed a decrease in T_2 values in a septic group compared to the control group, with this change being more prominent in the pelvis. This may be due to the decreased water content, urine production and increased

urinary viscosity in kidneys(W. T. Zhao et al., 2023). In addition, there was no remarkable renal edema that was detected by T_2 mapping. T_1 values, which were unchanged, confirmed these results. It suggests that the renal cells in our model were not severely damaged. In the post-injection phase, the decrease of T_2 values was observed in control groups using both D-GLC and 3-OMG injection methods. This decrease was noticeably prominent in the pelvis region and less pronounced in the 3-OMG injection method. This change may be due to the effect of glucose on the blood viscosity and causes resistance in the blood flow(Mushtaq, Abdul Mateen, & Kim, 2019). In addition, there was no significant difference before and after glucose injection in septic groups. It might be because of the reduced tissue perfusion in S-AKI, which was also reflected in the glucoCEST results.

The CEST MRI results show benefit of using the glucoCEST technique to assess renal function in S-AKI. The increase in glucoCEST contrast is likely due to changes in renal perfusion and the adaptive metabolic down-regulation of renal tubular cells in response to injury(Chvojka et al., 2008). Regarding renal perfusion, the kidney's filtering function is affected, which is why the expected decrease in glucose signal seen in the control group post-injection is not observed in the S-AKI group.

A literature review on AKI identifies three primary factors contributing to its development: inflammation and oxidative stress, abnormalities in microcirculation, and adaptive downregulation of cellular metabolism, renal tubules respond to damage. Therefore, assessing the AKI must be based on the connection between the CEST signal and the mechanism that causes AKI. In the AKI condition, glycolysis is activated. In a normal physiological state, proximal tubule cells produce ATP through aerobic respiration. However, in the early stages of sepsis, these cells switch to glycolysis to meet energy needs(C. Liu et al., 2024). Moreover, studies on glucose metabolism in the kidney have shown that the development of kidney disease is related to aerobic glycolysis or the Warburg effect. In addition, AKI is considered a disease caused by sepsis induction, so malignant cells will have high glycolysis metabolism because of increased hexokinase activity. Therefore, the down-regulated metabolism in S-AKI may also change glucoCEST contrast.

In addition to down-regulated metabolism, septic conditions in S-AKI also affect tissue perfusion properties, such as blood volume and vascular leakage. Based on the results,

we observe that the difference in glucoCEST signal between the control and sepsis groups is most evident at 20 minutes after D-GLC injection, particularly in the medulla and cortex. However, this difference is no longer observed at 40 and 60 minutes, with the difference only remaining in the medulla. This shows that blood flow might not be the leading cause of this difference(Kentrup et al., 2017). Although, this can be seen in the pelvis region when the glucoCEST signal in the control and sepsis groups is entirely different from 20 minutes to 60 minutes after injection. T-cell factors can also influence the difference in glucose signal. This factor mediates inflammatory processes that occur during sepsis. This increases vascular permeability, changing how glucose is transported into cells(Kentrup et al., 2017).

As mentioned above, significant differences in the glucoCEST signal were observed in the pelvis region between the control and septic groups at all time points following glucose injection. This could be because, after D-GLC injection, the D-GLC may be absorbed by the glomerulus in the cortex. The not-reabsorbed portion will pass through the medulla and be further concentrated through active sodium transport-driven water reabsorption in the tubular system, accumulating in the pelvis. The mechanism of glucose accumulation in the pelvis is similar to that of urea, as demonstrated in a previous study (Shin et al., 2020), which used a combination of urea injection and CEST MRI techniques to assess kidney function. The results of this study are also in agreement with studies using ^{13}C-labeled urea in combination with ^{13}C-MRI to evaluate kidneys.

In the 3-OMG injection group, the results showed a clear difference in the pelvis at all time points after injection which is similar to the D-GLC injection group. The medulla showed a similar trend, with differences observed at 20 and 40 minutes after injection, while the cortex showed no difference at any time point after injection.

In the septic groups injected with D-GLC or 3-OMG, the glucoCEST signal in the 3-OMG injection group is higher than that in the D-GLC injection group. This can be seen most clearly in the cortex and medulla when the 3-OMG injection group had no difference in glucose CEST at all times in the cortex between the control and septic groups. This difference may result from the differing chemical structures of the two sugars, D-GLC and 3-OMG. Previous studies have indicated that the difference in the signal between D-GLC and 3-OMG is caused by the effect of pH. The CEST effect of D-GLC tends to increase in an acidic environment, while that of 3-OMG tends to increase in a neutral

environment(Anemone et al., 2021). Although the septic condition makes the pH environment more acidic, this change is insignificant, as noted in previous studies on S-AKI. However, the disease model of that study is different. The study using CEST MRI and ^{31}P MRS showed that the pH only changed by 0.2 units in the severely damaged kidneys group compared to the control group (J. Liu et al., 2018). In addition to the pH factor that creates the signal difference between 3-OMG and D-GLC, the metabolic factor also plays an important role. As mentioned in the theoretical section, D-GLC is a type of sugar that can be metabolized, so after injection, the glucose signal would last shorter than 3-OMG. 3-OMG is a type of sugar that is not metabolized but still enters cells through GLUT 1 and 2 transport.(Akansha Ashvani Sehgal et al., 2019). This results in 3-OMG accumulating over time and remaining in the kidney longer than D-GLC. In other studies, when comparing the use of D-GLC and 3-OMG in disease condition such as brain tumors, 3-OMG had almost the same value as D-GLC in signal, and the CEST signal lasted longer than D-GLC (Rivlin & Navon, 2018; Akansha Ashvani Sehgal et al., 2019). This may require further research to understand better the nature of 3-OMG use in the S-AKI PCI model. This would be useful when using 3-OMG to assess GLUT status in S-AKI(Anemone et al., 2021; Jin et al., 2018).

In addition to the glucoCEST signal, information on the APT and NOE effects was extracted from the CEST data using the five-pool Lorentzian fitting algorithm. The results showed that APT and NOE parameters did not change significantly between the control and injured kidney groups. In principle, the APT effect is affected by many factors, such as mobile protein and peptide concentration and intracellular pH. Based on the APT results together with AACID values, it can be seen that pH or APT tended to decrease in the sepsis group, but this difference was not significant compared to the control group. This indicates that in S-AKI 6-hour disease, inflammation has not significantly changed the pH index, which agrees with other S-AKI articles(J. Liu et al., 2018). Considering the protein concentration factor, this factor changes due to increased water content in the tissue related to edema. However, in the T_2 mapping result, no remarkable renal edema was noted. Moreover, this result was also confirmed with T_1 mapping. In addition to the above factors, the change in mitochondrial function can also affect the APT parameter at offset 3.5 ppm. In this experiment, the Cr-CEST index was also quantified using the five-pool Lorentzian fitting algorithm, reflecting information about creatine related to mitochondrial dysfunction, oxidative damage, and inflammation(L. Chen et al., 2024). In

addition, because of the fast exchange nature of creatinine protons, this parameter can indirectly indicate changes in the pH environment due to inflammation (L. Chen et al., 2024) Moreover, the results showed that the Cr-CEST value had no significant change between the disease and healthy groups. Based on the results from glucoCEST, APT and creatine, it can be suggested that the pH environment in S-AKI 6-hours had no significant change compared to the control group.

Regarding the NOE parameter, the change in this parameter is related to the change in macromolecules and membrane lipids (J. Liu et al., 2018; Q. Zhang et al., 2023). In the analysis of the results, ROI covered only the medulla and cortex and excluded perirenal fat. Therefore, the contribution from lipid to the offset at -3.5 ppm can be eliminated. Based on the analysis results, the NOE alone showed no significant change between the control and sepsis groups. This indicates that the alterations in mobile macromolecule levels in renal cells have not occurred dramatically in the S-AKI 6-hour model.

Although the above results may indirectly indicate changes in the pH environment, in this study, the AACID index was also calculated to measure intracellular pH with two primary purposes: assessing the pH change between the control and sepsis groups and the pH change after injection of D-GLC and 3-OMG. In this calculation, the amine parameter was used at a frequency of 2.0 ppm to calculate AACID instead of 2.75 ppm because the amine peak is better defined at this offset and produces a more significant in vivo pH response(Albatany et al., 2022). As explained above, S-AKI causes inflammation, which can change the pH of the environment. The AACID results also showed a decreased pH in the septic group compared to the control group before glucose injection. However, this decrease was not significantly different, which agrees with the parameters analyzed above. After glucose injection, we observed that AACID increased from 20 to 60 minutes after injection at the pelvis position. This indicates that after glucose injection: D-GLC and 3-OMG, the pH environment in the kidney changed significantly at the pelvis position, or in other words, glucose increased the acidity in the urine. This change corresponded to the change in the T_2 mapping value mentioned above. However, this pH change was only clearly expressed in the control group. In the sepsis group, the amount of glucose accumulated in the pelvis decreased due to reduced blood flow and urine concentration in the septic state. Hence, the glucose concentration in the blood and urine was not large enough to change the pH environment. In the medulla and cortex, due to the characteristics of this place being the site of reabsorption and filtration, the accumulation

of glucose, or in other words, the glucose concentration here was not high, so it was not enough to change the pH index in the control group after glucose injection.

In this experiment, we observed a significant difference in the blood glucose levels between two groups injected with different types of sugars: D-GLC and 3-OMG. In the D-GLC group, the control and sepsis groups showed increased blood glucose levels after the injection. However, in the sepsis group, the increase was less pronounced than in the control group due to inflammation and reduced blood perfusion. On the other hand, in the 3-OMG injected group, there was also an increase in blood glucose levels after injection, even though 3-OMG is a non-metabolizable sugar. It is still transported via GLUT1 and GLUT2 competes with glucose for binding to these transporters(Akansha Ashvani Sehgal et al., 2019). Additionally, a study on 3-OMG pointed out that 3-OMG can cause an immediate increase in blood glucose. This is due to the high levels of 3-OMG in the plasma, which increases the energy demand not satisfied by the glycolytic support mechanism. As a result, hyperglycemia occurs instead of activating the glycolytic stress response(Hwang, Kim, Evelhoch, & Ackerman, 1992).

According to recent studies, each AKI disease model would have different diseased characteristics. In particular, the S-AKI disease models are carefully selected to ensure that the disease mechanism and pathological manifestations are almost equivalent to the human disease model. Among those disease models, the lipopolysaccharide model is widely used in research. Moreover, disease models such as lipopolysaccharide, cecal ligation and puncture models do not cause pathological changes like the human disease model. Therefore, currently, the PCI model is a polymicrobial sepsis model with fluid resuscitation chosen for use in research because it causes pathological effects similar to the human disease model, such as mimic cytokine profiles, metabolic acidosis or impaired microcirculation(W. T. Zhao et al., 2023). For this reason, we adopted the PCI model in our study.

In conclusion, our study demonstrates that glucoCEST, which uses D-GLC and 3-OMG injection protocol, is a reliable and sensitive method for detecting kidney functional alterations in the early stages of S-AKI model. When combined with relaxometry mapping, it offers complementary insights into the pathophysiology of S-AKI progression. Further investigation is needed to evaluate the metabolic reprogramming in S-AKI.

5. Abstract

CEST is an advanced MRI technique that is widely used today in both clinical and research. In particular, glucoCEST can be alternative to the contrast enhancement MRI technique using gadolinium(M. Kim et al., 2022). In the scope of this thesis, the CEST and glucoCEST techniques are applied to two main topics: FAT and S-AKI. Within the FAT topic, two subtopics are explored: characterizing different types of adipose tissue and evaluating glucose uptake in BAT under both resting and activated conditions. For the S-AKI topic, glucoCEST is used to assess it as a promising biomarker. This experiment is conducted in several phases: in-vitro, ex-vivo, and then transferred to in-vivo. Sections 1 and 2 provide an overview of the research direction and the fundamental principles, including MRI physics, the principles of CEST, and glucoCEST. Section 3 focuses on the characterization of adipose tissue, while Section 4 evaluates the effectiveness of the glucoCEST technique in assessing the 6-hour S-AKI model. The first project aims to differentiate between BAT and WAT using CEST spectra, with glucose as a tracer to distinguish between the two. Additionally, it evaluates the potential of the glucoCEST technique to detect the activation status of BAT through a pharmacological activation method. In this project, based on the CEST spectrum, we have clearly distinguished between the spectra of WAT and BAT based on the characteristic structure of this type of adipose tissue. In Part 2 of the first project, the glucoCEST technique was applied with two infusion methods, i.v. and i.p., to observe the different absorption times of BAT with glucose. The i.v. method showed faster wash-in and wash-out compared to the i.p. method. This shows the reasonableness of applying the i.v technique for the BAT activation experiment because the drug activation time only lasts from 40-60 minutes after injection. In addition, ex-vivo experiments with the combination of activation drugs showed the ability of the glucoCEST technique to detect BAT before and after activation. It shows the potential of glucoCEST to evaluate the function of BAT.

The second project shows the results of the experiment applying the glucoCEST technique to evaluate S-AKI. We used a S-AKI mice model that was generated by PCI model. The results of kidney injury were confirmed by the change of some blood index such as creatine, HDL and urea. MRI assessments were performed 6h after S-AKI, including the application of D-GLC, 3-OMG as a contrast agent, T_1 mapping, and T_2

mapping. The results of glucoCEST showed that there was a change in signal between the control group and S-AKI in both types of glucose injection. The change was also observed in the T_2 mapping results between healthy and disease groups. In contrast, the T_1 mapping in the injured kidneys did not show a significant change compared with the healthy group. Additionally, the T_2 values changed in the control group before and after injection, particularly in the pelvis region. This suggests that glucose injection alters the properties of urine. This finding aligns with the AACID results, where similar changes were observed in the pelvis, indicating a shift in the pH environment after glucose injection

Our results show that glucoCEST MRI is more sensitive to the change in septic groups in the early time point at 20 minutes. It indicates that glucoCEST can be a potential biomarker to evaluate the early stage of S-AKI.

6. List of figures

7. List of tables

8. References

Faivre, A., Verissimo, T., Auwerx, H., Legouis, D., & de Seigneux, S. (2021). Tubular Cell Glucose Metabolism Shift During Acute and Chronic Injuries. *Front Med (Lausanne), 8*, 742072. doi:10.3389/fmed.2021.742072

Gochberg, D. F., & Gore, J. C. (2017). Chemical exchange saturation transfer imaging: Advances and applications by Michael T. McMahon, Assaf A. Gild, Jeff W. M. Bulte, and Peter C.M. van Zijl Publisher: Pan Stanford Publishing Pte. Ltd., Singapore. *Magn Reson Imaging*. doi:10.1016/j.mri.2017.01.004

Haacke, E. M., Brown, R. W., Thompson, M. R., & Venkatesan, R. (1999). *Magnetic Resonance Imaging: Physical Principles and Sequence Design*: Wiley.

Hashemi, R. H., Bradley, W. G., & Lisanti, C. J. (2010). *MRI: The Basics*: Lippincott Williams & Wilkins.

Jacobs, M. (2006). Handbook of MRI pulse sequences. *Journal of Magnetic Resonance Imaging, 24*(1), 256-256. doi:https://doi.org/10.1002/jmri.20592

McRobbie, D. W., Moore, E. A., Graves, M. J., & Prince, M. R. (2017). *MRI from Picture to Proton* (3 ed.). Cambridge: Cambridge University Press.

Selby, N. M., & Francis, S. T. (2024). Assessment of Acute Kidney Injury using MRI. *J Magn Reson Imaging*. doi:10.1002/jmri.29281

Wang, B., Wang, Y., Wang, J., Jin, C., Zhou, R., Guo, J., . . . Wang, M. (2024). Multiparametric Magnetic Resonance Investigations on Acute and Long-Term Kidney Injury. *J Magn Reson Imaging, 59*(1), 43-57. doi:10.1002/jmri.28784

Wu, B., Warnock, G., Zaiss, M., Lin, C., Chen, M., Zhou, Z., . . . Delso, G. (2016). An overview of CEST MRI for non-MR physicists. *EJNMMI Phys, 3*(1), 19. doi:10.1186/s40658-016-0155-2

Albatany, M., Meakin, S., & Bartha, R. (2022). Brain pH Measurement Using AACID CEST MRI Incorporating the 2 ppm Amine Resonance. *Tomography, 8*(2), 730-739. doi:10.3390/tomography8020060

Anemone, A., Capozza, M., Arena, F., Zullino, S., Bardini, P., Terreno, E., . . . Aime, S. (2021). In vitro and in vivo comparison of MRI chemical exchange saturation transfer (CEST) properties between native glucose and 3-O-Methyl-D-glucose in a murine tumor model. *NMR Biomed, 34*(12), e4602. doi:10.1002/nbm.4602

Ávila, M., Mora Sánchez, M. G., Bernal Amador, A. S., & Paniagua, R. (2025). The Metabolism of Creatinine and Its Usefulness to Evaluate Kidney Function and Body Composition in Clinical Practice. *Biomolecules, 15*(1), 41.

Avram, A. S., Avram, M. M., & James, W. D. (2005). Subcutaneous fat in normal and diseased states: 2. Anatomy and physiology of white and brown adipose tissue. *J Am Acad Dermatol, 53*(4), 671-683. doi:10.1016/j.jaad.2005.05.015

Baliyan, V., Das, C. J., Sharma, R., & Gupta, A. K. (2016). Diffusion weighted imaging: Technique and applications. *World J Radiol, 8*(9), 785-798. doi:10.4329/wjr.v8.i9.785

Baxmann, A. C., Ahmed, M. S., Marques, N. C., Menon, V. B., Pereira, A. B., Kirsztajn, G. M., & Heilberg, I. P. (2008). Influence of muscle mass and physical activity on serum and urinary creatinine and serum cystatin C. *Clin J Am Soc Nephrol, 3*(2), 348-354. doi:10.2215/cjn.02870707

Bhuva, A. N., Treibel, T. A., Bulluck, H., Simpson, J., Manisty, C., & Moon, J. *Precision and reproducibility of blood T1 estimation: implications of T1 star on ECV calculation*: J Cardiovasc Magn Reson. 2015 Feb 3;17(Suppl 1):P4. doi: 10.1186/1532-429X-17-S1-P4. eCollection 2015.

Bloch, F., Hansen, W. W., & Packard, M. (1946). The Nuclear Induction Experiment. *Physical Review, 70*(7-8), 474-485. doi:10.1103/PhysRev.70.474

Boehm-Sturm, P., Schuenke, P., Foddis, M., Mueller, S., Koch, S. P., Beard, D. J., . . . Mergenthaler, P. (2025). 2-deoxy-D-glucose chemical exchange-sensitive spin-lock MRI of cerebral glucose metabolism after stroke in the rat. *bioRxiv*, 2025.2001.2008.628135. doi:10.1101/2025.01.08.628135

Branca, R. T., He, T., Zhang, L., Floyd, C. S., Freeman, M., White, C., & Burant, A. (2014). Detection of brown adipose tissue and thermogenic activity in mice by hyperpolarized xenon MRI. *Proc Natl Acad Sci U S A, 111*(50), 18001-18006. doi:10.1073/pnas.1403697111

Brown, R. W., Cheng, Y.-C. N., Haacke, E. M., Thompson, M. R., & Venkatesan, R. (2014). *Magnetic resonance imaging : physical principles and sequence design* Retrieved from http://site.ebrary.com/id/10861211

Buchanan, C., Mahmoud, H., Cox, E., Noble, R., Prestwich, B., Kasmi, I., . . . Selby, N. M. (2021). Multiparametric MRI assessment of renal structure and function in acute

kidney injury and renal recovery. *Clinical Kidney Journal, 14*(8), 1969-1976. doi:10.1093/ckj/sfaa221

Cai, K., Singh, A., Poptani, H., Li, W., Yang, S., Lu, Y., . . . Reddy, R. (2015). CEST signal at 2ppm (CEST@2ppm) from Z-spectral fitting correlates with creatine distribution in brain tumor. *NMR Biomed, 28*(1), 1-8. doi:10.1002/nbm.3216

Cai, Z., Zhong, Q., Feng, Y., Wang, Q., Zhang, Z., Wei, C., . . . Cai, K. (2024). Non-invasive mapping of brown adipose tissue activity with magnetic resonance imaging. *Nature Metabolism, 6*(7), 1367-1379. doi:10.1038/s42255-024-01082-z

CANNON, B., & NEDERGAARD, J. (2004). Brown Adipose Tissue: Function and Physiological Significance. *Physiological Reviews, 84*(1), 277-359. doi:10.1152/physrev.00015.2003

Chang, K. Y., Duval, S., Badesch, D. B., Bull, T. M., Chakinala, M. M., Marco, T. D., . . . Zwicke, D. (2022). Mortality in Pulmonary Arterial Hypertension in the Modern Era: Early Insights From the Pulmonary Hypertension Association Registry. *Journal of the American Heart Association, 11*(9), e024969. doi:doi:10.1161/JAHA.121.024969

Chen, J., Li, G., Sun, D., Li, H., & Chen, L. (2024). Research progress of hexokinase 2 in inflammatory-related diseases and its inhibitors. *European Journal of Medicinal Chemistry, 264*, 115986. doi:https://doi.org/10.1016/j.ejmech.2023.115986

Chen, L., Deng, H., Cui, H., Fang, J., Zuo, Z., Deng, J., . . . Zhao, L. (2018). Inflammatory responses and inflammation-associated diseases in organs. *Oncotarget, 9*(6), 7204-7218. doi:10.18632/oncotarget.23208

Chen, L., Xu, H., Gong, T., Jin, J., Lin, L., Zhou, Y., . . . Chen, Z. (2024). Accelerating multipool CEST MRI of Parkinson's disease using deep learning–based Z-spectral compressed sensing. *Magnetic Resonance in Medicine, 92*(6), 2616-2630. doi:https://doi.org/10.1002/mrm.30233

Chen, Y., Fry, B. C., & Layton, A. T. (2017). Modeling glucose metabolism and lactate production in the kidney. *Math Biosci, 289*, 116-129. doi:10.1016/j.mbs.2017.04.008

Chvojka, J., Sykora, R., Krouzecky, A., Radej, J., Varnerova, V., Karvunidis, T., . . . Matejovic, M. (2008). Renal haemodynamic, microcirculatory, metabolic and histopathological responses to peritonitis-induced septic shock in pigs. *Crit Care, 12*(6), R164. doi:10.1186/cc7164

Consolino, L., Anemone, A., Capozza, M., Carella, A., Irrera, P., Corrado, A., . . . Longo, D. L. (2020). Non-invasive Investigation of Tumor Metabolism and Acidosis by MRI-CEST Imaging. *Front Oncol, 10*, 161. doi:10.3389/fonc.2020.00161

Cypess, A. M., Weiner, L. S., Roberts-Toler, C., Franquet Elía, E., Kessler, S. H., Kahn, P. A., . . . Kolodny, G. M. (2015). Activation of human brown adipose tissue by a β3-adrenergic receptor agonist. *Cell Metab, 21*(1), 33-38. doi:10.1016/j.cmet.2014.12.009

De Graaf, R. A. (2007). *In vivo NMR spectroscopy : principles and techniques* (2nd ed ed.). Chichester, West Sussex, England: John Wiley & Sons.

DeBrosse, C., Nanga, R. P., Bagga, P., Nath, K., Haris, M., Marincola, F., . . . Reddy, R. (2016). Lactate Chemical Exchange Saturation Transfer (LATEST) Imaging in vivo A Biomarker for LDH Activity. *Sci Rep, 6*, 19517. doi:10.1038/srep19517

Faghihi, R., Zeinali-Rafsanjani, B., Mosleh-Shirazi, M.-A., Saeedi-Moghadam, M., Lotfi, M., Jalli, R., & Iravani, V. (2017). Magnetic Resonance Spectroscopy and its Clinical Applications: A Review. *Journal of Medical Imaging and Radiation Sciences, 48*(3), 233-253. doi:10.1016/j.jmir.2017.06.004

Faix, J. D. (2013). Biomarkers of sepsis. *Crit Rev Clin Lab Sci, 50*(1), 23-36. doi:10.3109/10408363.2013.764490

Franz, D., Syväri, J., Weidlich, D., Baum, T., Rummeny, E. J., & Karampinos, D. C. (2018). *Magnetic Resonance Imaging of Adipose Tissue in Metabolic Dysfunction*.

Gao, T., Zou, C., Li, Y., Jiang, Z., Tang, X., & Song, X. (2021). A Brief History and Future Prospects of CEST MRI in Clinical Non-Brain Tumor Imaging. *Int J Mol Sci, 22*(21). doi:10.3390/ijms222111559

Gochberg, D. F., & Gore, J. C. (2017). Chemical exchange saturation transfer imaging: Advances and applications by Michael T. McMahon, Assaf A. Gild, Jeff W. M. Bulte, and Peter C.M. van Zijl Publisher: Pan Stanford Publishing Pte. Ltd., Singapore. *Magn Reson Imaging*. doi:10.1016/j.mri.2017.01.004

Goerke, S., Zaiss, M., & Bachert, P. (2014). Characterization of creatine guanidinium proton exchange by water-exchange (WEX) spectroscopy for absolute-pH CEST imaging in vitro. *NMR Biomed, 27*(5), 507-518. doi:10.1002/nbm.3086

Goerke, S., Zaiss, M., Kunz, P., Klika, K. D., Windschuh, J. D., Mogk, A., . . . Bachert, P. (2015). Signature of protein unfolding in chemical exchange saturation transfer imaging. *NMR Biomed, 28*(7), 906-913. doi:10.1002/nbm.3317

Goyal, A., Sharma, R., Bhalla, A. S., Gamanagatti, S., & Seth, A. (2012). Diffusion-weighted MRI in assessment of renal dysfunction. *Indian J Radiol Imaging, 22*(3), 155-159. doi:10.4103/0971-3026.107169

Haacke, E. M., Brown, R. W., Thompson, M. R., & Venkatesan, R. (1999). *Magnetic Resonance Imaging: Physical Principles and Sequence Design*: Wiley.

Hamilton, G., Smith Jr, D. L., Bydder, M., Nayak, K. S., & Hu, H. H. (2011). MR properties of brown and white adipose tissues. *Journal of Magnetic Resonance Imaging, 34*(2), 468-473. doi:https://doi.org/10.1002/jmri.22623

Hankir, M. K., Kranz, M., Keipert, S., Weiner, J., Andreasen, S. G., Kern, M., . . . Fenske, W. K. (2017). Dissociation Between Brown Adipose Tissue (18)F-FDG Uptake and Thermogenesis in Uncoupling Protein 1-Deficient Mice. *J Nucl Med, 58*(7), 1100-1103. doi:10.2967/jnumed.116.186460

Haris, M., Nanga, R. P., Singh, A., Cai, K., Kogan, F., Hariharan, H., & Reddy, R. (2012). Exchange rates of creatine kinase metabolites: feasibility of imaging creatine by chemical exchange saturation transfer MRI. *NMR Biomed, 25*(11), 1305-1309. doi:10.1002/nbm.2792

Hashemi, R. H., Bradley, W. G., & Lisanti, C. J. (2010). *MRI: The Basics*: Lippincott Williams & Wilkins.

Henkelman, R. M., Hardy, P. A., Bishop, J. E., Poon, C. S., & Plewes, D. B. (1992). Why fat is bright in RARE and fast spin-echo imaging. *J Magn Reson Imaging, 2*(5), 533-540. doi:10.1002/jmri.1880020511

Henkelman, R. M., Stanisz, G. J., & Graham, S. J. (2001). Magnetization transfer in MRI: a review. *NMR Biomed, 14*(2), 57-64. doi:10.1002/nbm.683

Hosono, M., Takenaka, M., Monzen, H., Tamura, M., Kudo, M., & Nishimura, Y. (2021). Cumulative radiation doses from recurrent PET-CT examinations. *Br J Radiol, 94*(1126), 20210388. doi:10.1259/bjr.20210388

Hoste, E. A. J., Kellum, J. A., Selby, N. M., Zarbock, A., Palevsky, P. M., Bagshaw, S. M., . . . Chawla, L. S. (2018). Global epidemiology and outcomes of acute kidney injury. *Nat Rev Nephrol, 14*(10), 607-625. doi:10.1038/s41581-018-0052-0

Hwang, Y. Y., Kim, S. G., Evelhoch, J. L., & Ackerman, J. J. (1992). Nonglycolytic acidification of murine radiation-induced fibrosarcoma 1 tumor via 3-O-methyl-D-glucose monitored by 1H, 2H, 13C, and 31P nuclear magnetic resonance spectroscopy. *Cancer Res, 52*(5), 1259-1266.

Jacobs, M. (2006). Handbook of MRI pulse sequences. *Journal of Magnetic Resonance Imaging, 24*(1), 256-256. doi:https://doi.org/10.1002/jmri.20592

Jiang, W., Song, L., Gong, W., Zhang, Y., Shi, K., Liao, T., . . . Zheng, R. (2023). Low HDL-C can be a biomarker to predict persistent severe AKI in septic patients? A retrospective cohort study. *Eur J Med Res, 28*(1), 567. doi:10.1186/s40001-023-01513-9

Jin, T., Iordanova, B., Hitchens, T. K., Modo, M., Wang, P., Mehrens, H., & Kim, S. G. (2018). Chemical exchange-sensitive spin-lock (CESL) MRI of glucose and analogs in brain tumors. *Magn Reson Med, 80*(2), 488-495. doi:10.1002/mrm.27183

Jones, D. K. (2010). *Diffusion MRI*: Oxford University Press.

Katagiri, D., Wang, F., Gore, J. C., Harris, R. C., & Takahashi, T. (2021). Clinical and experimental approaches for imaging of acute kidney injury. *Clin Exp Nephrol, 25*(7), 685-699. doi:10.1007/s10157-021-02055-2

Kentrup, D., Bovenkamp, P., Busch, A., Schuette-Nuetgen, K., Pawelski, H., Pavenstadt, H., . . . Hoerr, V. (2017). GlucoCEST magnetic resonance imaging in vivo may be diagnostic of acute renal allograft rejection. *Kidney Int, 92*(3), 757-764. doi:10.1016/j.kint.2017.04.015

Kim, J., Wu, Y., Guo, Y., Zheng, H., & Sun, P. Z. (2015). A review of optimization and quantification techniques for chemical exchange saturation transfer MRI toward sensitive in vivo imaging. *Contrast Media Mol Imaging, 10*(3), 163-178. doi:10.1002/cmmi.1628

Kim, M., Eleftheriou, A., Ravotto, L., Weber, B., Rivlin, M., Navon, G., . . . consortium, G. (2022). What do we know about dynamic glucose-enhanced (DGE) MRI and how close is it to the clinics? Horizon 2020 GLINT consortium report. *MAGMA, 35*(1), 87-104. doi:10.1007/s10334-021-00994-1

Kim, P. K., Hong, Y. J., Im, D. J., Suh, Y. J., Park, C. H., Kim, J. Y., . . . Choi, B. W. (2017). Myocardial T1 and T2 Mapping: Techniques and Clinical Applications. *Korean J Radiol, 18*(1), 113-131. doi:10.3348/kjr.2017.18.1.113

Konigsfeld, H. P., Viana, T. G., Pereira, S. C., Santos, T. O. C. D., Kirsztajn, G. M., Tavares, A., & de Souza Durão Junior, M. (2019). Acute kidney injury in hospitalized patients who underwent percutaneous kidney biopsy for histological

diagnosis of their renal disease. *BMC Nephrology, 20*(1), 315. doi:10.1186/s12882-019-1514-8

Kruger, C., Nguyen, T. T., Breaux, C., Guillory, A., Mangelli, M., Fridianto, K. T., . . . Stadler, K. (2019). Proximal Tubular Cell-Specific Ablation of Carnitine Acetyltransferase Causes Tubular Disease and Secondary Glomerulosclerosis. *Diabetes, 68*(4), 819-831. doi:10.2337/db18-0090

Kwok, K. H. M., Lam, K. S. L., & Xu, A. (2016). Heterogeneity of white adipose tissue: molecular basis and clinical implications. *Experimental & Molecular Medicine, 48*(3), e215-e215. doi:10.1038/emm.2016.5

Larson, P. E., Han, M., Krug, R., Jakary, A., Nelson, S. J., Vigneron, D. B., . . . Kelley, D. A. (2016). Ultrashort echo time and zero echo time MRI at 7T. *MAGMA, 29*(3), 359-370. doi:10.1007/s10334-015-0509-0

Liepinsh, E., & Otting, G. (1996). Proton exchange rates from amino acid side chains--implications for image contrast. *Magn Reson Med, 35*(1), 30-42. doi:10.1002/mrm.1910350106

Liu, C., Wei, W., Huang, Y., Fu, P., Zhang, L., & Zhao, Y. (2024). Metabolic reprogramming in septic acute kidney injury: pathogenesis and therapeutic implications. *Metabolism, 158*, 155974. doi:https://doi.org/10.1016/j.metabol.2024.155974

Liu, G., Song, X., Chan, K. W., & McMahon, M. T. (2013). Nuts and bolts of chemical exchange saturation transfer MRI. *NMR Biomed, 26*(7), 810-828. doi:10.1002/nbm.2899

Liu, J., Han, Z., Chen, G., Li, Y., Zhang, J., Xu, J., . . . Liu, G. (2018). CEST MRI of sepsis-induced acute kidney injury. *NMR Biomed, 31*(8), e3942. doi:10.1002/nbm.3942

Maliszewska, K., & Kretowski, A. (2021). Brown Adipose Tissue and Its Role in Insulin and Glucose Homeostasis. *Int J Mol Sci, 22*(4). doi:10.3390/ijms22041530

Marik, P. E., & Taeb, A. M. (2017). SIRS, qSOFA and new sepsis definition. *J Thorac Dis, 9*(4), 943-945. doi:10.21037/jtd.2017.03.125

McConnell, H. M. (1958). Reaction Rates by Nuclear Magnetic Resonance. *The Journal of Chemical Physics, 28*(3), 430-431. doi:10.1063/1.1744152

McMahon, M. T., Gilad, A.A., Bulte, J.W.M., & van Zijl, P.C.M. (2017). Chemical Exchange Saturation Transfer Imaging: Advances and Applications (1st ed.). *NMR in Biomedicine, 30*(10), e3788. doi:https://doi.org/10.1002/nbm.3788

McRobbie, D. W., Moore, E. A., Graves, M. J., & Prince, M. R. (2017). *MRI from Picture to Proton* (3 ed.). Cambridge: Cambridge University Press.

Meng, N., Huang, Z., Jiang, H., Dai, B., Shen, L., Liu, X., . . . Wang, M. (2024). Glucose chemical exchange saturation transfer MRI for predicting the histological grade of rectal cancer: a comparative study with amide proton transfer-weighted and diffusion-weighted imaging. *Insights into Imaging, 15*(1), 269. doi:10.1186/s13244-024-01828-z

Murase, K. (2018). Basics of Chemical Exchange Saturation Transfer (CEST) Magnetic Resonance Imaging. doi:10.5772/intechopen.71645

Mushtaq, M., Abdul Mateen, M., & Kim, U. H. (2019). Hyperglycemia associated blood viscosity can be a nexus stimuli. *Clin Hemorheol Microcirc, 71*(1), 103-112. doi:10.3233/ch-180426

Nievelstein, R. A., Quarles van Ufford, H. M., Kwee, T. C., Bierings, M. B., Ludwig, I., Beek, F. J., . . . Geleijns, J. (2012). Radiation exposure and mortality risk from CT and PET imaging of patients with malignant lymphoma. *Eur Radiol, 22*(9), 1946-1954. doi:10.1007/s00330-012-2447-9

Nikiforaki, K., & Marias, K. (2023). MRI Methods to Visualize and Quantify Adipose Tissue in Health and Disease. *Biomedicines, 11*(12). doi:10.3390/biomedicines11123179

Peerapornratana, S., Manrique-Caballero, C. L., Gómez, H., & Kellum, J. A. (2019). Acute kidney injury from sepsis: current concepts, epidemiology, pathophysiology, prevention and treatment. *Kidney Int, 96*(5), 1083-1099. doi:10.1016/j.kint.2019.05.026

Peterson, P., Trinh, L., & Månsson, S. (2021). Quantitative 1H MRI and MRS of fatty acid composition. *Magnetic Resonance in Medicine, 85*(1), 49-67. doi:https://doi.org/10.1002/mrm.28471

Ricci, M., De Feo, M. S., Granese, G. M., Frantellizzi, V., Carabellese, B., Lubrano, E., & Cimini, A. (2023). (18)F-FDG PET/CT technology for the assessment of brown adipose tissue: an updated review. *Expert Rev Med Devices, 20*(12), 1143-1156. doi:10.1080/17434440.2023.2283618

Rivlin, M., & Navon, G. (2018). CEST MRI of 3-O-methyl-D-glucose on different breast cancer models. *Magnetic Resonance in Medicine, 79*(2), 1061-1069. doi:https://doi.org/10.1002/mrm.26752

Rivlin, M., & Navon, G. (2019). Molecular imaging of tumors by chemical exchange saturation transfer MRI of glucose analogs. *Quant Imaging Med Surg, 9*(10), 1731-1746.

Roveran Genga, K., Lo, C., Cirstea, M., Zhou, G., Walley, K. R., Russell, J. A., . . . Boyd, J. H. (2017). Two-year follow-up of patients with septic shock presenting with low HDL: the effect upon acute kidney injury, death and estimated glomerular filtration rate. *Journal of Internal Medicine, 281*(5), 518-529. doi:https://doi.org/10.1111/joim.12601

Scheen, M., Giraud, R., & Bendjelid, K. (2021). Stress hyperglycemia, cardiac glucotoxicity, and critically ill patient outcomes current clinical and pathophysiological evidence. *Physiol Rep, 9*(2), e14713. doi:10.14814/phy2.14713

Scotti, A., Tain, R.-W., Li, W., Gil, V., Liew, C. W., & Cai, K. (2018). Mapping brown adipose tissue based on fat water fraction provided by Z-spectral imaging. *Journal of magnetic resonance imaging : JMRI, 47*(6), 1527-1533. doi:10.1002/jmri.25890

Sehgal, A. A., Li, Y., Lal, B., Yadav, N. N., Xu, X., Xu, J., . . . van Zijl, P. C. M. (2019). CEST MRI of 3-O-methyl-D-glucose uptake and accumulation in brain tumors. *Magn Reson Med, 81*(3), 1993-2000. doi:10.1002/mrm.27489

Seidemo, A. (2023). *Dynamic glucose enhanced chemical exchange saturation transfer MRI: Optimization of methodology and characterization of cerebral transport kinetics.* Lund University, Lund.

Selby, N. M., & Francis, S. T. (2025). Assessment of Acute Kidney Injury using MRI. *J Magn Reson Imaging, 61*(1), 25-41. doi:10.1002/jmri.29281

Steidle, G., Eibofner, F., & Schick, F. (2011). Quantitative diffusion imaging of adipose tissue in the human lower leg at 1.5 T. *Magn Reson Med, 65*(4), 1118-1124. doi:10.1002/mrm.22699

Sun, P. Z. (2012). Simplified quantification of labile proton concentration-weighted chemical exchange rate (kws) with RF saturation time dependent ratiometric analysis (QUESTRA): normalization of relaxation and RF irradiation spillover effects for improved quantitative chemical exchange saturation transfer (CEST) MRI. *Magnetic Resonance in Medicine, 67*(4), 936-942.

Sun, P. Z., Lu, J., Wu, Y., Xiao, G., & Wu, R. (2013). Evaluation of the dependence of CEST-EPI measurement on repetition time, RF irradiation duty cycle and imaging

flip angle for enhanced pH sensitivity. *Phys Med Biol, 58*(17), N229-240. doi:10.1088/0031-9155/58/17/n229

Tain, R., Xu, H. N., Zhou, X. J., Li, L. Z., & Cai, K. (2016). Magnetization Transfer MRI Contrast May Correlate with Tissue Redox State in Prostate Cancer. *Adv Exp Med Biol, 923*, 401-406. doi:10.1007/978-3-319-38810-6_52

Thakur, V., Alcoreza, N., Cazares, J., & Chattopadhyay, M. (2021). Changes in Stress-Mediated Markers in a Human Cardiomyocyte Cell Line under Hyperglycemia. *Int J Mol Sci, 22*(19). doi:10.3390/ijms221910802

Trayhurn, P., & Beattie, J. H. (2001). Physiological role of adipose tissue: white adipose tissue as an endocrine and secretory organ. *Proc Nutr Soc, 60*(3), 329-339. doi:10.1079/pns200194

van Zijl, P. C., & Yadav, N. N. (2011). Chemical exchange saturation transfer (CEST): what is in a name and what isn't? *Magn Reson Med, 65*(4), 927-948. doi:10.1002/mrm.22761

Verma, S. K., Nagashima, K., Yaligar, J., Michael, N., Lee, S. S., Xianfeng, T., . . . Velan, S. S. (2017). Differentiating brown and white adipose tissues by high-resolution diffusion NMR spectroscopy. *J Lipid Res, 58*(1), 289-298. doi:10.1194/jlr.D072298

Vinogradov, E., Sherry, A. D., & Lenkinski, R. E. (2013). CEST: from basic principles to applications, challenges and opportunities. *J Magn Reson, 229*, 155-172. doi:10.1016/j.jmr.2012.11.024

Walker-Samuel, S., Ramasawmy, R., Torrealdea, F., Rega, M., Rajkumar, V., Johnson, S. P., . . . Golay, X. (2013). In vivo imaging of glucose uptake and metabolism in tumors. *Nat Med, 19*(8), 1067-1072. doi:10.1038/nm.3252

Walker, M. E., Kodani, S. D., Mena, H. A., Tseng, Y. H., Cypess, A. M., & Spite, M. (2024). Brown Adipose Tissue Activation in Humans Increases Plasma Levels of Lipid Mediators. *J Clin Endocrinol Metab, 109*(7), 1837-1849. doi:10.1210/clinem/dgae016

Wang, B., Wang, Y., Wang, J., Jin, C., Zhou, R., Guo, J., . . . Wang, M. (2024). Multiparametric Magnetic Resonance Investigations on Acute and Long-Term Kidney Injury. *J Magn Reson Imaging, 59*(1), 43-57. doi:10.1002/jmri.28784

Wang, F., Kopylov, D., Zu, Z., Takahashi, K., Wang, S., Quarles, C. C., . . . Takahashi, T. (2016). Mapping murine diabetic kidney disease using chemical exchange

saturation transfer MRI. *Magn Reson Med, 76*(5), 1531-1541. doi:10.1002/mrm.26045

Wang, J., Weygand, J., Hwang, K.-P., Mohamed, A. S. R., Ding, Y., Fuller, C. D., . . . Zhou, J. (2016). Magnetic Resonance Imaging of Glucose Uptake and Metabolism in Patients with Head and Neck Cancer. *Scientific Reports, 6*(1), 30618. doi:10.1038/srep30618

Wang, X. Y., Pang, Y. P., Jiang, T., Wang, S., Li, J. T., Shi, B. M., & Yu, C. (2019). Value of early diagnosis of sepsis complicated with acute kidney injury by renal contrast-enhanced ultrasound. *World J Clin Cases, 7*(23), 3934-3944. doi:10.12998/wjcc.v7.i23.3934

Ward, K. M., Aletras, A. H., & Balaban, R. S. (2000). A New Class of Contrast Agents for MRI Based on Proton Chemical Exchange Dependent Saturation Transfer (CEST). *Journal of Magnetic Resonance, 143*(1), 79-87. doi:https://doi.org/10.1006/jmre.1999.1956

Wen, L., Li, Y., Li, S., Hu, X., Wei, Q., & Dong, Z. (2021). Glucose Metabolism in Acute Kidney Injury and Kidney Repair. *Front Med (Lausanne), 8*, 744122. doi:10.3389/fmed.2021.744122

Westbrook, C., & Talbot, J. (2019). *MRI in Practice, Fifth Edition*: John Wiley & Sons (UK).

Wu, B., Warnock, G., Zaiss, M., Lin, C., Chen, M., Zhou, Z., . . . Delso, G. (2016b). An overview of CEST MRI for non-MR physicists. *EJNMMI Physics, 3*(1), 19. doi:10.1186/s40658-016-0155-2

Wu, J., Boström, P., Sparks, Lauren M., Ye, L., Choi, Jang H., Giang, A.-H., . . . Spiegelman, Bruce M. (2012). Beige Adipocytes Are a Distinct Type of Thermogenic Fat Cell in Mouse and Human. *Cell, 150*(2), 366-376. doi:10.1016/j.cell.2012.05.016

Xia, Y. (2022). *Essential Concepts in MRI: Physics, Instrumentation, Spectroscopy and Imaging*: Wiley.

Xiao, Z., Huang, Q., Yang, Y., Liu, M., Chen, Q., Huang, J., . . . Ai, K. (2022). Emerging early diagnostic methods for acute kidney injury. *Theranostics, 12*(6), 2963-2986. doi:10.7150/thno.71064

Yaligar, J., Verma, S. K., Gopalan, V., Anantharaj, R., Thu Le, G. T., Kaur, K., . . . Velan, S. S. (2020). Dynamic contrast-enhanced MRI of brown and beige adipose tissues. *Magn Reson Med, 84*(1), 384-395. doi:10.1002/mrm.28118

Zaiss, M., & Bachert, P. (2013). Chemical exchange saturation transfer (CEST) and MR Z-spectroscopy in vivo: a review of theoretical approaches and methods. *Phys Med Biol, 58*(22), R221-269. doi:10.1088/0031-9155/58/22/R221

Zaiss, M., Jin, T., Kim, S. G., & Gochberg, D. F. (2022). Theory of chemical exchange saturation transfer MRI in the context of different magnetic fields. *NMR Biomed, 35*(11), e4789. doi:10.1002/nbm.4789

Zancanaro, C., Nano, R., Marchioro, C., Sbarbati, A., Boicelli, A., & Osculati, F. (1994). Magnetic resonance spectroscopy investigations of brown adipose tissue and isolated brown adipocytes. *J Lipid Res, 35*(12), 2191-2199. doi:https://doi.org/10.1016/S0022-2275(20)39925-9

Zarbock, A., Nadim, M. K., Pickkers, P., Gomez, H., Bell, S., Joannidis, M., . . . Forni, L. G. (2023). Sepsis-associated acute kidney injury: consensus report of the 28th Acute Disease Quality Initiative workgroup. *Nat Rev Nephrol, 19*(6), 401-417. doi:10.1038/s41581-023-00683-3

Zhang, Q., Tao, Q., Xie, Y., Chen, Z., Seeliger, E., Niendorf, T., . . . Feng, Y. (2023). Assessment of rhabdomyolysis-induced acute kidney injury with chemical exchange saturation transfer magnetic resonance imaging. *Quant Imaging Med Surg, 13*(12), 8336-8349. doi:10.21037/qims-23-699

Zhang, S., Trokowski, R., & Sherry, A. D. (2003). A Paramagnetic CEST Agent for Imaging Glucose by MRI. *Journal of the American Chemical Society, 125*(50), 15288-15289. doi:10.1021/ja038345f

Zhang, Z. (2015). Biomarkers, diagnosis and management of sepsis-induced acute kidney injury: a narrative review. *Heart Lung Vessel, 7*(1), 64-73.

Zhao, W. T., Herrmann, K. H., Sibgatulin, R., Nahardani, A., Kramer, M., Heitplatz, B., . . . Hoerr, V. (2023). Perfusion and T(2) Relaxation Time as Predictors of Severity and Outcome in Sepsis-Associated Acute Kidney Injury: A Preclinical MRI Study. *J Magn Reson Imaging, 58*(6), 1954-1963. doi:10.1002/jmri.28698

Zhou, I. Y., Wang, E., Cheung, J. S., Zhang, X., Fulci, G., & Sun, P. Z. (2017). Quantitative chemical exchange saturation transfer (CEST) MRI of glioma using Image Downsampling Expedited Adaptive Least-squares (IDEAL) fitting. *Sci Rep, 7*(1), 84. doi:10.1038/s41598-017-00167-y

Zhou, J., Payen, J. F., Wilson, D. A., Traystman, R. J., & van Zijl, P. C. (2003). Using the amide proton signals of intracellular proteins and peptides to detect pH effects in MRI. *Nat Med, 9*(8), 1085-1090. doi:10.1038/nm907

Zhu, H., Li, Y., Ding, Y., Liu, Y., Shen, N., Xie, Y., . . . Zhu, W. (2024). Multi-pool chemical exchange saturation transfer MRI in glioma grading, molecular subtyping and evaluating tumor proliferation. *J Neurooncol, 169*(2), 287-297. doi:10.1007/s11060-024-04729-9

Xia, Y. (2022). *Essential Concepts in MRI: Physics, Instrumentation, Spectroscopy and Imaging*: Wiley.

Zarbock, A., Nadim, M. K., Pickkers, P., Gomez, H., Bell, S., Joannidis, M., . . . Forni, L. G. (2023). Sepsis-associated acute kidney injury: consensus report of the 28th Acute Disease Quality Initiative workgroup. *Nat Rev Nephrol, 19*(6), 401-417. doi:10.1038/s41581-023-00683-3

9. Statement on own contribution

The work was carried out at the Heart center of university hospital Bonn, Germany under the supervision of Professor Verena Hörr.

The study was designed by Verena Hörr, a professor of cardiovascular imaging at the heart center in the University hospital Bonn, Germany.

All MRI experiments and analyses were carried out by me with the support of Dr. Ali Nahardani and Leon Sadowski.

The following blood tests and IHC were carried out by our collaborator “SynLab” from Cologne University hospital, Germany and Dr. Stephan Niland from Institute of Physiological Chemistry and Patho-biochemistry, university of Munster, Germany.

The data used for the evaluation was generated independently by me.

The statistical evaluation was performed by me independently under the guidance of Professor Verena Hörr and Dr. Ali Nahardani.

In preparing this dissertation, I used Grammarly to improve the readability and linguistics clarity of selected passages. After using this tool, I reviewed and edited all relevant sections myself and take full responsibility for the scientific content of the dissertation.

I confirm that I have written this thesis independently and have not used any sources or aids other than those specified by me.

I hereby confirm that my thesis complies with the Statement by the Executive Committee of the Deutsche Forschungsgemeinschaft (DFG, German Research Foundation) on the Influence of Generative Models of Text and Image Creation on Science and the Humanities and on the DFG’s Funding Activities.

10. Acknowledgements

It is time to thank those who supported and accompanied me during my doctoral studies at the University of Bonn. Firstly, I would like to extend my deepest gratitude to Professor Verena Hörr for her invaluable guidance, support, and encouragement. Her dedication and insight have been in guiding not only my research but also my development as a researcher. This thesis would not have been possible without her continuous mentorship and encouragement.

I also would like to thank PhD committee members Professor Andreas Schlitzer, Professor Hiroki Kato, and Professor Julian Luetkens for their feedback, suggestions, and continuous support. I sincerely appreciate the time they invested in reviewing my progress and the advice they provided during my thesis.

A special thank you goes to Dr. Ali Nahardani, whose expertise and practical assistance were invaluable in my research. His support, particularly in MRI scanning and data processing, has significantly improved my work quality. His patience, willingness to share his knowledge, and collaborative spirit have motivated me during challenging moments in my research.

I am also deeply thankful to Mrs. Sara Moradi for her excellent data management and organizational support, and to Mr. Leon Sadowski for his valuable support in data analysis.

Most importantly, I would like to express my heartfelt appreciation to my family and friends who have always believed in me, thank you for your great support. Especially to my wife and child, words cannot express how grateful I am for your love, patience, and understanding. Your unconditional support has allowed me to pursue this dream. Your belief in me gave me the strength to overcome the toughest of times, and I am eternally grateful for the sacrifices you made for me.

This thesis is as much a product of your faith in me as it is of my work.